CONTACT PROBLEMS WITH SURFACE STRESS EFFECTS

Mr. Supakorn Tirapat

A Dissertation Submitted in Partial Fulfillment of the Requirements
for the Degree of Doctor of Philosophy Program in Civil Engineering
Department of Civil Engineering
Faculty of Engineering
Chulalongkorn University
Academic Year 2017

ปัญหาการสัมผัสที่มีผลกระทบจากหน่วยแรงที่ผิว

นายศุภกร ติระพัฒน์

วิทยานิพนธ์นี้เป็นส่วนหนึ่งของการศึกษาตามหลักสูตรปริญญาวิศวกรรมศาสตรดุษฎีบัณฑิต
สาขาวิชาวิศวกรรมโยธา ภาควิชาวิศวกรรมโยธา
คณะวิศวกรรมศาสตร์ จุฬาลงกรณ์มหาวิทยาลัย
ปีการศึกษา 2560

Thesis Title	CONTACT PROBLEMS WITH SURFACE STRESS EFFECTS
By	Mr. Supakorn Tirapat
Field of Study	Civil Engineering
Thesis Advisor	Professor Dr. Teerapong Senjuntichai
Thesis Co-Advisor	Associate Professor Dr. Jaroon Rungamornrat

Accepted by the Faculty of Engineering, Chulalongkorn University in Partial Fulfillment of the Requirements for the Doctoral Degree

.....Dean of the Faculty of Engineering
(Associate Professor Dr. Supot Teachavorasinskun)

THESIS COMMITTEE

.....Chairman
(Professor Dr. Thaksin Thepchatri)

.....Thesis Advisor
(Professor Dr. Teerapong Senjuntichai)

.....Thesis Co-Advisor
(Associate Professor Dr. Jaroon Rungamornrat)

.....Examiner
(Assistant Professor Dr. Watanachai Smittakorn)

.....Examiner
(Associate Professor Dr. Akhrawat Lenwari)

.....External Examiner
(Professor Dr. Pruettha Nanakorn)

ศุภกร ติระพัฒน์ : ปัญหาการสัมผัสที่มีผลกระทบจากหน่วยแรงที่ผิว (CONTACT PROBLEMS WITH SURFACE STRESS EFFECTS) อ.ที่ปรึกษาวิทยานิพนธ์หลัก: ศ. ดร. ธีรพงศ์ เสนจันทร์ตไชย, อ.ที่ปรึกษาวิทยานิพนธ์ร่วม: รศ. ดร. จรูญ รุ่งอมรรัตน์, 103 หน้า.

วิทยานิพนธ์ฉบับนี้นำเสนอปัญหาการสัมผัสที่มีผลกระทบจากหน่วยแรงที่ผิว โดยใช้สมการของเกอร์ตินและเมอร์ดอครูปแบบสมบูรณ์ในการจำลองพฤติกรรมของหน่วยแรงที่ผิว ในการศึกษานี้ได้นำเสนอผลเฉลยมูลฐานของชั้นบางยืดหยุ่นวางบนตัวกลางกึ่งปริภูมิภายใต้แรงกระทำแบบสมมาตรรอบแกน การหาคำตอบของผลเฉลยของการเคลื่อนที่และหน่วยแรงในรูปของปริพันธ์กึ่งอนันต์อาศัยหลักการตัวแทนความเครียดศักดิ์ของเลิฟและการแปลงแฮนเคลอินทิกรัล ซึ่งสามารถหาคำตอบที่ถูกต้องแม่นยำโดยการใช้ระเบียบวิธีเชิงตัวเลขที่เหมาะสม ผลเฉลยมูลฐานดังกล่าวถูกนำมาใช้ในการพัฒนาแบบจำลองทางคณิตศาสตร์สำหรับปัญหาการกดแบบแข็งเกร็งทั้งแบบมีและไม่มีแรงเสียดทานบนชั้นบางยืดหยุ่นวางบนตัวกลางกึ่งปริภูมิ นอกจากนี้ได้นำไปใช้ในการวิเคราะห์ปัญหาการรับแรงร่วมกันระหว่างแผ่นวงกลมยืดหยุ่นและตัวกลางกึ่งปริภูมิภายใต้อิทธิพลของหน่วยแรงที่ผิวในระดับนาโน ผลเฉลยเชิงตัวเลขถูกใช้ในการศึกษาอิทธิพลของหน่วยแรงที่ผิวที่มีผลต่อคำตอบของสนามยืดหยุ่น พบว่าหน่วยแรงที่ผิวจะมีอิทธิพลมากโดยเฉพาะตรงบริเวณที่ใกล้กับพื้นผิวและส่งผลให้วัสดุมีพฤติกรรมที่ขึ้นอยู่กับขนาดและทำให้วัสดุมีความแข็งมากขึ้น จากการศึกษาในครั้งนี้สามารถสรุปได้ว่าหน่วยแรงที่ผิวมีอิทธิพลต่อพฤติกรรมเชิงกลของวัสดุในระดับนาโนอย่างมาก คำตอบที่ได้จากการวิเคราะห์ปัญหานี้ สามารถใช้เป็นผลเฉลยเกณฑ์เปรียบเทียบในการพัฒนาระเบียบวิธีการเชิงตัวเลข เช่น ไฟไนต์เอลิเมนต์และระเบียบวิธีบาวดารีเอลิเมนต์สำหรับการวิเคราะห์ปัญหาการสัมผัสที่ซับซ้อนมากขึ้นภายใต้อิทธิพลของหน่วยแรงที่ผิวสำหรับปัญหาในระดับนาโนและปัญหาที่เกี่ยวข้องกับวัสดุยืดหยุ่นอ่อน

ภาควิชา วิศวกรรมโยธา ลายมือชื่อนิสิต .....

สาขาวิชา วิศวกรรมโยธา ลายมือชื่อ อ.ที่ปรึกษาหลัก .....

ปีการศึกษา 2560 ลายมือชื่อ อ.ที่ปรึกษาร่วม .....

5571436521 : MAJOR CIVIL ENGINEERING
KEYWORDS: CONTACT PROBLEM / LAYERED MEDIUM / GURTIN-MURDOCH / NANOINDENTATION / NANOPLATE / SIZE-DEPENDENT / SURFACE STRESSES / THIN FILMS

SUPAKORN TIRAPAT: CONTACT PROBLEMS WITH SURFACE STRESS EFFECTS. ADVISOR: PROF. DR. TEERAPONG SENJUNTICHAI, CO-ADVISOR: ASSOC. PROF. DR. JAROON RUNGAMORNRAT, 103 pp.

This dissertation presents a theoretical study of contact problems with consideration of surface energy effects by adopting a complete Gurtin-Murdoch theory of surface elasticity. The fundamental solution of a layered elastic half-space subjected to axisymmetric surface loading is obtained by using Love's representation and the Hankel integral transform. The analytical solutions for both displacement and stress fields are expressed in terms of semi-infinite integrals, which can be accurately evaluated by employing a numerical quadrature scheme. The obtained solutions are employed as the required influence functions in the investigation of axisymmetric indentation on a layered elastic medium with frictionless and adhesive contacts. In addition, they are also employed in the analysis of an elastic circular nanoplate under axisymmetric vertical loading resting on an elastic half-space based on a variational formulation. The accuracy of the present solution scheme is confirmed by comparison with relevant existing solutions, and selected numerical results on elastic fields under various contact problems are also presented. It is found that the surface stresses have a significant influence on both displacement and stress fields in the elastic medium especially in the vicinity of the surface. An extensive parametric study confirms that, unlike the classical elasticity solution, the material becomes stiffer and size-dependent with the presence of surface stresses. The present solution can be used as a benchmark solution in the development of numerical techniques such as the finite element and boundary element methods for analysis of more complicated contact problems under the influence of surface energy effects such as nanoscale problems and soft elastic solids.

Department:	Civil Engineering	Student's Signature	.....
Field of Study:	Civil Engineering	Advisor's Signature	.....
Academic Year:	2017	Co-Advisor's Signature	.....

ACKNOWLEDGEMENTS

The work presented in this dissertation was supported by the Thailand Research Fund (TRF) under the Royal Golden Jubilee Ph.D. (RGJ-Ph.D.) scholarship, and the research assistantship from Applied Mechanics and Structures Research Unit, Department of Civil Engineering, Faculty of Engineering, Chulalongkorn University. Those supports are gratefully acknowledged.

The author wishes to express his sincere appreciation to his advisor, Professor Dr. Teerapong Senjuntichai, and his co-advisor, Associate Professor Dr. Jaroon Rungamornrat, for their kind guidance and long-term support throughout this work. He also wishes to express his gratitude to Professor Dr. Nimal Rajapakse at the Simon Fraser University, Canada, for his kindness and invaluable advice on the research work and very warm welcome during the visit at SFU from August, 2017 to December, 2017.

The author also would like to express his sincere thanks to all committee members: Professor Dr. Thaksin Thepchatri; Professsor Dr. Pruettha Nanakorn; Associate Professor Dr. Akhrawal Lenwari; and Assistant Professor Dr. Watanachai Smittakorn for their helpful suggestions and comments.

Special thanks are also due to everyone who has helped directly and indirectly in the preparation of this dissertation. Finally, the author would like to express his gratitude to his parents for their support and love.

CONTENTS

Page

THAI ABSTRACT iv
ENGLISH ABSTRACT v
ACKNOWLEDGEMENTS vi
CONTENTS vii
LIST OF TABLES ix
LIST OF FIGURES x
LIST OF ABBREVIATIONS xiv
CHAPTER I INTRODUCTION 1
1.1 General 1
1.2 Objectives and Scopes of Present Study 3
CHAPTER II LITERATURE REVIEWS 4
2.1 General 4
2.2 Surface Elasticity Theory 4
2.3 Contact Problems with Surface Stress Effects 8
CHAPTER III LAYERED ELASTIC MEDIUM UNDER SURFACE LOADING AND SURFACE STRESS EFFECTS 16
3.1 General 16
3.2 Basic Equation and General Solution 16
3.3 Solution of Boundary Value Problem 20
3.4 Numerical Results and Discussion 25
3.5 Conclusion 29
CHAPTER IV NANOINDENTATION ON LAYERED ELASTIC MEDIUM 38
4.1 General 38
4.2 Nanoindentation with Frictionless Contact 38
4.3 Nanoindentation with Adhesive Contact 46
4.4 Conclusion 53

Page

CHAPTER V INTERACTION BETWEEN CIRCULAR NANO-PLATE AND ELASTIC MEDIUM 72
5.1 General 72
5.2 Basic Equations of Circular Nano-Plate 72
5.3 Total Potential Energy of Circular Nano-Plate 74
5.4 Variational Formulation of Interaction Problem 77
5.5 Numerical Results and Discussion 82
5.6 Conclusion 84
CHAPTER VI CONCLUSIONS 91
REFERENCES 93
VITA 103

LIST OF TABLES

Page

Table 3.1 Comparison of normalized surface displacements and stresses at the interface of a layered elastic half-space under uniformly distributed normal traction for μ_1/μ_2 = 5 and *h/a* = 1……..…..……36

Table 3.2 Comparison of normalized surface displacements and stresses at the interfaces of a layered elastic half-space under linearly distributed tangential traction for μ_1/μ_2 = 5 and *h/a* = 1……36

Table 3.3 Material properties employed in numerical study……...…..…..37

LIST OF FIGURES

Page

Figure 3.1 Layered elastic half-space subjected to axisymmetric surface loading……..31

Figure 3.2 Radial variations of elastic fields under the vertical loading for different values of layer thickness (*h/a*): (a) surface displacements (*z* = 0) and (b) stresses at the interface (*z* = *h*)……..32

Figure 3.3 Radial variations of elastic fields under the vertical loading for *h/a* = 1 and different magnitudes of residual surface stress (τ^{s}_{2}): (a) surface displacements (*z* = 0) and (b) stresses at the interface (*z* = *h*)……33

Figure 3.4 Radial variations of elastic fields under the vertical loading for *h/a* = 1 and different values of loading radius ($\bar{a}$): (a) surface displacements (*z* = 0) and (b) stresses at the interface (*z* = *h*)……..34

Figure 3.5 Radial variations of elastic fields under the radial loading for different values of layer thickness (*h/a*): (a) surface displacements (*z* = 0) and (b) stresses at the interface (*z* = *h*)……..35

Figure 4.1 A layered elastic half-space under axisymmetric indentation: (a) paraboloidal indentation and (b) flat-ended cylindrical indentation….55

Figure 4.2 Comparisons of normalized contact pressure: (a) without surface energy effects and (b) with surface energy effects…….…..56

Figure 4.3 Radial variations of elastic fields under flat-ended cylindrical indenter with *h/a* = 1 and $\bar{a}$ = 1 for different values of τ_1^s / τ_2^s: (a) normalized contact pressure and (b) normalized surface displacement.……..57

Figure 4.4 Radial variations of elastic fields at different depths under flat-ended cylindrical indenter with *h/a* = 1 and $\bar{a}$ = 1: (a) normalized vertical displacement and (b) normalized vertical stress.……..58

Figure 4.5 Variations of normalized indentation force under flat-ended cylindrical indenter for various layer thicknesses with (a) contact radius and (b) ratio of shear moduli.……..……..59

Figure 4.6 Radial variations of elastic fields under paraboloidal indenter with *h/a* = 1 and $\bar{a}$ = 1 for different values of τ_1^s / τ_2^s: (a) normalized contact pressure and (b) normalized surface displacement.……..60

Figure 4.7 Radial variations of elastic fields at different depths under paraboloidal indenter with *h/a* = 1 and $\bar{a}$ = 1: (a) normalized vertical displacement and (b) normalized vertical stress.……..…..61

Figure 4.8 Variations of normalized indentation force under paraboloidal indenter for various layer thicknesses with (a) contact radius and (b) ratio of shear moduli.……..……..……..62

Figure 4.9 An adhesive contact between a rigid flat-ended cylindrical punch of radius *a* and a layered elastic half-space.……..63

Figure 4.10 Comparisons of normalized contact pressures and surface displacements for classical numerical solutions with existing solutions under adhesive contact of flat-ended cylindrical indenter: (a) normalized contact pressure and (b) normalized surface displacements.……...…..64

Figure 4.11 Comparisons of normalized contact pressure and surface displacement for surface effects with existing solutions under frictionless contact of flat-ended cylindrical indenter: (a) normalized contact pressure and (b) normalized surface displacement.……..……..65

Figure 4.12 Distribution of normalized contact pressure and vertical surface displacement profiles under flat-ended cylindrical indenter with *h/a* = 1 and $\bar{a}$ = 1: (a) normalized contact pressure and (b) normalized vertical surface displacement.……..……..66

Figure 4.13 Radial variations of elastic fields at different depths under flat-ended cylindrical indenter with *h/a* = 1 and $\bar{a}$ = 1: (a) normalized displacements and (b) normalized stresses.……..67

Figure 4.14 Radial variations of elastic fields under flat-ended cylindrical indenter with h/a = 1 for different contact radii $\bar{a}$: (a) normalized contact pressure and (b) normalized surface displacement……..68

Figure 4.15 Radial variations of elastic fields under flat-ended cylindrical indenter with h/a = 1 and $\bar{a}$ = 1 for different values of τ_1^s/τ_2^s : (a) normalized contact pressure and (b) normalized surface displacement……..69

Figure 4.16 Radial variations of elastic fields under flat-ended cylindrical indenter with h/a = 1 and $\bar{a}$ = 1 for different ratio of shear moduli μ_1/μ_2 : (a) normalized contact pressure and (b) normalized surface displacement…….……70

Figure 4.17 Variations of normalized indentation force under flat-ended cylindrical indenter for various layer thicknesses, h/a versus contact radius, $\bar{a}$ ….71

Figure 5.1 A circular nano-plate under axisymmetric vertical loading.…..……..85

Figure 5.2 A circular nano-plate on an elastic half-space under axisymmetric vertical loading.……..……..85

Figure 5.3 Unit vertical load applied over an annular region on an elastic half-space.……..…..86

Figure 5.4 Comparisons for deflection of a circular nano-plate: (a) simply supported edge and (b) clamped edge.……..87

Figure 5.5 Comparisons for: (a) contact pressure and (b) bending moment of a circular plate on an elastic half-space without surface energy effects..88

Figure 5.6 Radial profiles of normalized vertical deflection of a circular nano-plate resting on an elastic half-space under uniform vertical loading for different values of K_r with $\bar{a}$ =10.……..……..89

Figure 5.7 Radial profiles of normalized bending moment of a circular nano-plate resting on an elastic half-space under uniform vertical loading for different values of K_r with $\bar{a}$ =10.……...……..89

Figure 5.8 Variations of normalized central deflection with $\bar{a}$ of a circular nano-plate resting on an elastic half-space under uniform vertical loading for different values of K_r ……...…..…..90

Figure 5.9 Variations of normalized maximum bending moment with $\bar{h}_{pl}$ of a circular nano-plate resting on an elastic half-space under uniform vertical loading for different values of K_r ……90

LIST OF ABBREVIATIONS

a	radius of contact area, punch and circular plate;
α	characteristic parameter of the paraboloidal punch;
α_n	generalized coordinate;
D^*	flexural rigidity of plate;
d	indentation depth;
E	Young's modulus;
h	thickness of an elastic layer;
h_{pl}	thickness of an elastic plate;
I	total potential energy of interaction problem;
I_P	total potential energy of the plate;
J_n	Bessel functions of the first kind of order n;
K_r	relative plate stiffness;
κ^s	surface material constant;
Λ	material characteristic length;
∇^2	Laplacian operator in a cylindrical coordinate;
M_r	bending moment of circular plate;
Ne	number of ring elements;
ν	Poisson's ratio;
P	indentation force, point force;
$p(r)$	an applied normal traction;
Φ	Love' strain potential;
Q_r	shear force of circular plate;

$q(r)$	an applied tangential traction;
r	radial coordinate;
t_i^0	prescribed traction on the surface in the *i*-direction;
u_i	displacement component of the bulk in the *i*-direction;
μ , λ	Lamé's constants of the bulk material;
μ^s , λ^s	Lamé's constants of the surface material;
τ^s	residual surface stress under unstrained condition;
σ_{ij}	stress components;
ε_{ij}	strain components;
δ_{ij}	Kronecker delta;
$\delta(r)$	profile of the punch;
S	contact surface;
ξ	Hankel transform parameter;
T_z	normal traction at the contact surface;
U_B	strain energy of the bulk;
U_P	strain energy of the plate;
U_S	strain energy of the surface;
U_r^j	Green's function for radial surface displacement;
U_z^j	Green's function for vertical surface displacement;
$w(r)$	deflection of an elastic plate;
W	potential energy;
z	vertical coordinate;

CHAPTER I
INTRODUCTION

1.1 General

In recent years, researches related to nanotechnology have received increasing attentions due to the vast applications of nano-scale structures and devices in various fields such as biology, chemistry, physics, medicines and engineering. For instance, logic and memory devices have driven the development of new materials, tools and technologies for the fabrication of even more complex devices with their sizes now down to the sub-micron and nanometer levels. Nano-crystals are also examples of a new invention at a nanoscale level. Metal nano-crystals can be incorporated into car bumpers, making the parts stronger, or into aluminum, making it more durable. Other applications of the metal nano-crystals can be found in the production of bearings, new types of sensors and components for computers and electronic hardware. Useful information regarding physical and mechanical properties at the nanoscale level is necessary for the design of microelectromechanical systems (MEMS) and nanoelectromechanical systems (NEMS) devices. It is thus evident that understanding fundamental aspects of mechanical properties at a nano scale is important for optimum design of nano-sized devices and structures.

The study of mechanical behaviors at nano-scale can be investigated by two basic approaches, namely, experimental method and theoretical simulations. Some of previous researches using direct experimental methods have been found in the literature, for instance, Wong et al. (1997) performed AFM bending tests to determine the mechanical properties of cantilever SiC beams by using conventional beam theory. Mao et al. (2003) employed the same method to investigate the hardness of both ZnO and SnO_2 nano-belts. Jing et al. (2006) determined the elastic modulus of silver nanowires with diameters ranging from 20 to 140 nm by performing three-point bending tests, and found that the Young's modulus of silver nanowires is increased significantly with decreasing wire diameter when the diameter is less than 90 nm. Jindal et al. (2014) obtained result of static tests for hardness and elastic modulus by nano-indenter on a MWCNT based PC composite. Although actual material behavior can be

obtained by performing an experiment, the results are still found highly dependent on experimental environments, and the procedure is quite expensive due to the requirement of high-precision equipment.

For the analytical approach, mathematical modeling and simulations have become an attractive alternative and been widely used to analyze the mechanical behaviors of nanoscale systems. Two major approaches have been commonly employed to study nanoscale systems, i.e. molecular or atomistic models and continuum based models. Though molecular simulations are considered very accurate for nanoscale systems because of their effectiveness in detailing of bonds or atoms, but they need huge computational efforts to model billions of atoms at a nanoscale and hence they are limited in practical applications. Therefore, the continuum-based approach is considered attractive due to the computational efficiency and lesser complexity. However, the classical concepts of continuum mechanics need to be modified to account for some effects that exist at the nanoscale. Unlike the atomistic simulations that calculate the behavior of atom by atom, the modified continuum models are incorporated to account for the nanoscale effects.

From atomistic study, it was reported that the energy associated with atoms at or near free surface or interface is different from that of atoms in the bulk material (Miller and Shenoy, 2000; Shenoy, 2005). Due to the high surface to volume ratio at a nano-scale level when compared to that at a macro-scale level, the influence of excess energy associated with surface/interface atoms, called the surface/interfacial free energy, is significant, and the mechanical behavior becomes size-dependent (Wong et al., 1997). Thus, the surface energy effects, which are generally ignored in conventional continuum mechanics, must be considered in modified continuum-based simulations for nano-scale problems. Several continuum-based models have been developed to take into account surface energy effects and size-dependent material behaviors such as the couple stress theory (Mindlin and Tiersten, 1962; Toupin, 1964), the strain gradient elasticity theory (Mindlin, 1964; Gao and Zhou, 2013), and the surface elasticity theory by Gurtin and Murdoch (1975; 1978). Among various exiting continuum-based models, the Gurtin-Murdoch model has been adopted extensively for the investigation of continuum mechanics problems that account surface energy effects for simulation of

nanomaterials and soft elastic solids due to its attractive features both in terms of computational efficiency and level of accuracy gained.

Contact mechanics is the study of the deformation of two solids that come into contact area. It is fundamental to various fields of engineering by providing information necessary for the safe and energy efficient design of technical systems and for the study of tribology, contact stiffness, electrical contact resistance and indentation hardness. This dissertation is concerned with the analysis of various contact problems at nanoscale level based on continuum mechanics approach by incorporating the influence of surface energy effects from Gurtin-Murdoch theory of surface elasticity. The analytical solution for fundamental problems of a layered elastic medium subjected to axisymmetric surface loading is obtained in Chapter III. Axisymmetric rigid indentation on a layered elastic medium with consideration of either frictionless or adhesive contact is presented in Chapter IV. The interaction between a circular elastic plate and an isotropic elastic half-space is studied in Chapter V. In each chapter, selected numerical results are presented to demonstrate the influence of surface stresses on elastic fields of the contact problems under consideration.

1.2 Objectives and Scopes of Present Study

The main objectives and scopes of the present study are given as follows:

i. To develop efficient solution schemes to investigate various contact problems that take into account the influence of surface stresses by adopting a complete Gurtin-Murdoch continuum theory of elastic material surface. The following contact problems are to be considered: a layered elastic medium under surface loading; nanoindentation on a layered elastic medium; and interaction between an elastic nanoplate and an elastic medium under vertical loading.

ii. To investigate size-dependent and nanoscale influence on elastic fields of various contact problems under consideration.

CHAPTER II
LITERATURE REVIEWS

2.1 General

Contact mechanics is the study of deformations of solids that touch each other at one or more points. The stresses and deformations arising from the contact between two elastic solids have practical applications such as hardness testing, impact damage of engineering ceramics, locomotive wheel-rail contact, coupling devices braking systems, bearings, mechanical linkages, metal working and many others. In the fields of material sciences and engineering, studies related to mechanical behaviors of nanostructured materials have become a subject of numerous investigations due to the fact that understanding fundamental aspects of their behaviors at nano-scale level is important for optimum design of nanosized devices and structures. Due to the high surface to volume ratio at the nano-scale level when compared to that at a macro-scale level, the influence of surface/interface free energy associated with atoms at or near a free surface, and the mechanical behavior becomes size-dependent (Wong et al., 1997). Therefore, the surface energy effects, which are generally ignored in conventional continuum mechanics, must be taken into account in modified continuum-based simulations for nano-scale problems. The present study is concerned with the analysis of various contact problems with consideration of surface energy effects. In the following section, a review of literature related to surface elasticity theory, contact problems is presented.

2.2 Surface Elasticity Theory

The concepts of surface energy and surface stress were originally formulated by Gibbs (1906). In the formulation of the thermodynamics of surface, Gibbs defined the surface free energy (γ) to represent the changeable work per unit area needed to create a new surface. Gibbs also pointed out that for an elastic solid there is another type of surface quantity, which is different from the surface energy, called the surface stress that represents the reversible work per unit area needed to elastically stretch a pre-

existing surface. From the thermodynamics of solid surfaces, the relationship between the surface stress and the surface free energy was derived by Cammarata (1994), who showed that the surface of a solid has different atomistic structure from the bulk and is treated as a specific mathematical surface which has no thickness. The free energy per unit area of the surface is called specific surface energy, and its changer per unit amount of strain is referred as surface stress. It should be noted that γ is a scalar quantity, while the surface stress is a second order tensor in the tangent plane of the surface and the strain normal to the surface is excluded. The relationship between the surface stress and surface free energy as

$$\sigma_{\alpha\beta} = \gamma\delta_{\alpha\beta} + \frac{\partial\gamma}{\partial\varepsilon_{\alpha\beta}} \tag{2.1}$$

where $\sigma_{\alpha\beta}$ and $\varepsilon_{\alpha\beta}$ denote the surface stress and surface strain, respectively, and $\delta_{\alpha\beta}$ is the two-dimensional Kronecker delta. The Greek indices range from 1 to 2.

The term surface energy γ is usually accepted as an excess energy term since a surface can be interpreted as a layer to which certain energy is attached (Fischer et al., 2008). Due to the different local environment, atoms at or near a free surface or interface have different equilibrium positions than do atoms in the bulk of a material. As a result, the energy of these atoms is, in general, different from that of the atoms in the bulk (Dingreville and Cherkaoui, 2005). The influence of surface energy effect is significant on their behavior for a nanoscale system. The ratio of surface free energy γ (J/m^2) and Young's modulus E (J/m^3), γ / E, has a dimension of length (m) and points to some other inherent parameters of a material (Yakobson, 2003). Obviously, this ratio has the dimension of length, and defines an intrinsic length scale for the material. For usual metallic materials, the ratio is normally less than one Angstrom. When the characteristic size of the metals is very large comparable to this intrinsic scale, the effect of surface energy (or surface stress) becomes important on the properties of the materials, and thus the properties of this material becomes size-dependent. To support this assumption, many experiments have been performed. For example, Wong et al. (1997) used atomic force microscopy method to determine the Young's modulus, strength and toughness of nanorods and nanotubes. They showed that those properties

depend on the size of materials. In the case of a soft elastic solid, the surface free energy is a little less than that of a metal, but its elastic modulus is also much smaller than that of a conventional solid. Consequently, the corresponding intrinsic length scale of a soft solid is much larger and becomes comparable to material dimensions in practical situations and then the surface energy effects can play an important role on its mechanical properties (He and Lim, 2006). Thus, in order to study the behavior of soft materials or to obtain the correct response of nanoscale system, the surface stress should be incorporated into classical continuum models.

Many researchers have developed modified continuum models to include the effects of surface and interface energy, and the most well-known model was presented by Gurtin-Murdoch model. Gurtin and Murdoch (1975; 1978) and Gurtin et al. (1998), who proposed a theoretical framework based on the continuum mechanics concepts to study the mechanical behavior of material surfaces. The surface is modeled as the zero-thickness layer, whose material properties are different from the bulk, and perfectly bonded to an underlying bulk material without slipping. For an isotropic elastic surface, a linearized expression for surface stress-strain constitutive relation has the following form

$$\sigma_{\beta\alpha}^{s} = \tau^{s}\delta_{\beta\alpha} + 2\left(\mu^{s} - \tau^{s}\right)\varepsilon_{\beta\alpha} + \left(\lambda^{s} + \tau^{s}\right)\varepsilon_{\gamma\gamma}\delta_{\beta\alpha} + \tau^{s}u_{\beta\alpha}^{s} \tag{2.2}$$

where the superscript ‘s’ is used to denote the quantities corresponding to the surface, μ^{s} and λ^{s} are surface Lamé constants and τ^{s} is the residual surface tension under unstrained conditions, which is a constant.

The validity of Gurtin-Murdoch model has been verified in various studies. For instance, Miller and Shenoy (2000) employed the Gurtin-Murdoch constitutive relation to investigate the behavior of bars, beams, and plates subjected to uniaxial loading and pure bending. Their results were compared with direct atomistic simulations of nanoscale structures and good agreement between the simulations and the model was found and the size dependence of the stiffness of bars, beams and plate was observed. Shenoy (2002) extended the work of Miller and Shenoy (2000) by adding the torsional rigidities of nanosized structural elements and applied to the case of nanoscale bars in torsion. The theoretical results were compared with the solutions from atomistic

simulations for the torsion of various metal squared bars, and good agreement was found by assuming that the surface energy depends only on the surface strain. Dingreville and Cherkaoui (2005) incorporated the surface free energy into the continuum theory of mechanics to demonstrate that the overall elastic behavior of structural elements (such as particles, wires, films) is size-dependent. The effective Young's modulus of thin films of various thicknesses computed by using molecular static (MS) simulations and their proposed formulation was found to be in good agreement. Moreover, they showed that the MS simulation is much more computationally expensive than the proposed formulation. This thus confirms the advantages of using continuum-based models.

Although the experimental measurement of surface elastic properties (i.e. surface energy, surface stress, and surface elastic stiffness) seems to be challenging, several tests at nano-scale have actually been performed. Jing et al. (2006) measured the surface elastic properties of silver nanowires by using three-point bending test and contact atomic force microscopy (C-AFM). They found that the surface elastic modulus E^s and surface residual stress τ^s of the silver nanowire are 8.7 N/m and 5.8 N/m respectively. Another approach, which is rather computationally expensive, is atomistic simulations. Shenoy (2005) presented a fully nonlinear treatment of surface stress and surface elastic constants by performing atomistic simulations.

The surface elasticity model has been extensively used to study the size-dependent behavior at the nanoscale in various problems. For example, He et al. (2004) and Huang (2008) used Gurtin-Murdoch continuum-based model to study the size dependence of the mechanical response of ultra-thin film. Similarly, Lu et al. (2006) studied the size-dependent static and dynamic analyses of plate-like thin film structures by modifying the thin plate model in Lim and He (2004). Incorporating continuum theory with surface elasticity was further developed by several researchers to study nano-inhomogeneities problems. For instance, Shama and Wheeler (2006) and Shama et al. (2003) investigated the size-dependent elastic field of spherical and ellipsoidal nan-inclusions by using Gurtin-Murdoch model with the effect of surface energy. Duan et al. (2005) extended the Eshelby formulism for a spherical inhomogeneous inclusion with the interface stress effect subjected to an arbitrary uniform eigenstrain under the

surface/interface effects. Tian and Rajapakse (2006; 2007) used the Gurtin-Murdoch model to examine the size-dependent elastic field of nano-scale circular and elliptical inhomogeneity. In addition, Intarit et al. (2010) presented analytical solutions for shear and opening dislocations in an elastic half-plane with surface stresses by using the Gurtin-Murdoch continuum theory and Fourier integral transform techniques. They indicated that the influence of surface stresses becomes significant only near the surface for both dislocations and buried loading cases. Subsequently, Intarit et al. (2011) repeated the work of Intarit et al. (2010) by considering the out-of-plane terms in the Gurtin-Murdoch continuum theory in the buried vertical and horizontal line loads, and showed significantly different solutions compared to previous studies. Sapsathiarn and Rajapakse (2013) used the governing equations of circular nano-plate presented by Liu and Rajapakse (2013) to develop a finite-element method for static and free vibration analysis of axisymmetric circular nano-plate, and showed the size-dependent response of nano-plate. Recently, Intarit et al. (2017) considered a penny-shaped crack in an infinite elastic medium subjected to vertical pressure loading at the crack surface, and presented the influence of surface stress on the elastic field.

2.3 Contact Problems with Surface Stress Effects

Stress analysis of a layered elastic medium under applied surface loading has been used to study characterization of mechanical properties of layered materials: e.g. protective coatings, multilayer capacitors and layered composite materials; analysis and design of pavement and foundations; and in-situ testing of soils and rocks, etc. In the past, the classical elasticity solution of a layer substrate system has investigated the effect of different elastic properties of layer substrate system and layered thickness on the contact pressure, contact size of the system as compared to the homogeneous medium (Gupta and Walowit, 1974; Barber and Ciavarella, 2000; Perriot and Barthel, 2004; Greenwood and Barber, 2012). Burmister (1945) considered an elastic half-space bonded to one or two elastic layers and subjected to an axially symmetric surface loading. He also presented some numerical results on the vertical surface displacements at the center of the loaded region for several different combinations of physical and geometrical properties in the single surface layer problem. Fox (1948) produced the

first extensive tabular summary of normal and radial stresses below the interfaces. Especially, Gerrard (1969) presented the solutions for the stresses, strains and displacements in two-layer system that showed the effect of layer thickness and the mismatch of elastic modulus on the resulting contact pressure (i.e. vertical, inward shear, and uni-directional shear).

In the nano-scale level, several researchers have investigated a variety of contact mechanics by adopting the Gurtin-Murdoch theory of surface elasticity. For surface-loading problems, Huang and Yu (2006) studied an elastic half-plane under surface loading with consideration of surface energy effects. An elastic layer with finite thickness, subjected to surface loading under plane-strain and axisymmetric conditions, was also considered by Zhao and Rajapakse (2009). Intarit et al. (2010) derived fundamental solutions of an elastic half-plane under internal loading and dislocations. An elastic half-plane under surface shear loading was also investigated by Lei et al. (2012). Ou and Pang (2013) considered the two-dimension Hertzian contact problems at nanoscale based on surface elasticity theory by employing the complex variable function method. Recently, nano-contact problem of layered viscoelastic solids with surface energy effects was presented by Abdel Rahman and Mahmoud (2016). All these studies, however, considered the surface stress tensor as a 2D quantity with its out-of-plane components being neglected. Wang et al. (2010) showed that the out-of-plane terms of the surface displacement gradient could be significant even in the case of small deformations particularly for curved and rotated surfaces. The complete version of Gurtin-Murdoch model, with consideration of the out-of-plane term, has later been employed to examine various continuum mechanics problems, e.g. problems related to internally loaded elastic layer under plane strain condition (Intarit et al., 2011) and axisymmetric loading (Rungamornrat et al., 2016) respectively. In addition, the influence of surface energy effects is also significant in problems related to soft elastic solids (He and Lim, 2006). A review of literature indicates that studies related to a layered elastic medium with consideration of surface energy effects based on the Gurtin-Murdoch theory are very limited. This class of problems has extensive applications in the study of nanocoatings and nanoscale surface layers that are used in electronic devices, tribological and biomaterial applications, advanced industrial materials, communication devices, and so forth.

Indentation techniques have been widely used in several researches to study the mechanical properties of materials such as hardness and elastic modulus. Several experimental techniques have been proposed to investigate by indentation techniques. For instance, the depth-sensing indentation tests were performed to find hardness and Young's modulus of thin films from the slope of the unloading curves in the load versus penetration depth while hardness values are calculated from the data along the loading curves (Doerner and Nix, 1986). Similarly, Oliver and Pharr (1992) improved indentation experiments for determining hardness and elastic modulus of six materials (e.g. fused silica, soda-lime glass, single crystals of aluminum, tungsten, quartz, and sapphire) from indentation load-displacement data. Hainsworth and Page (1994) used nanoindentation techniques to study chemomechanical effects on the detailed surface mechanical response (e.g. elastic flexure, stiffness, dislocation nucleation and plasticity) of single-crystal sapphire. Armstrong et al. (1995) studied an increase in hardness value for copper material by using a nanoindentation test. Oliver and Pharr (2004) applied indentation techniques to measure hardness and elastic modulus in the characterization of small-scale mechanical behavior introduced in 1992. They improved testing equipment and techniques to make more accurate mechanical property measurement. Since the smart materials have been variously used in nanoscale systems, the understanding of mechanics of nanostructures is essential in the development for engineering applications. Cao et al. (2007) explained that accurate prediction of the indentation load-displacement relationship of an elastic sharp indenter indenting into an elastic half-space is critical for analyzing the nanoindentation data if super-hard materials are used in the procedure proposed by Oliver and Pharr (1992). Chang and Zhang (2009) investigated the deformation behavior of silicon under ultra-low loading conditions with nanoindentation using a Berkovich indenter. They found that when a proper area function of the indenter tip is used the mechanical properties of silicon can be accurately characterized and the Young's modulus of silicon (100) is 171 GPa. Shokien et al. (2013) studied the effect of graphene nano-platelets (GNPs) on the mechanical properties of polymer nanocomposites by using nanoindentation and nanoscratch methods. They showed that the mechanical properties of the pure polymer matrix are improved with the addition of low amounts of the graphene nano-platelets. While the experimental techniques have been commonly used by various researchers

to investigate the mechanical properties, the testing procedure requires high precision machines and supreme laboratories.

Several researchers presented elastic solutions of indentation problems by employing continuum mechanics theory. The classical solution of axisymmetric rigid frictionless indentation on elastic half-space is first considered by Boussinesq (1885). Harding and Sneddon (1945) and Sneddon (1965) established a solution of the axisymmetric Boussinesq problem, which enabled them to deduce simple formulas giving the penetration of a punch of arbitrary profile by using Hankel integral transform techniques. Thereafter, Clements (1971) considered a rigid punch to determine stresses produced by the indentation on the plane surface of an anisotropic half space by employing the theory of anisotropic elasticity for a three dimension solution developed by Eshelby et al. (1953) and Stroh (1958). The indentation problems associated with an elastic layer perfectly bonded to an elastic half-space have also been investigated. Dhaliwal and Rau (1970) developed a solution of the axisymmetric Boussinesq problem for an elastic layer lying over an elastic foundation under a rigid punch of arbitrary profiles by using a Fredholm integral equation. Later, Rau and Dhaliwal (1972) proposed a numerical technique to solve the integral equation developed by Dhaliwal and Rau (1970). They showed the load and deformation characteristics under cylindrical, conical, paraboloidal and spherical punch shapes. Yu et al. (1990) considered an axisymmetric mixed boundary value problem with an elastic layer in frictionless contact or perfectly bonded to a semi-infinite elastic half-space and presented numerical results obtained from solving Fredholm integral equations of the second kind to demonstrate the effect of a substrate on the elastic properties of films. They provided useful guidelines for the proper choice of an approximate layer thickness and substrate elastic properties to determine the elastic constants of the layer. Yang (1998) solved the problem of impressing a rigid flat-ended cylindrical indenter onto an incompressible elastic film by applying Fredholm integral equation of the second kind to reduce an integral transform solution. In addition, Huajian et al. (1992) and Xu and Pharr (2006) provided approximate results by using a perturbation analysis, in which the stress and strain fields are regarded as a superposition of the contact filed in a homogeneous half-space and one due to the transformation of one part of the half-space (representing the film or the substrate) into another type of material.

The above solutions to indentation problems were obtained based on the assumption of frictionless contact surface. If the coefficient of friction between a rigid indenter and an elastic medium is large enough, the indenter is prevented from any sliding on the contact area. This condition is known as an adhesive contact problem, and it is mathematically more complicated than the case of frictionless contact. For the indentation with adhesive contact, the top surface of elastic medium is decomposed into a surface outside the contact region on which both normal and shear stresses are identically zero, and a surface inside the contact region on which the normal displacement is prescribed in terms of the indentation depth and the radial displacement is zero at every point of the contact region. The analysis of indentation with adhesive contact was first performed incrementally for a growth in the contact radius (Mossakovskii, 1954, 1963; Goodman, 1962). Spence (1968) introduced a self-similarity approach for a flat-ended cylinder and a parabolic punch, corrected some misprints in the Mossakovskii examples, and also presented the solution for a conical punch. By adopting Mossakovskii's approach, Borodich and Keer (2004) obtained the exact solution to the axisymmetric adhesive elastic contact problem for punches whose shapes are described by monomial functions. A detailed and comprehensive analysis of the literature related to the adhesive contact problems is given by Galin and Gladwell (2008) and Borodich (2014). Recently, Selvadurai and Katebi (2015) examined the axisymmetric adhesive contact problem between a rigid circular plate and an incompressible elastic half-space where the shear modulus of the elastic material varies exponentially with depth.

At nano-scale level, analytical investigation is also performed to study nanoindentation problems. Zhao (2009) derived an analytical solution of a frictionless nanoindentation problem, in which elastic fields within the half-space caused by flat-ended cylindrical, conical and spherical rigid indenters are presented. Although Gurtin-Murdoch continuum model used in the formulation is not complete (e.g. no out-of-plane term), numerical result showed a size-dependent behavior due to the surface energy effect, i.e. when the contact area becomes smaller, the material behaves stiffer. Long et al. (2012) considered a two-dimension contact problem of a rigid cylinder indenting on an elastic half-space with surface tension. The Guass-Chebyshev quadrature formula is applied to solve the derived integral equation. Long and Wang (2013) extended this

work to handle axisymmetric indentation problems between a sphere and a half-space. Zhou and Gao (2013) derived for both half-space and half-plane contact problems with the linearized surface elasticity theory of Gurtin and Murdoch by using the Papkovitch-Neuber potential functions, Fourier transforms and Bessel functions. Gao et al. (2013) developed a non-classical formulation of the Boussinesq problem with the surface effect, in which both the residual surface stress and the surface elasticity are considered. Pinyochotiwong et al. (2013) later generalized the work of Zhao (2009) to investigate an axisymmetric, rigid, frictionless indentor with the integration of the influence of surface stresses for two indentor profiles (i.e., flat-ended and paraboloidal indentors). They used the standard Love's representation and Hankel integral transform to predict the influence of surface stresses on the mechanical response of a homogeneous elastic half-space indented by using a complete version of Gurtin-Murdoch surface elasticity model. The finite element method was also employed by Attia and Mahmoud (2015) to consider a frictionless nanoindentation problem on a functionally graded layered elastic medium with the influence of surface stresses. Recently, Intarit et al. (2018) extended Pinyochotiwong et al. (2013) to consider an axisymmetric indentation on an elastic layer bonded to rigid base with the consideration of surface energy effects. Based on the above literature review, it is evident that the analysis of axisymmetric rigid indentation with frictionless and adhesive contacts on a layered elastic half-space under the influence of surface energy effects has never been considered in the past. The results of this problem are useful in the characterization of mechanical properties of nanocoatings and nanoscale surface layers such as hardness and elastic modulus.

The analysis of interaction between a circular elastic plate and an elastic supporting medium is of fundamental importance in the field of civil engineering. This includes the study of structural foundations, floating structures, laminated or composite materials and the analytical study of geological structures. The classical study by Borowicka (1939) investigated the influence of the relative rigidity of a circular plate, subjected to uniform external load and resting on an isotropic elastic half-space using a power series expansion technique. Brown (1969) presented a modified solution for a uniformly loaded plate in which they considered the effect of near edge singular terms in the approximation of the contact stress distribution by using integral transforms and collocation. Selvadurai (1979), who is the first who utilized an energy method,

presented the investigation of the elastostatic contact problem where the deflected shape of the circular plate is presented in the form of a power series in terms of the radial coordinate. Likewise, Selvadurai (1979) also used an energy approach to study the behavior of a circular flexible plate embedded in bonded contact with an elastic infinite half-space subjected to a uniformly distributed axisymmetric external load. Zaman et al. (1988) developed an analytical formulation based on an energy approach to predict the flexural behavior of a uniformly loaded thin flexible circular plates resting in smooth and continuous contact with an isotropic elastic half-space. The deflected shape of the plate is approximated by an even power series expansion in terms of the radial coordinate. Selvadurai et al. (2007) examined the elastic contact problem between a flexible elastic diaphragm and an isotropic elastic half-space under an applied normal stress. Pak et al. (2008) presented a new hybrid method for a circular solid or annular plate in tensionless and frictionless contact with an elastic half-space by employing Kirchhoff plate theory and classical three-dimensional elastostatics to set of Green's functions. Selvadurai and Dumont (2011) employed the energy method to examine the contact problem for an isotropic elastic half-space containing a Mindlin-type axial force and a flexible circular plate subjected simultaneously to an external load. Katebi and Selvadurai (2015) employed an energy method to examine the axisymmetric contact problem for a flexible circular plate in smooth contact with an incompressible elastic half-space. The coefficients in the series that satisfies the kinematics of deformation of the plate and the Kirchhoff boundary condition at the edge of the plate are evaluated by making use of the principle of minimum potential energy.

Nano-plate strurtures are used in various nanotechnology-based such as nano-electro-mechanical systems (NEMS) due to their superior optical, electronic and mechanical properties (Craighead, 2000). Gurtin-Murdoch continuum theory is applied to develop a new continuum mechanics model for static deformation of thin and thick circular nano-plates proposed by Liu and Rajapakse (2013). The analytical solution for deflections of a uniformly loaded thin plate resting on an elastic spring support is also presented to demonstrate the key features of mechanical behaviours of nano-plate. Recently, Gao and Zhang (2016) presented a new non-classical Krichhoff plate model by using a modified couple stress theory, a surface elasticity theory and a two-parameter elastic foundation model via a variational formulation based on Hamilton's principle.

Their numerical results show that the deflection of a simply supported plate with or without the elastic foundation predicted by the current model is smaller than that predicted by the classical model. Based on a survey of literature mentioned above, it is found that the study on the influence of surface stresses on contact problems related to flexural behavior of loaded elastic circular plate resting on the surface of an elastic medium has never been considered in the literature. Results from this problem by incorporating a complete Gurtin-Murdoch model are crucial to investigate the size-dependent behavior and gain an insight into nano-scale influence on interaction between flexural structures and the supporting medium, which can be found in various applications at the nano-scale level.

CHAPTER III
LAYERED ELASTIC MEDIUM UNDER SURFACE LOADING AND SURFACE STRESS EFFECTS

3.1 General

Stress analysis of a layered elastic medium under applied surface loading has extensive applications in the study of nanocoatings and nanoscale surface layers that are used in electronic devices, tribological and biomaterial applications, advanced industrial materials, communication devices, and so forth. This chapter presents the analytical solutions to a layered elastic half-space under axisymmetric surface loading by adopting the complete Gurtin-Murdoch theory of surface elasticity. The boundary value problems of a layered elastic half-space under axisymmetric surface loading involving non-classical boundary conditions due to surface stress influence are formulated by employing the standard Love's representation and Hankel integral transform. Selected numerical results for displacements and stresses due to applied vertical and radial loading are presented to portray the influence of layer thickness, surface material parameters, and size dependency on elastic fields. The present fundamental solution is useful in the development of numerical solution scheme for the investigation of more complicated problems such as nano-indentation and contact problems involving a layered elastic medium.

3.2 Basic Equation and General Solution

Consider a layered elastic half-space consisting of two elastic materials with different properties perfectly bonded together, in which the upper material is an elastic layer of finite thickness h and subjected to axisymmetric vertical and radial surface loads denoted by $p(r)$ and $q(r)$ respectively, as shown in Figure 3.1. According to the Gurtin-Murdoch surface elasticity theory, both materials consist of two parts, the bulk material and the surface, which is a zero-thickness layer perfectly bonded to the bulk material without slipping. The equilibrium equations, the constitutive equations, and the strain-displacement relationship of the bulk material under axisymmetric

deformations are the same as those in the classical elasticity theory, which are given respectively by

$$\frac{\partial \sigma_{rr}}{\partial r}+\frac{\partial \sigma_{rz}}{\partial z}+\frac{\sigma_{rr}-\sigma_{\theta\theta}}{r}=0; \quad \frac{\partial \sigma_{rz}}{\partial r}+\frac{\partial \sigma_{zz}}{\partial z}+\frac{\sigma_{rz}}{r}=0 \tag{3.1}$$

$$\sigma_{rr}=\left(\lambda+2\mu\right)\varepsilon_{rr}+\lambda\varepsilon_{\theta\theta}+\lambda\varepsilon_{zz}; \quad \sigma_{\theta\theta}=\lambda\varepsilon_{rr}+\left(\lambda+2\mu\right)\varepsilon_{\theta\theta}+\lambda\varepsilon_{zz} \tag{3.2}$$

$$\sigma_{zz}=\lambda\varepsilon_{rr}+\lambda\varepsilon_{\theta\theta}+\left(\lambda+2\mu\right)\varepsilon_{zz}; \quad \sigma_{rz}=2\mu\varepsilon_{rz} \tag{3.3}$$

$$\varepsilon_{rr}=\frac{\partial u_r}{\partial r}; \quad \varepsilon_{\theta\theta}=\frac{u_r}{r}; \quad \varepsilon_{zz}=\frac{\partial u_z}{\partial z}; \quad \varepsilon_{rz}=\frac{1}{2}\left(\frac{\partial u_r}{\partial z}+\frac{\partial u_z}{\partial r}\right) \tag{3.4}$$

where $\{\sigma_{rr}, \sigma_{\theta\theta}, \sigma_{zz}, \sigma_{rz}\}$ denote the components of stress tensors; $\{\varepsilon_{rr}, \varepsilon_{\theta\theta}, \varepsilon_{zz}, \varepsilon_{rz}\}$ denote the components of strain tensors; and $\{u_r, u_z\}$ denote the components of displacement tensors respectively. In addition, μ and λ are Lamé constants of a bulk material. On the surface, the equilibrium conditions in terms of the generalized Young-Laplace equation (Povstenko, 1993), the surface constitutive relations, and the strain-displacement relationship can be expressed, respectively, as (Gurtin and Murdoch, 1975; Gurtin and Murdoch, 1978; Gurtin et al., 1998)

$$\frac{\partial \sigma^s_{rr}}{\partial r}+\frac{\sigma^s_{rr}-\sigma^s_{\theta\theta}}{r}+\sigma_{zr}\big|_{z=0}+t^0_r=0; \quad \frac{\partial \sigma^s_{zr}}{\partial r}+\frac{\sigma^s_{zr}}{r}+\sigma_{zz}\big|_{z=0}+t^0_z=0 \tag{3.5}$$

$$\sigma^s_{rr}=\tau^s+\left(2\mu^s+\lambda^s\right)\varepsilon^s_{rr}+\left(\lambda^s+\tau^s\right)\varepsilon^s_{\theta\theta}; \sigma^s_{\theta\theta}=\tau^s+\left(2\mu^s+\lambda^s\right)\varepsilon^s_{\theta\theta}+\left(\lambda^s+\tau^s\right)\varepsilon^s_{rr} \tag{3.6}$$

$$\sigma^s_{zr}=\tau^s\frac{du^s_z}{dr} \tag{3.7}$$

$$\varepsilon^s_{rr}=\frac{du^s_r}{dr}; \quad \varepsilon^s_{\theta\theta}=\frac{u^s_r}{r} \tag{3.8}$$

where the superscript "s" is used to denote the quantities corresponding to the surface; λ^s and μ^s are surface Lamé constants; τ^s is the residual surface stress (or surface tension) under unstrained conditions. In addition, t^0_r and t^0_z denote the prescribed traction on the surface in the radial and vertical directions respectively. Equation (3.7) can be viewed

as the out-of-plane contribution of the pre-existing surface tension τ^s in the deformed configuration whereas the surface gradient of the displacement du_z^s/dr acts as the out-of-plane component of the unit vector tangent to the surface in the deformed state. This term has been ignored in several previous studies even though the contribution of τ^s could be significant even in the case of small deformations (e.g. see Intarit et al., 2011; Pinyochotiwong et al., 2013; Rungamornrat et al., 2016).

For the axisymmetric case, the corresponding elastic fields can be obtained by solving the following biharmonic equation (Sneddon, 1951) in a cylindrical coordinate system (r,θ, z)

$$\nabla^2\nabla^2\Phi(r,z)=0 \tag{3.9}$$

where $\nabla^2=\frac{\partial^2}{\partial r^2}+\frac{1}{r}\frac{\partial}{\partial r}+\frac{\partial^2}{\partial z^2}$ denotes the Laplacian operator in a cylindrical coordinate and $\Phi(r,z)$ is Love's strain potential.

By applying Hankel integral transform into equation (3.9), we obtain,

$$\left(\frac{d^2}{dz^2}-\xi^2\right)^2 G(\xi,z)=0 \tag{3.10}$$

where $G(\xi,z)=\int_0^\infty r\Phi J_0(\xi r)\,dr$ and $J_n(\xi)$ denotes the Bessel functions of the first kind of order *n*. The general solution of above equation may be written in the form

$$G(\xi,z)=(A+Bz)e^{-\xi z}+(C+Dz)e^{\xi z} \tag{3.11}$$

where *A*, *B*, *C* and *D* are arbitrary functions that can be determined from the boundary conditions.

Thereafter, the general solutions for bulk stresses and displacements of an elastic solid can be expressed in the forms of Hankel integral transform as (Sneddon, 1951; Selvadurai, 2000)

$$u_r=\frac{\lambda+\mu}{\mu}\int_0^\infty \xi^2\frac{dG}{dz}J_1(\xi r)\,d\xi \tag{3.12}$$

$$u_z = \int_0^\infty \xi \left[\frac{d^2G}{dz^2} - \frac{\lambda+2\mu}{\mu}\xi^2 G \right] J_0(\xi r)\, d\xi \tag{3.13}$$

$$\sigma_{rr} = \int_0^\infty \xi \left[\lambda \frac{d^3G}{dz^3} + (\lambda+2\mu)\xi^2 \frac{dG}{dz} \right] J_0(\xi r)\, d\xi - \frac{2(\lambda+\mu)}{r} \int_0^\infty \xi^2 \frac{dG}{dz} J_1(\xi r)\, d\xi \tag{3.14}$$

$$\sigma_{\theta\theta} = \lambda \int_0^\infty \xi \left[\frac{d^3G}{dz^3} - \xi^2 \frac{dG}{dz} \right] J_0(\xi r)\, d\xi + \frac{2(\lambda+\mu)}{r} \int_0^\infty \xi^2 \frac{dG}{dz} J_1(\xi r)\, d\xi \tag{3.15}$$

$$\sigma_{zz} = \int_0^\infty \xi \left[(\lambda+2\mu)\frac{d^3G}{dz^3} - (3\lambda+4\mu)\xi^2 \frac{dG}{dz} \right] J_0(\xi r)\, d\xi \tag{3.16}$$

$$\sigma_{rz} = \int_0^\infty \xi^2 \left[\lambda \frac{d^2G}{dz^2} + (\lambda+2\mu)\xi^2 G \right] J_1(\xi r)\, d\xi \tag{3.17}$$

Finally, the substitution of the function *G*, given by Eq.(3.11), results in the stresses and displacements, expressed in terms of the arbitrary functions *A*, *B*, *C* and *D* as,

$$u_r = \frac{\lambda+\mu}{\mu} \int_0^\infty \xi^2 \left\{ \left[-A\xi + (1-z\xi)B \right] e^{-\xi z} + \left[C\xi + (1+z\xi)D \right] e^{\xi z} \right\} J_1(\xi r)\, d\xi \tag{3.18}$$

$$u_z = -\frac{\lambda+\mu}{\mu} \int_0^\infty \xi^2 \left\{ \left[A\xi + \left(\frac{2\mu}{\lambda+\mu} + z\xi \right) B \right] e^{-\xi z} + \left[C\xi - \left(\frac{2\mu}{\lambda+\mu} - z\xi \right) D \right] e^{\xi z} \right\} J_0(\xi r)\, d\xi \tag{3.19}$$

$$\frac{\sigma_{rr}}{\mu} = \frac{2(\lambda+2\mu)}{\mu} \int_0^\infty \xi^3 \left\{ \left[-A\xi + \left(\frac{2\lambda+\mu}{\lambda+\mu} - z\xi \right) B \right] e^{-\xi z} + \left[C\xi + \left(\frac{2\lambda+\mu}{\lambda+\mu} + z\xi \right) D \right] e^{\xi z} \right\} J_0(\xi r)\, d\xi$$

$$- \frac{2(\lambda+\mu)}{r\mu} \int_0^\infty \xi^2 \left\{ \left[-A\xi + (1-z\xi)B \right] e^{-\xi z} + \left[C\xi + (1+z\xi)D \right] e^{\xi z} \right\} J_1(\xi r)\, d\xi \tag{3.20}$$

$$\frac{\sigma_{\theta\theta}}{\mu} = \frac{2\lambda}{\mu} \int_0^\infty \xi^3 \left\{ Be^{-\xi z} + De^{\xi z} \right\} J_0(\xi r)\, d\xi$$

$$+ \frac{2(\lambda+\mu)}{r\mu} \int_0^\infty \xi^2 \left\{ \left[-A\xi + (1-z\xi)B \right] e^{-\xi z} + \left[C\xi + (1+z\xi)D \right] e^{\xi z} \right\} J_1(\xi r)\, d\xi \tag{3.21}$$

$$\frac{\sigma_{zz}}{\mu}=\frac{2(\lambda+\mu)}{\mu}\int_0^\infty \xi^3\left\{\left[A\xi+\left(\frac{\mu}{\lambda+\mu}+z\xi\right)B\right]e^{-\xi z}+\left[-C\xi+\left(\frac{\mu}{\lambda+\mu}-z\xi\right)D\right]e^{\xi z}\right\}J_0(\xi r)\,d\xi \tag{3.22}$$

$$\frac{\sigma_{rz}}{\mu}=\frac{2(\lambda+\mu)}{\mu}\int_0^\infty \xi^3\left\{\left[A\xi-\left(\frac{\lambda}{\lambda+\mu}-z\xi\right)B\right]e^{-\xi z}+\left[C\xi+\left(\frac{\lambda}{\lambda+\mu}+z\xi\right)D\right]e^{\xi z}\right\}J_1(\xi r)\,d\xi \tag{3.23}$$

3.3 Solution of Boundary Value Problem

Boundary value problem of a layered elastic half-space subjected to axisymmetric normal and tangential traction, denoted by $p(r)$ and $q(r)$ respectively, applied at its surface as shown in Figure 3.1 is considered in this section. To solve this problem, the layered half-space is divided into two domains. The domain '1' represents the upper layer and the domain '2' represents the underlying half-space. The general solutions of the bulk material in the domain '1', are given by Eqs. (3.18) to (3.23) whereas those of the the domain '2' can also be obtained from Eqs. (3.18) to (3.23) by replacing the arbitrary functions A to D with the arbitrary functions E to H respectively. Note that $G\equiv 0$ and $H\equiv 0$ are imposed to ensure the regularity of the solutions at infinity for the domain '2'. In addition, the subscript i =1, 2 is used to denote the quantities corresponding to the domains '1' and '2', respectively. The solutions of A to F can be determined by solving the following boundary and continuity conditions.

$$\sigma_{zz1}\big|_{z=0}+\tau_1^s\left(\frac{d^2u_{z1}}{dr^2}+\frac{1}{r}\frac{du_{z1}}{dr}\right)_{z=0}=-p(r) \tag{3.24}$$

$$\sigma_{rz1}\big|_{z=0}+\kappa_1^s\left(\frac{d^2u_{r1}}{dr^2}+\frac{1}{r}\frac{du_{r1}}{dr}-\frac{u_{r1}}{r^2}\right)_{z=0}=-q(r) \tag{3.25}$$

$$\sigma_{zz1}\big|_{z=h}-\sigma_{zz2}\big|_{z=h}+\tau_2^s\left(\frac{d^2u_{z2}}{dr^2}+\frac{1}{r}\frac{du_{z2}}{dr}\right)_{z=h}=0 \tag{3.26}$$

$$\sigma_{rz1}\big|_{z=h}-\sigma_{rz2}\big|_{z=h}+\kappa_2^s\left(\frac{d^2u_{r2}}{dr^2}+\frac{1}{r}\frac{du_{r2}}{dr}-\frac{u_{r2}}{r^2}\right)_{z=h}=0 \tag{3.27}$$

$$u_{z1}\big|_{z=h} - u_{z2}\big|_{z=h} = 0 \tag{3.28}$$

$$u_{r1}\big|_{z=h} - u_{r2}\big|_{z=h} = 0 \tag{3.29}$$

where $\kappa_i^s = 2\mu_i^s + \lambda_i^s$ is a surface material constant. It should be noted that Eqs. (3.24) to (3.27) are non-classical boundary conditions obtained from Eqs. (3.5) to (3.8). In view of Eqs. (3.18) to (3.23) together with the assumption that the surface residual stress τ^s is constant, the following six linear algebraic equations are established to solve for the arbitrary functions *A* to *F*.

$$\left(\lambda_1' + \frac{\lambda_1'\bar{\tau}_1^s\xi}{2}\right)A\xi + \left(1+\bar{\tau}_1^s\xi\right)B + \left(-\lambda_1' + \frac{\lambda_1'\bar{\tau}_1^s\xi}{2}\right)C\xi + \left(1-\bar{\tau}_1^s\xi\right)D = -\frac{\bar{P}(\xi)}{2\xi^2} \tag{3.30}$$

$$\begin{aligned}&\left(\lambda_1' + \frac{\lambda_1'\bar{\kappa}_1^s\xi}{2}\right)A\xi + \left(-\lambda_1' + 1 - \frac{\lambda_1'\bar{\kappa}_1^s\xi}{2}\right)B + \left(\lambda_1' - \frac{\lambda_1'\bar{\kappa}_1^s\xi}{2}\right)C\xi \\ &+ \left(\lambda_1' - 1 - \frac{\lambda_1'\bar{\kappa}_1^s\xi}{2}\right)D = -\frac{\bar{Q}(\xi)}{2\xi^2}\end{aligned} \tag{3.31}$$

$$\begin{aligned}&\lambda_1' e^{-\bar{h}\xi}A\xi + \left(1+\lambda_1'\bar{h}\xi\right)e^{-\bar{h}\xi}B - \lambda_1' e^{\bar{h}\xi}C\xi + \left(1-\lambda_1'\bar{h}\xi\right)e^{\bar{h}\xi}D \\ &+ \left(-\lambda_2' + \frac{\lambda_2'\bar{\tau}_2^s\xi}{2\bar{\mu}_2}\right)e^{-\bar{h}\xi}E\xi + \left(-\bar{\mu}_2 - \lambda_2'\bar{h}\xi + \left(\frac{2\bar{\mu}_2}{\lambda_2'} + \bar{h}\xi\right)\frac{\lambda_2'\bar{\tau}_2^s\xi}{2\bar{\mu}_2}\right)e^{-\bar{h}\xi}F = 0\end{aligned} \tag{3.32}$$

$$\begin{aligned}&\lambda_1' e^{-\bar{h}\xi}A\xi + \left(-\lambda_1' + 1 + \lambda_1'\bar{h}\xi\right)e^{-\bar{h}\xi}B + \lambda_1' e^{\bar{h}\xi}C\xi + \left(\lambda_1' - 1 + \lambda_1'\bar{h}\xi\right)e^{\bar{h}\xi}D \\ &+ \left(-\lambda_2' + \frac{\lambda_2'\bar{\kappa}_2^s\xi}{2\bar{\mu}_2}\right)e^{-\bar{h}\xi}E\xi + \left(\lambda_2' - \bar{\mu}_2 - \lambda_2'\bar{h}\xi - \left(1-\bar{h}\xi\right)\frac{\lambda_2'\bar{\kappa}_2^s\xi}{2\bar{\mu}_2}\right)e^{-\bar{h}\xi}F = 0\end{aligned} \tag{3.33}$$

$$\begin{aligned}&-\lambda_1' e^{-\bar{h}\xi}A\xi + \left(-2-\lambda_1'\bar{h}\xi\right)e^{-\bar{h}\xi}B - \lambda_1' e^{\bar{h}\xi}C\xi + \left(2-\lambda_1'\bar{h}\xi\right)e^{\bar{h}\xi}D + \left(\frac{\lambda_2'}{\bar{\mu}_2}\right)e^{-\bar{h}\xi}E\xi \\ &+ \left(2 + \left(\frac{\lambda_2'}{\bar{\mu}_2}\right)\bar{h}\xi\right)e^{-\bar{h}\xi}F = 0\end{aligned} \tag{3.34}$$

$$-\lambda_1' e^{-\bar{h}\xi} A\xi + \lambda_1' \left(1-\bar{h}\xi\right) e^{-\bar{h}\xi} B + \lambda_1' e^{\bar{h}\xi} C\xi + \lambda_1' \left(1+\bar{h}\xi\right) e^{\bar{h}\xi} D + \left(\frac{\lambda_2'}{\bar{\mu}_2}\right) e^{-\bar{h}\xi} E\xi + \left(\frac{\lambda_2'}{\bar{\mu}_2}\right)\left(-1+\bar{h}\xi\right) e^{-\bar{h}\xi} F = 0 \tag{3.35}$$

where the following non-dimensional quantities in the above equations are defined as: $\bar{h} = h/\Lambda_1; \lambda_1' = \bar{\lambda}_1 + 1; \lambda_2' = \bar{\lambda}_2 + \bar{\mu}_2; \bar{\lambda}_1 = \lambda_1/\mu_1; \bar{\lambda}_2 = \lambda_2/\mu_1; \bar{\mu}_2 = \mu_2/\mu_1; \bar{\tau}_1^s = \tau_1^s/\mu_1\Lambda_1;$ $\bar{\tau}_2^s = \tau_2^s/\mu_1\Lambda_1;\ \bar{\kappa}_1^s = \kappa_1^s/\mu_1\Lambda_1;\ \bar{\kappa}_2^s = \kappa_2^s/\mu_1\Lambda_1;$ and $\Lambda_1 = \kappa_1^s\left(\lambda_1 + 2\mu_1\right)/2\mu_1\left(\lambda_1 + \mu_1\right)$. In addition, the functions $\bar{P}(\xi)$ and $\bar{Q}(\xi)$ are obtained from the surface loads $p(r)$ and $q(r)$ respectively as

$$\bar{P}(\xi) = \int_0^\infty \bar{p}(\bar{r})\, J_0(\xi\bar{r})\, \bar{r}\, d\bar{r} \tag{3.36}$$

$$\bar{Q}(\xi) = \int_0^\infty \bar{q}(\bar{r})\, J_1(\xi\bar{r})\, \bar{r}\, d\bar{r} \tag{3.37}$$

in which $\bar{p} = p/\mu_1$; $\bar{q} = q/\mu_1$; and $\bar{r} = r/\Lambda_1$. The arbitrary functions A to F for given functions of the applied surface loads $p(r)$ and $q(r)$ can then be obtained separately by solving the linear equation system, Eqs. (3.30) to (3.35), and they are given by

$$A\xi = A_N\xi + A_R\xi \tag{3.38}$$

$$B = B_N + B_R \tag{3.39}$$

$$C\xi = C_N\xi + C_R\xi \tag{3.40}$$

$$D = D_N + D_R \tag{3.41}$$

$$\begin{Bmatrix} E\xi \\ F \end{Bmatrix} = \begin{bmatrix} b_{11} & b_{12} & b_{13} & b_{14} \\ b_{21} & b_{22} & b_{23} & b_{24} \end{bmatrix} \begin{Bmatrix} A\xi \\ B \\ C\xi \\ D \end{Bmatrix} \tag{3.42}$$

$$\begin{Bmatrix} A_N\xi \\ B_N \\ C_N\xi \\ D_N \end{Bmatrix} = -\frac{\bar{P}(\xi)}{2\xi^2 \cdot |a_{ij}|} \begin{Bmatrix} a_{22}(a_{33}a_{44}-a_{34}a_{43})+a_{23}(a_{34}a_{42}-a_{32}a_{44})+a_{24}(a_{32}a_{43}-a_{33}a_{42}) \\ a_{21}(a_{34}a_{43}-a_{33}a_{44})+a_{23}(a_{31}a_{44}-a_{34}a_{41})+a_{24}(a_{33}a_{41}-a_{31}a_{43}) \\ a_{21}(a_{32}a_{44}-a_{34}a_{42})+a_{22}(a_{34}a_{41}-a_{31}a_{44})+a_{24}(a_{31}a_{42}-a_{32}a_{41}) \\ a_{21}(a_{33}a_{42}-a_{32}a_{43})+a_{22}(a_{31}a_{43}-a_{33}a_{41})+a_{23}(a_{32}a_{41}-a_{31}a_{42}) \end{Bmatrix} \tag{3.43}$$

$$\begin{Bmatrix} A_R\xi \\ B_R \\ C_R\xi \\ D_R \end{Bmatrix} = -\frac{\bar{Q}(\xi)}{2\xi^2 \cdot |a_{ij}|} \begin{Bmatrix} a_{12}(a_{34}a_{43}-a_{33}a_{44})+a_{13}(a_{32}a_{44}-a_{34}a_{42})+a_{14}(a_{33}a_{42}-a_{32}a_{43}) \\ a_{11}(a_{33}a_{44}-a_{34}a_{43})+a_{13}(a_{34}a_{41}-a_{31}a_{44})+a_{14}(a_{31}a_{43}-a_{33}a_{41}) \\ a_{11}(a_{34}a_{42}-a_{32}a_{44})+a_{12}(a_{31}a_{44}-a_{34}a_{41})+a_{14}(a_{32}a_{41}-a_{31}a_{42}) \\ a_{11}(a_{32}a_{43}-a_{33}a_{42})+a_{12}(a_{33}a_{41}-a_{31}a_{43})+a_{13}(a_{31}a_{42}-a_{32}a_{41}) \end{Bmatrix} \tag{3.44}$$

$$|a_{ij}| = \begin{vmatrix} a_{11} & a_{12} & a_{13} & a_{14} \\ a_{21} & a_{22} & a_{23} & a_{24} \\ a_{31} & a_{32} & a_{33} & a_{34} \\ a_{41} & a_{42} & a_{43} & a_{44} \end{vmatrix} \tag{3.45}$$

$$a_{11} = \lambda_1' + \frac{\lambda_1'\bar{\tau}_1^s\xi}{2} \tag{3.46}$$

$$a_{12} = 1 + \bar{\tau}_1^s\xi \tag{3.47}$$

$$a_{13} = -\lambda_1' + \frac{\lambda_1'\bar{\tau}_1^s\xi}{2} \tag{3.48}$$

$$a_{14} = 1 - \bar{\tau}_1^s\xi \tag{3.49}$$

$$a_{21} = \lambda_1' + \frac{\lambda_1'\bar{\kappa}_1^s\xi}{2} \tag{3.50}$$

$$a_{22} = 1 - \lambda_1' - \frac{\lambda_1'\bar{\kappa}_1^s\xi}{2} \tag{3.51}$$

$$a_{23} = \lambda_1' - \frac{\lambda_1'\bar{\kappa}_1^s\xi}{2} \tag{3.52}$$

$$a_{24} = -1 + \lambda_1' - \frac{\lambda_1' \bar{\kappa}_1^s \xi}{2} \tag{3.53}$$

$$a_{31} = \frac{\lambda_1' e^{-2\bar{h}\xi}}{2}\left(\bar{\tau}_2^s \xi - 2\bar{\mu}_2 + 2\right) \tag{3.54}$$

$$a_{32} = \frac{e^{-2\bar{h}\xi}}{2}\left(\left(2 + \lambda_1' \bar{h}\xi\right)\left(\bar{\tau}_2^s \xi - 2\bar{\mu}_2\right) + \left(2 + 2\lambda_1' \bar{h}\xi\right)\right) + \bar{\mu}_2{}^2 e^{-2\bar{h}\xi} \frac{\lambda_1' + 2}{\lambda_2' + 2\bar{\mu}_2} \tag{3.55}$$

$$a_{33} = -\lambda_1' - \frac{\lambda_1' \lambda_2' \bar{\mu}_2}{\lambda_2' + 2\bar{\mu}_2} + \frac{\lambda_1' \bar{\tau}_2^s \xi}{2} \tag{3.56}$$

$$a_{34} = -\bar{\tau}_2^s \xi\left(1 - \frac{\lambda_1' \bar{h}\xi}{2}\right) + \bar{\mu}_2\left(2 - \lambda_1' \bar{h}\xi\right) + \left(1 - \lambda_1' \bar{h}\xi\right) + \bar{\mu}_2{}^2\left(\frac{\lambda_1' + 2\lambda_1' \bar{h}\xi - 2}{\lambda_2' + 2\bar{\mu}_2}\right) \tag{3.57}$$

$$a_{41} = \frac{\lambda_1' e^{-2\bar{h}\xi}}{2}\left(\bar{\kappa}_2^s \xi - 2\bar{\mu}_2 + 2\right) \tag{3.58}$$

$$a_{42} = \frac{e^{-2\bar{h}\xi}}{2}\left(\lambda_1'\left(\bar{h}\xi - 1\right)\left(2 - 2\bar{\mu}_2 + \bar{\kappa}_2^s \xi\right) + 2\right) - \bar{\mu}_2{}^2 e^{-2\bar{h}\xi} \frac{\lambda_1' + 2}{\lambda_2' + 2\bar{\mu}_2} \tag{3.59}$$

$$a_{43} = \lambda_1' - \frac{\lambda_1' \bar{\kappa}_2^s \xi}{2} + \frac{\lambda_1' \lambda_2' \bar{\mu}_2}{\lambda_2' + 2\bar{\mu}_2} \tag{3.60}$$

$$a_{44} = \left(1 + \bar{h}\xi\right)\left(\lambda_1' + \lambda_1' \bar{\mu}_2 - \frac{\lambda_1' \bar{\kappa}_2^s \xi}{2}\right) - 1 - \bar{\mu}_2{}^2\left(\frac{\lambda_1' + 2\lambda_1' \bar{h}\xi - 2}{\lambda_2' + 2\bar{\mu}_2}\right) \tag{3.61}$$

$$b_{11} = \frac{\lambda_1' \bar{\mu}_2}{\lambda_2'} \tag{3.62}$$

$$b_{12} = -\frac{2\bar{\mu}_2\left(\bar{h}\xi - 1\right)\left(\lambda_2' - \lambda_1' \bar{\mu}_2\right)}{\lambda_2'\left(\lambda_2' + 2\bar{\mu}_2\right)} \tag{3.63}$$

$$b_{13} = -e^{2\bar{h}\xi} \frac{\lambda_1'\bar{\mu}_2\left(2\bar{\mu}_2 - \lambda_2' + 2\lambda_2'\bar{h}\xi\right)}{\lambda_2'\left(\lambda_2' + 2\bar{\mu}_2\right)} \tag{3.64}$$

$$b_{14} = -e^{2\bar{h}\xi} \frac{2\bar{\mu}_2\left(\lambda_2' + \lambda_1'\bar{\mu}_2 - \lambda_2'\bar{h}\xi + \lambda_1'\lambda_2'\left(\bar{h}\xi\right)^2 + \lambda_1'\bar{\mu}_2\bar{h}\xi\right)}{\lambda_2'\left(\lambda_2' + 2\bar{\mu}_2\right)} \tag{3.65}$$

$$b_{21} = 0 \tag{3.66}$$

$$b_{22} = \bar{\mu}_2 \frac{\lambda_1' + 2}{\lambda_2' + 2\bar{\mu}_2} \tag{3.67}$$

$$b_{23} = e^{2\bar{h}\xi} \frac{2\lambda_1'\bar{\mu}_2}{\lambda_2' + 2\bar{\mu}_2} \tag{3.68}$$

$$b_{24} = \bar{\mu}_2 e^{2\bar{h}\xi} \frac{\lambda_1' + 2\lambda_1'\bar{h}\xi - 2}{\lambda_2' + 2\bar{\mu}_2} \tag{3.69}$$

Substitution of the arbitrary functions *A* to *F* into Eqs. (3.18) to (3.23) yields the displacement and stress fields at an arbitrary point of the layered elastic half-space under axisymmetric surface loading as shown in Figure 3.1.

3.4 Numerical Results and Discussion

The complete solutions of displacements and stresses corresponding to the boundary value problems of a layered elastic medium under axisymmetric surface loading shown in Figure 3.1 are given by Eqs. (3.18) to (3.23) with the arbitrary functions *A* to *F* given by Eqs. (3.38) to (3.44). Given the complexity of the arbitrary functions *A* to *F*, closed-form solutions to the displacement and stress fields cannot be obtained. Therefore it is essential to determine all elastic fields by numerically evaluating the semi-infinite integrals appearing in Eqs. (3.18) to (3.23). It is found that those semi-infinite integrals with respect to ξ can be accurately evaluated by employing an adaptive numerical quadrature scheme. This scheme subdivides the interval of

integration and employs a 21-point Gauss–Kronrod rule (Piessens, 1983) to estimate the integral over each subinterval. The error for each subinterval is estimated by comparing the obtained results with those from a 10-point Gauss-Kronrod rule. The subdivision continues until the error from the approximation is reached a specified tolerance.

The accuracy of the present solution is first verified by comparing with the existing solution given by Gerrard (1969), who presented the classical solutions (without the influence of surface energy effects) of a layered elastic half-space subjected to axisymmetric surface loading. Table 3.1 presents a comparison of normalized displacements at the surface ($z = 0$) and normalized stresses at the interface ($z = h$) along the radial direction of a layered elastic half-space under uniformly distributed normal traction p_0, acting over a circular area of radius a at the surface. The comparison of surface displacements and stresses at the interface of the layered half-space under linearly distributed shear traction $\bar{q}(\bar{r}) = -q_0 r/\mu_1 a$ applied over a circular area of radius a at the surface is also presented in Table 3.2. In addition, $\mu_1/\mu_2 = 5$ with Poisson's ratio $\nu_1 = \nu_2 = 0.2$, and $h/a = 1$ are considered for the numerical results given in both tables. The solutions for normalized displacements and stresses from the present study are obtained by setting the parameters associated with the surface energy effects to be zero, i.e., $\tau^s \cong 0$ and $\kappa^s \cong 0$. It is evident that excellent agreement between the two solutions is observed for both displacements and stresses shown in Tables 3.1 and 3.2.

Numerical results for vertical and radial displacements, and vertical and shear stresses corresponding to a layered elastic half-space with the influence of surface energy effects subjected to axisymmetric surface loading as shown in Figure 3.1 are presented next. Two cases of axisymmetric surface loading, namely, the *vertical* loading and the *radial* loading are considered in the numerical study. The *vertical* loading denotes the case where uniformly distributed normal traction p_0 applied over a circular area of normalized radius $a/\Lambda_1 = \bar{a} = 10$. The *radial* loading represents the case where the layered half-space is subjected to linearly distributed tangential traction $\bar{q}(\bar{r}) = q_0\bar{r}/\mu_1\bar{a}$ over a circular area of normalized radius $\bar{a} = 10$, where q_0 is the maximum traction at the edge of the loading region. The functions defined as shown in

Eqs. (3.36) and (3.37) are given respectively for the *vertical* loading and the *radial* loading as follows,

$$\bar{P}(\xi) = \frac{p_0 \bar{a}}{\xi} J_1(\xi \bar{a}) \text{ and } \bar{Q} = 0 \tag{3.70}$$

$$\bar{P} = 0 \text{ and } \bar{Q}(\xi) = \frac{2q_0}{\xi^2} J_1(\xi \bar{a}) - \frac{q_0 \bar{a}}{\xi} J_0(\xi \bar{a}) \tag{3.71}$$

In addition, the numerical results presented hereafter correspond to the case where the material for the upper layer (the domain '1') is Si [100] whereas Al [111] is chosen for the underlying half-space (the domain '2') respectively. The material properties for both domains are given in Table 3.3 (Miller and Shenoy, 2000).

Figures 3.2 presents radial variations of non-dimensional displacements at the top surface (z = 0) and non-dimensional stresses at the interface (z = h) of a layered elastic half-space under the vertical loading for different values of normalized thickness of the top layer (h/a). Note that the stress profiles in all figures presented in this section are computed at the interface (z = h) at the bulk material of the underlying half-space. Figure 3.2(a) shows radial profiles of vertical and radial surface displacements for various values of h/a whereas the profiles of normal and shear stresses at the interface are illustrated in Figure 3.2(b). The classical solutions also presented in these figures for comparison are obtained by setting the parameters associated with the surface energy effects to be zero, i.e., $\tau^s \cong 0$ and $\kappa^s \cong 0$. It is evident from Figure 3.2 that although the results from the present study and the classical solution display similar trends for both displacements and stresses at all values of h/a, the surface energy effects renders the layered medium stiffer. The present solution yields lower surface displacements and stresses at the interface. The influence of surface energy is however less significant in the interface stresses, especially in the case of the shear stress. It is also found that the magnitude of all displacements and stresses decrease with increasing the normalized thickness of the layer (h/a) since the upper layer is stiffer than the underlying half-space (Lamé constants of Si [100] are higher than those of Al [111]). In addition, as the layer thickness increases both vertical and radial surface

displacements move towards the homogeneous half-space solutions presented by Intarit (2012), and both solutions are virtually identical when $h/a \geq 100$.

Radial profiles of normalized surface displacements ($z = 0$) and normalized stress at the interface ($z = h$) of the layered elastic medium under the vertical loading are shown in Figure 3.3 to demonstrate the influence of the residual surface stress (τ^s) on elastic fields. The values of the residual surface stress in the underlying half-space are varied (i.e. τ_2^s = 0.1, 1, 5, 10 N/m) whereas other material parameters associated with both upper layer and underlying half-space given in Table 3.3 remain unchanged. In addition, the normalized thickness of $h/a = 1$ is considered in the numerical results shown in this figure. Once again, the influence of the surface stress is clearly observed from the displacement and stress solutions presented in Figure 3.3. The values of all displacements and stresses from the present study are substantially reduced from their classical elasticity counterparts as the value of the residual surface stress increases.

The next numerical results are presented to demonstrate the size-dependent behavior of the present solution when the influence of surface energy effects is considered. Figure 3.4 shows radial variations of vertical and radial surface displacements, and the vertical and shear stresses at the interface of the layered half-space under the vertical loading for different values of the normalized radius of loading area $\overline{a}$ (i.e. $\overline{a} = a/\Lambda_1 = 1, 5, 10$). In addition, the thickness of the top layer and the circular loading area are varied while their ratio is maintained at $h/a = 1$. Note that the solution when $\overline{a} = 1$ corresponds to the case where the thickness of the layer is equal to the characteristic length (Λ_1). The corresponding non-dimensional solution for the classical elasticity case is also shown, and it is size-independent. The size-dependency of the present solution is clearly observed in all displacement and stress profiles. It is evident from the numerical results presented in Figure 3.4 that the present solution accounting for surface energy effects approaches the classical solution as the loading radius increases. This is consistent with the fact that a larger loading area would produce higher displacements and stresses.

The final set of the numerical results corresponds to the case where the layered elastic half-space is subjected to the radial loading, in which the tangential traction is applied linearly distributed over a circular area of normalized radius $\overline{a} = 10$. Figure

3.5 presents radial profiles of non-dimensional displacements at the top surface ($z = 0$) and non-dimensional stresses at the interface ($z = h$) for different values of h/a. It is evident from Figure 3.5 that both displacements and stresses of the layered half-space under radial loading depend more significantly on surface energy effects for all values of h/a when compared to the results presented in Figure 3.2 under the vertical loading case. The presence of surface stresses significantly lowers the magnitude of all displacements and stresses shown in Figure 3.5. In addition, all displacements and stresses are reduced as the normalized thickness of the layer (h/a) increases. Once again, both vertical and radial surface displacements are practically the same as the half-space solutions given by Intarit (2012) when $h/a \geq 100$ similar to what observed in the vertical loading case.

3.5 Conclusion

An analytical treatment of a layered elastic half-space under axisymmetric surface loading, taking into account the influence of surface energy effects is presented in this chapter. The boundary value problem corresponding to a layered elastic half-space subjected to axisymmetric normal and tangential traction is formulated based on the complete Gurtin-Murdoch theory of surface elasticity and the application of Hankel integral transforms. An efficient numerical quadrature scheme is developed to evaluate all involved integrals. Selected numerical results for radial profiles of displacements and stresses are presented to portray the influence of various parameters on elastic fields. The numerical results indicate that the surface energy effects play an important role in both stress and displacement fields of a layered elastic medium. Surface residual stress reduces the surface displacements and stresses at the interface of the layered medium. Unlike the classical elasticity solution, the present study shows substantial size-dependency of elastic fields. Both displacement and stress fields show strong dependency on the loading area, and the magnitude of non-dimensional displacements and stresses increase with increasing the radius of the loading area. The application of the present fundamental solution for nano-indentation and contact problems will be presented in next chapter. In addition, the present solution can also be used as a benchmark solution for assessing the accuracy of numerical models such as the finite

element and boundary element methods, which can be used to investigate more complicated problems in the presence of surface energy effects.

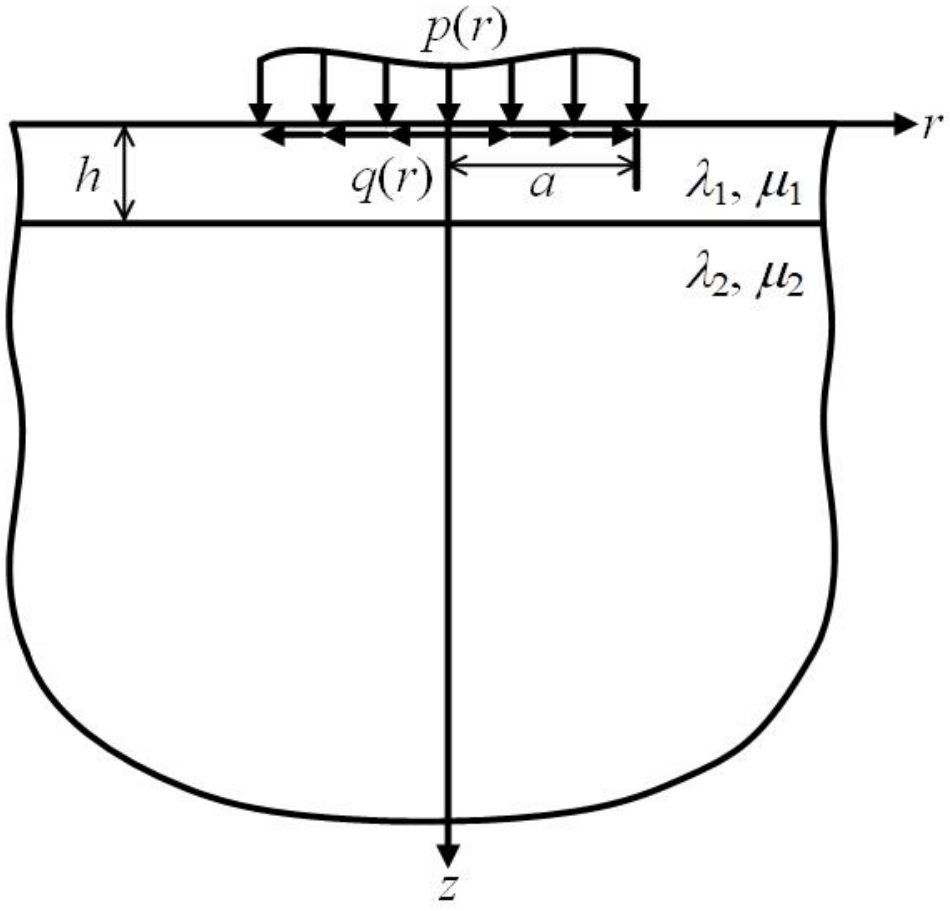

Figure 3.1 Layered elastic half-space subjected to axisymmetric surface loading.

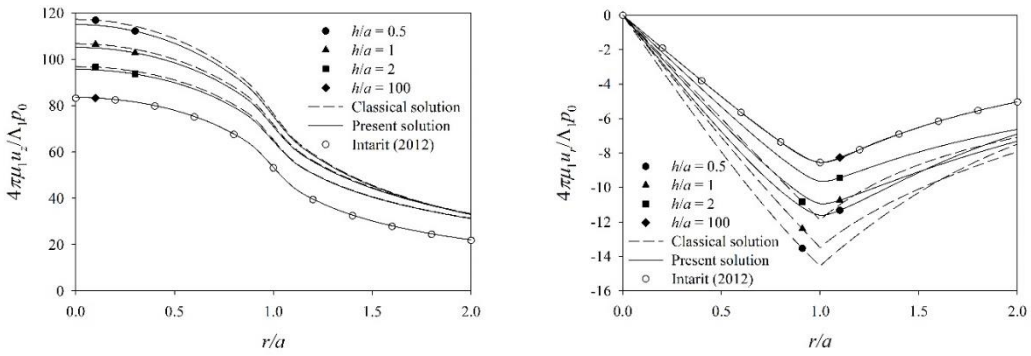

(a)

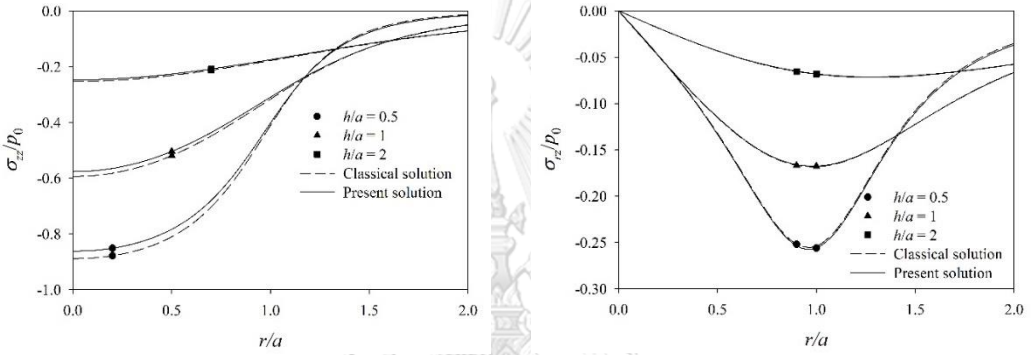

(b)

Figure 3.2 Radial variations of elastic fields under the vertical loading for different values of layer thickness (h/a): (a) surface displacements ($z = 0$) and (b) stresses at the interface ($z = h$).

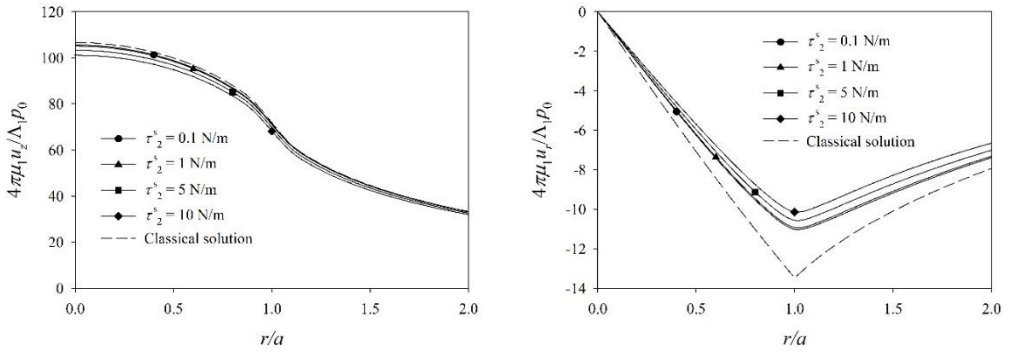

(a)

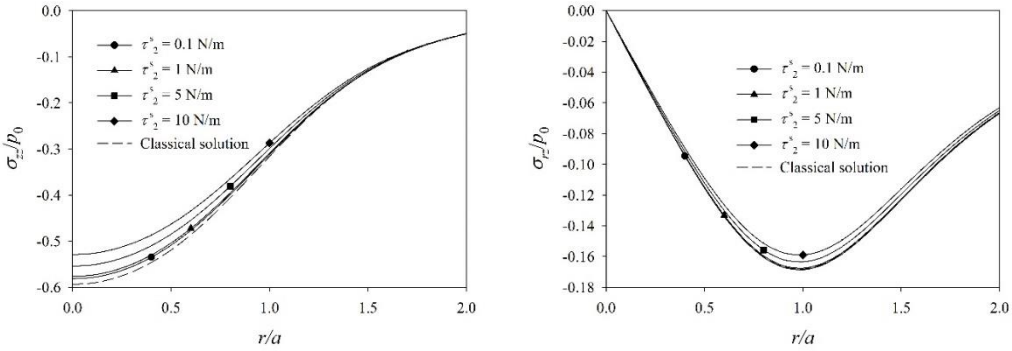

(b)

Figure 3.3 Radial variations of elastic fields under the vertical loading for h/a = 1 and different magnitudes of residual surface stress (τ^s_2): (a) surface displacements (z = 0) and (b) stresses at the interface ($z = h$).

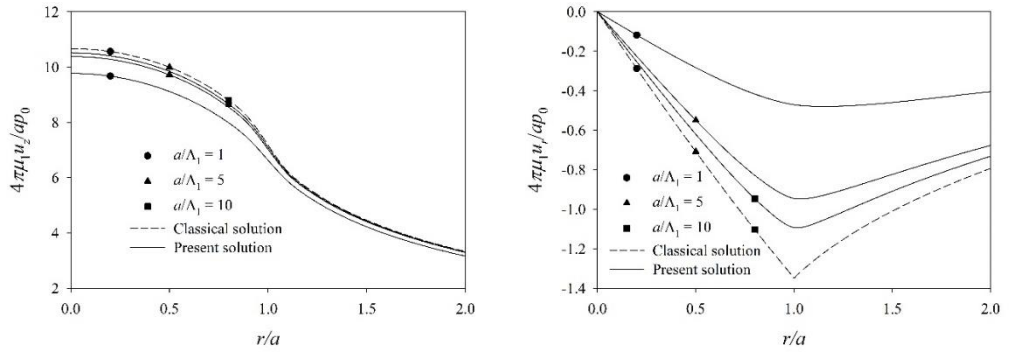

(a)

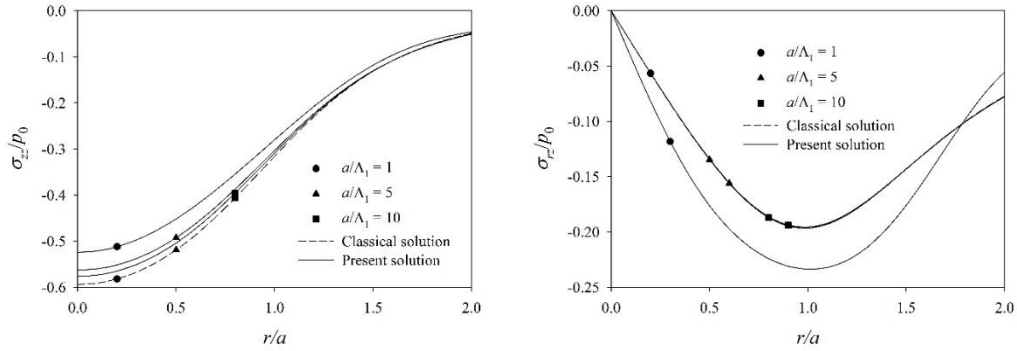

(b)

Figure 3.4 Radial variations of elastic fields under the vertical loading for $h/a = 1$ and different values of loading radius ($\bar{a}$): (a) surface displacements ($z = 0$) and (b) stresses at the interface ($z = h$).

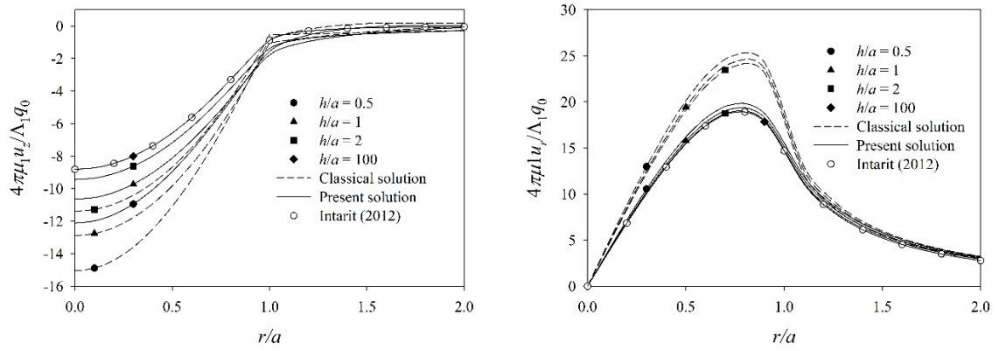

(a)

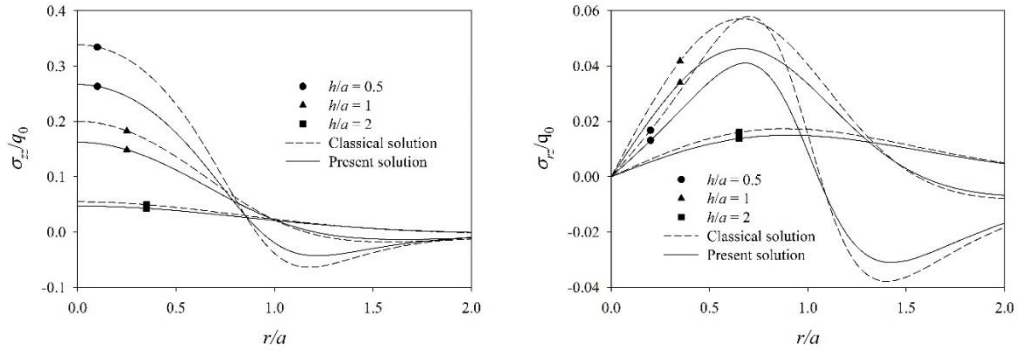

(b)

Figure 3.5 Radial variations of elastic fields under the radial loading for different values of layer thickness (*h/a*): (a) surface displacements ($z = 0$) and (b) stresses at the interface ($z = h$).

Table 3.1 Comparison of normalized surface displacements and stresses at the interface of a layered elastic half-space under uniformly distributed normal traction for $\mu_1/\mu_2 = 5$ and $h/a = 1$.

r/a	$\mu_1 u_z/ap_0$		$\mu_1 u_r/ap_0$		σ_{zz}/p_0		σ_{rz}/p_0	
	Gerrard (1969)	Present solution	Gerrard (1969)	Present solution	Gerrard (1969)	Present solution	Gerrard (1969)	Present solution
0.0	0.9945	0.9944	0.0000	0.0000	0.4260	0.4260	0.0000	0.0000
0.5	0.9442	0.9440	-0.0746	-0.0746	0.3790	0.3790	0.0867	0.0867
1.0	0.7651	0.7649	-0.1363	-0.1363	0.2526	0.2526	0.1303	0.1303
2.0	0.4630	0.4629	-0.1048	-0.1048	0.0657	0.0657	0.0719	0.0719
3.0	0.3179	0.3177	-0.0747	-0.0748	0.0174	0.0174	0.0307	0.0307
5.0	0.1867	0.1866	-0.0420	-0.0421	0.0010	0.0010	0.0069	0.0069
10.0	0.0933	0.0932	-0.0217	-0.0218	0.0001	0.0000	0.0009	0.0009

Table 3.2 Comparison of normalized surface displacements and stresses at the interfaces of a layered elastic half-space under linearly distributed tangential traction for $\mu_1/\mu_2 = 5$ and $h/a = 1$.

r/a	$\mu_1 u_z/aq_0$		$\mu_1 u_r/aq_0$		σ_{zz}/q_0		σ_{rz}/q_0	
	Gerrard (1969)	Present solution	Gerrard (1969)	Present solution	Gerrard (1969)	Present solution	Gerrard (1969)	Present solution
0.0	0.1188	0.1189	0.0000	0.0000	0.1150	0.1150	0.0000	0.0000
0.5	0.0941	0.0941	-0.0952	-0.0952	0.0803	0.0803	0.0359	0.0359
1.0	0.0253	0.0253	-0.0934	-0.0934	0.0173	0.0173	0.0312	0.0312
2.0	0.0044	0.0044	-0.0198	-0.0198	-0.0068	-0.0068	-0.0005	-0.0005
3.0	-0.0003	-0.0003	-0.0087	-0.0087	-0.0028	-0.0028	-0.0020	-0.0020
4.0	-0.0006	-0.0005	-0.0051	-0.0051	-0.0010	-0.0010	-0.0012	-0.0012
5.0	-0.0003	-0.0003	-0.0036	-0.0036	-0.0004	-0.0004	-0.0007	-0.0007
10.0	0.0001	0.0001	-0.0014	-0.0014	0.0000	0.0000	-0.0001	-0.0001

Table 3.3 Material properties employed in numerical study.

Material parameters	**Upper layer**	**Underlying half-space**
λ (N/m^2)	78.0849×10^9	58.17×10^9
μ (N/m^2)	40.2256×10^9	26.13×10^9
τ^s (N/m)	0.6056	1
λ^s (N/m)	4.4939	6.8511
μ^s (N/m)	2.7779	-0.376
κ^s (N/m)	10.0497	6.0991

CHAPTER IV
NANOINDENTATION ON LAYERED ELASTIC MEDIUM

4.1 General

This chapter presents the analysis of axisymmetric rigid indentation on a layered elastic half-space with consideration of surface energy effects under frictionless and adhesive contacts by adopting a complete Gurtin-Murdoch continuum model for theory of surface elasticity. The fundamental solutions of a layered elastic medium with consideration of surface stresses derived in Chapter III are employed in the formulation of axisymmetric indentation problem as a mixed-boundary value problem. The displacement boundary condition is expressed in terms of a displacement Green's function, which is obtained by employing the Hankel integral transforms. The unknow contact pressure distribution under an indenter of axisymmetric profiles is determined by using a discretization technique. The accuracy of the proposed solution scheme is verified by comparing with existing solutions. Selected numerical results are presented to portray the influence of surface stresses on a layered elastic half-space under indentation with frictionless and adhesive contacts.

4.2 Nanoindentation with Frictionless Contact

Consider a layered elastic medium subjected to axisymmetric indentation under the action of a vertical force P as shown in Figure 4.1. The frictionless contact between the indenter and the layered medium is assumed in this study. In addition, the punch profile is given by $\delta(r)$ where the final radius of a contact region and the indentation depth at the center of the punch are denoted by a and d respectively. The punch profile is assumed to be *smooth* (i.e., $d\delta/dr$ is well-defined) at any point within the contact region except along the boundary $r = a$ where the profile can be *non-smooth*. A punch with a well-defined $d\delta/dr$ for $r \leq a$ is termed *smooth-contact* indentation [e.g., a paraboloid indenter in Figure 4.1 (a)] whereas for *non-smooth-contact* indentation, $d\delta/dr$ is not well-defined at $r = a$ [e.g., a flat-ended indenter in Figure 4.1 (b)].

For axisymmetric frictionless indentation, the top surface of the upper layer can be decomposed into the surface outside the contact region ($r > a$) on which the traction (both normal and shear) is identically zero, and the surface inside the contact region ($r \le a$) on which the normal displacement is prescribed in terms of the indentation depth d and the punch profile $\delta(r)$. In addition, the shear traction vanishes on the contact area due to the condition of frictionless contact surface. To solve this indentation problem, the subscript "1" is employed to represent the quantities corresponding to the bulk of the upper layer and the surface. In addition, the subscript "2" is used to represent the quantities associated with the bulk of the half-space and the interface between the layer and the half-space. The mixed boundary conditions at the top surface can then be expressed as,

$$u_{z1}\big|_{z=0} = d - \delta(r); \qquad 0 \le r \le a \tag{4.1}$$

$$\sigma_{zz1}\big|_{z=0} + \tau_1^s \left(\frac{d^2 u_{z1}}{dr^2} + \frac{1}{r}\frac{du_{z1}}{dr} \right)_{z=0} = 0; \quad a < r < \infty \tag{4.2}$$

$$\sigma_{rz1}\big|_{z=0} + \kappa_1^s \left(\frac{d^2 u_{r1}}{dr^2} + \frac{1}{r}\frac{du_{r1}}{dr} - \frac{u_{r1}}{r^2} \right)_{z=0} = 0 \tag{4.3}$$

In addition, the continuity conditions at the interface are given by Eqs. (3.26) to (3.29).

By using the method of superposition, the vertical displacement at the contact surface, Eq. (4.1), can be expressed as an integral equation in the following form:

$$\int_0^a U_z^N(r, r') \cdot p(r')\, dr' = d - \delta(r); \qquad 0 \le r \le a \tag{4.4}$$

where $p(r')$ denotes the normal contact traction occurred inside the contact region; and $U_z^N(r, r')$ denotes the Green's function corresponding to the vertical displacement at any distance r on the contact area due to a unit vertical ring load applied on the top surface of the layered medium at the radius r'. The Green's function can be expressed in the form of Hankel integral transform as,

$$U_z^N(r,r') = -(\bar{\lambda}_1+1)\Lambda_1\int_0^\infty \xi^2\left\{A\xi + B\left(\frac{2}{\bar{\lambda}_1+1}\right) + C\xi - D\left(\frac{2}{\bar{\lambda}_1+1}\right)\right\}J_0(\xi\bar{r})\,d\xi \qquad (4.5)$$

where $\bar{\lambda}_1 = \lambda_1/\mu_1$; $\bar{r} = r/\Lambda_1$; and $\Lambda_1 = \kappa_1^s(\lambda_1+2\mu_1)/2\mu_1(\lambda_1+\mu_1)$. In addition, *A*, *B*, *C*, and *D* are the arbitrary functions, which can be obtained explicitly from Chapter III with the loading functions $\bar{P}(\xi)$ and $\bar{Q}(\xi)$ defined respectively as,

$$\bar{P}(\xi) = \bar{r}'J_0(\xi\bar{r}') \text{ and } \bar{r}' = r'/\Lambda_1 \qquad (4.6)$$

$$\bar{Q}(\xi) = 0 \qquad (4.7)$$

In order to obtain the unknown normal contact traction $p(r')$, the contact surface under the indenter is discretized into a number of *Ne* annular ring elements. It is assumed that the normal contact traction is constant within each ring element. The vertical displacements at the contact surface, Eq. (4.4), can then be expressed as,

$$\sum_{j=1}^{Ne} U_z^N(r_i,r_j)\cdot p(r_j) = d - \delta(r_i); \qquad 0 \le r \le a \qquad (4.8)$$

where $U_z^N(r_i,r_j)$ (i, j = 1, 2,…, *Ne*) denotes the Green's function corresponding to the vertical displacement at the center of the i^{th} ring element due to vertical loading of unit intensity applied uniformly over the j^{th} ring element. The expression of the Green's function under the vertical annular loading is also given by Eq. (4.5) with the arbitrary functions *A* to *D* being given in Chapter III together with the following loading functions for $\bar{P}(\xi)$ and $\bar{Q}(\xi)$

$$\bar{P}(\xi) = \frac{\bar{r}_0 J_1(\xi\bar{r}_0)}{\xi} - \frac{\bar{r}_i J_1(\xi\bar{r}_i)}{\xi} \qquad (4.9)$$

$$\bar{Q}(\xi) = 0 \qquad (4.10)$$

where $\bar{r}_i = r_i/\Lambda_1$ and $\bar{r}_0 = r_0/\Lambda_1$ are inner and outer radii of the annular loading.

Once the normal traction distribution in the contact region $p(r')$ is obtained, all elastic fields within the bulk of the layered half-space under axisymmetric indentation as shown in Figure 4.1 can be determined from the following equation:

$$R(r,z) = \int_0^\infty R^N(r,z;r') \cdot p(r') dr' \tag{4.11}$$

where $R(r,z)$ denotes displacements and stresses at any point (r, z) in a layered elastic half-space under axisymmetric indentation on the top surface; and $R^N(r,z;r')$ denotes the Green's functions corresponding to displacements and stresses at any point (r, z) due to the vertical loading (ring or annular) acting on the top surface of the layered medium at the radius r'. The Green's functions, $R^N(r,z;r')$, expressed in the form of the Hankel integral transforms, are presented in Chapter III.

A computer program based on the solution procedure described in the previous section has been developed to study axisymmetric rigid frictionless indentation on a layered elastic half-space as shown in Figure 4.1. In this study, indenters with flat-ended cylindrical and paraboloidal punch profiles are investigated for *non-smooth* and *smooth* contacts respectively. For flat-ended cylindrical punch [see Figure 4.1 (b)], the contact radius a and a normal indentation depth d are defined with the punch profile being $\delta(r) = 0$. For paraboloidal punch, the punch profile is given by $\delta(r) = \alpha r^2$ where α is a constant and the radius of contact region a is unknown a priori [see Figure 4.1 (a)]. The unknown contact traction between a rigid indenter and the layered medium can be determined by employing discretization approach outlined in the preceding section. The required Green's function is obtained from a layered elastic half-space under the vertical annular loading of unit intensity. It is noted that Green's functions are expressed as semi-infinite integrals with respect to ξ [see Eq. (4.5)], which can be accurately evaluated by employing the adaptive numerical quadrature scheme discussed in Chapter III.

The accuracy of the numerical solutions obtained from the present scheme is validated with existing solutions. First, the present solution is specialized for the case of flat-ended cylindrical punch of radius a on a layered elastic half-space without the

influence of surface energy effects. Figure 4.2 (a) shows a comparison of normalized contact pressure profiles along the radial direction under the flat-ended cylindrical indenter between the present solution and the solution by Chen and Engel (1972) for different numbers of annular elements, *Ne*, used to discretize the contact area. The material parameters employed in the comparison are $\nu_1 = 0.333$ and $\nu_2 = 0.250$ with $\mu_1/\mu_2 = 0.25$, and the ratio of layer thickness to punch radius is $h/a = 3$. In addition, the surface parameters are set to be negligibly small ($\tau^s = \kappa^s \approx 0$). It is found that converged numerical solution is obtained when $Ne \geq 20$, and it agrees very closely with the solution by Chen and Engel (1972).

Figure 4.2 (b) shows the comparison between the present numerical solutions and the solutions given by Pinyochotiwong et al. (2013) for axisymmetric indentation on a homogeneous elastic half-space with the influence of surface energy effects. The following material parameters are employed in the present solution: $\lambda_1 = \lambda_2 = 58.17$ GPa; $\mu_1 = \mu_2 = 26.13$ GPa; $\tau_1^s = 1$ N/m; and $\kappa_1^s = 6.0991$ N/m. In addition, $\tau_2^s = \kappa_2^s \approx 0$. Comparison of normalized contact pressure profiles under flat-ended cylindrical and paraboloidal indenters are shown in Figures 4.2 (b) for discretization method. It should be noted that under flat-ended cylindrical punch a vertical ring load has to be applied at $r = a$ in the present solution to account for a normal ring load induced at the indenter edge due to the presence of the residual surface stress. The applied vertical force *P* would then be supported by the ring load together with the contact pressure generated under the indenter. A convergence study indicates that a very good agreement between the present solution and the benchmark solution (Pinyochotiwong et al., 2013) is obtained with $Ne = 30$ for flat-ended cylindrical and paraboloidal indenters as shown in Figures 4.2 (b). The accuracy of the proposed solution scheme is thus verified through these comparisons.

The influence of surface energy effects on axisymmetric frictionless indentation on a layered elastic half-space is investigated next for flat-ended cylindrical and paraboloidal indenters respectively. For convenience, the following non-dimensional quantities are employed: $\bar{z} = z/\Lambda_1$; $\bar{h} = h/\Lambda_1$; $\bar{a} = a/\Lambda_1$; $\bar{d} = d/\Lambda_1$; and $\bar{\delta} = \delta/\Lambda_1$. The discretization technique is employed with $Ne = 30$ for the numerical results presented

hereafter. For the layered elastic medium considered in the numerical study, the properties of the bulk and the surface of the top layer are identical to those of the half-space employed by Pinyochotiwong et al. (2013) whereas λ_2 = 78.08 GPa, μ_2 = 40.23 GPa for the underlying half-space. In addition, τ_2^s = 0.3944 N/m, and κ_2^s = -3.9506 N/m at the interface. Note that the broken lines in all figures presented in this section denote the classical solutions where surface stress effects are ignored (i.e. $\tau^s = \kappa^s \approx 0$).

The influence of the residual surface stress (τ^s) on the normalized contact pressure and surface displacement are shown respectively in Figures 4.3 (a) and 4.3 (b) with h/a = 1 and $\bar{a}$ = 1. In addition, the value of τ_1^s is varied whereas the value of τ_2^s and other material parameters remain unchanged, and the following ratios of τ_1^s/τ_2^s are considered, i.e. τ_1^s/τ_2^s = 0.5, 1, 2 and 4. Note that the conditions of h/a = 1 and $\bar{a}$ = 1 correspond to the case where the layer thickness is equal to the characteristic length (Λ_1). Numerical results in Figure 4.4 indicate that both contact pressure and surface displacement from the present study and the classical elasticity display similar trends for all values of τ_1^s/τ_2^s. It can be seen from Figure 4.3 (a) that the normalized contact pressure from the present study is lower than its classical counterpart due to the presence of surface stresses, and it decreases with increasing the ratio of τ_1^s/τ_2^s. This is due to the fact that a larger ring load is generated for higher value of residual surface stress at the top surface resulting in smaller contact pressure being developed under the indenter. In addition, the singularity is observed at the profiles near the indenter edge for both present and classical solutions. Figure 4.3 (b) reveals that the vertical displacements outside the contact area obtained from the present study are higher than the classical solution since higher indentation force is required due to the presence of surface stresses to produce the same indentation depth.

Figures 4.4 (a) and 4.4 (b) respectively display radial variations of normalized vertical displacements and vertical stresses of a layered elastic half-space under axisymmetric indentation at different depths for the contact radius of $\bar{a}$ = 1.0 and h/a = 1. It is evident that the surface stresses have a significant influence on both displacements and stresses in the layered medium. The vertical displacements from the present study are higher than their classical counterparts in both layer and half-space as

shown in Figure 4.4 (a). Numerical results presented in Figure 4.4 (b) display lower vertical stresses from the present study on the area under the contact region ($r/a < 1.0$) in the top layer ($z/\Lambda_1 < 1.0$) whereas, in the half-space ($z/\Lambda_1 > 1.0$), minor difference between the vertical stresses from the present and classical solutions is observed.

The indentation forces on a layered elastic half-space with the consideration of surface energy effects are also investigated. Figure 4.5 (a) presents variations of normalized indentation force with the normalized contact radius, $\bar{a}$, for different values of normalized layer thickness h/a. The dash lines in the figure indicate the corresponding classical elasticity solutions (i.e. $\tau^s = \kappa^s \cong 0$), and they are size-independent. In addition, P_c denotes the indentation force on an elastic half-space ($h/a \to \infty$) for the classical elasticity. It is clearly seen from Figure 4.5 (a) that under the influence of surface energy effects the normalized indentation force depends significantly on the contact radius indicating a size-dependent behavior. The indentation force increases with decreasing the layer thickness, which is physically realistic since the upper layer is softer than the underlying half-space, the reduction in thickness then renders the layered medium stiffer. In addition, the indentation force decreases with increasing the contact radius, and it converges to the classical solution.

To study the influence of shear moduli in the layered medium, variations of normalized indentation force with the ratio μ_1/μ_2 for different values of h/a are shown in Figure 4.5 (b). It is evident from Figure 4.5 (b) that the present solution and the classical solution display similar behavior where the indentation forces decrease with increasing the ratio of μ_1/μ_2 for all values of layer thickness. This behavior was also noted by Dhaliwal (1970), who studied axisymmetric rigid indentation on an elastic layer overlying an elastic half-space. In addition, the indentation force from the present study is higher than its classical counterpart confirming the fact that the influence of surface energy effects renders the layered medium stiffer.

The second set of numerical results corresponding to rigid frictionless indentation under a paraboloidal indenter with the normalized profile of $\bar{\delta}(\bar{r}) = 0.5\bar{r}^2$ is reported in Figures 4.6 - 4.8. This case is a *smooth* contact punch where the contact radius a is unknown a *priori*. Note that the contact radius is obtained by imposing the

continuity of vertical stress on the top surface at $r = a$. In addition, the normal ring load is not induced along the indenter edge under *smooth* contact indentation. Radial profiles of normalized contact pressure and normalized surface displacement under paraboloidal indentation are illustrated in Figure 4.6 for τ_1^s/τ_2^s = 0.5, 1, 2, and 4 by varying the value of τ_1^s with the values of τ_2^s and other material parameters being unchanged. In addition, $h/a = 1$ and $\bar{a} = 1$ are employed for the numerical results shown in Figure 4.6. It is evident that the surface stresses have a significant influence on normalized contact pressure and surface displacement under paraboloidal indentation. The normalized contact pressure profiles presented in Figure 4.6 (a) show no singularity at the edge of a *smooth* contact indenter. The contact pressure from the classical solution vanishes at the indenter edge whereas, in the present solution, non-zero contact pressure is observed at $r = a$ due to the existence of surface stresses. In addition, numerical results presented in Figure 4.6 reveal that both contact pressure and displacement in the present study increase with increasing the values of τ_1^s/τ_2^s, and they are higher than the classical solutions since the surface stresses render the layered medium stiffer, and larger indentation force is then required for the same indentation depth.

Figures 4.7 illustrates radial profiles of normalized vertical displacements and vertical stresses in a layered elastic medium under paraboloidal indentation at various depths for $h/a = 1$ and $\bar{a} = 1$. Figure 4.7 reveals that the influence of surface stresses on elastic fields under paraboloidal indentation is similar to what observed under flat-ended cylindrical punch shown in Figure 4.4. The vertical displacements under the influence of surface stresses are larger than the corresponding classical solutions in both layer and half-space, and the presence of surface energy effects results in discrepancy in vertical stresses between the present and classical solutions, especially in the top layer.

Figures 4.8 (a) and 4.8 (b) respectively show variations of normalized indentation force on a layered elastic half-space with contact radius $\bar{a}$ and shear modulus ratio μ_1/μ_2 for different values of layer thickness h/a. Numerical results presented in Figure 4.8 indicate that the indentation force under paraboloidal punch displays similar dependence on the surface energy effects when compared to what observed in Figure 4.5 for *non-smooth* contact indentation. In Figure 4.8 (a), the

indentation force decreases with increasing the layer thickness and the contact radius, and it converges to the classical solution for increasing values of $\bar{a}$. The indentation forces from the present study and the classical elasticity decrease with increasing the ratio of μ_1/μ_2 for all thicknesses as shown in Figure 4.8 (b). It is also found that the indentation force under paraboloidal punch is independent of the ratio μ_1/μ_2 when $h/a \geq 10$. This implies that an analysis of a layered elastic half-space under the paraboloidal punch and the influence of surface energy effects can be performed as a rigid indentation on an elastic half-space with the properties identical to the top layer of the layered medium when the thickness of the top layer is at least ten times greater than the contact radius.

4.3 Nanoindentation with Adhesive Contact

The analysis of nanoindentation outlined in the previous section are carried out based on the assumption of frictionless contact surface. If the coefficient of friction between a rigid flat-ended cylindrical punch and a layered elastic half-space is large enough, the indenter is prevented from any sliding on the contact area. This condition is known as an adhesive contact. For axisymmetric adhesive indentation as shown in Figure 4.9, the surface of the upper layer can be decomposed into a surface outside the contact region ($r > a$) on which both normal and shear stresses are identically zero, and a surface inside the contact region ($r \leq a$) on which the normal displacement is prescribed in terms of the indentation depth d and the radial displacement is zero at every point of the contact region. The mixed boundary conditions at the top surface for the adhesive contact problem can then be expressed as

$$u_{z1}\big|_{z=0} = d; \qquad 0 \leq r \leq a \tag{4.12}$$

$$u_{r1}\big|_{z=0} = 0; \qquad 0 \leq r \leq a \tag{4.13}$$

$$\sigma_{zz1}\big|_{z=0} + \tau_1^s \left(\frac{d^2 u_{z1}}{dr^2} + \frac{1}{r}\frac{du_{z1}}{dr} \right)_{z=0} = 0; \; a < r < \infty \tag{4.14}$$

$$\sigma_{rz1}\big|_{z=0} + \kappa_1^s \left(\frac{d^2 u_{r1}}{dr^2} + \frac{1}{r}\frac{du_{r1}}{dr} - \frac{u_{r1}}{r^2} \right)_{z=0} = 0; \;\; a < r < \infty \tag{4.15}$$

In addition, the continuity conditions at the interface are given by Eqs. (3.26) to (3.29).

By using the method of superposition, the normal and radial surface displacements are given by Eqs. (4.12) and (4.13), can be expressed in the form of integral equations as,

$$\int_0^a U_z^N \left(r, r'\right) \cdot p\left(r'\right) dr' + \int_0^a U_z^R \left(r, r'\right) \cdot q\left(r'\right) dr' = d; \;\; 0 \le r \le a \tag{4.16}$$

$$\int_0^a U_r^N \left(r, r'\right) \cdot p\left(r'\right) dr' + \int_0^a U_r^R \left(r, r'\right) \cdot q\left(r'\right) dr' = 0; \;\; 0 \le r \le a \tag{4.17}$$

where $U_i^j \left(r, r'\right)$ denotes the Green's function corresponding to the normal ($i = z$) or radial ($i = r$) surface displacement at any distance r on the contact surface due to a unit normal ($j = N$) or a unit radial ($j = R$) ring load acting on the surface of the upper layer at the radius r'. The Green's functions corresponding to the normal and radial surface displacements of a layered elastic half-space with consideration of surface energy effects can be expressed in the form of Hankel integral transform as

$$U_z^k \left(r, r'\right) = -\left(\bar{\lambda}_1 + 1\right) \Lambda_1 \int_0^\infty \xi^2 \left\{ A\xi + B\left(\frac{2}{\bar{\lambda}_1 + 1} \right) + C\xi - D\left(\frac{2}{\bar{\lambda}_1 + 1} \right) \right\} J_0\left(\xi \bar{r}\right) d\xi \tag{4.18}$$

$$U_r^k \left(r, r'\right) = \left(\bar{\lambda}_1 + 1\right) \Lambda_1 \int_0^\infty \xi^2 \left\{ -A\xi + B + C\xi + D \right\} J_1\left(\xi \bar{r}\right) d\xi \tag{4.19}$$

where $\bar{\lambda}_1 = \lambda_1 / \mu_1$; $\bar{r} = r / \Lambda_1$; and $\Lambda_1 = \kappa_1^s \left(\lambda_1 + 2\mu_1\right) / 2\mu_1 \left(\lambda_1 + \mu_1\right)$. In addition, A, B, C and D are the arbitrary functions of the applied surface loads at any the radius r', which are given explicitly in Chapter III and the superscript "k" is used to denote a unit normal ring load ($k = N$) or a unit radial ring load ($k = R$) acting on the surface of the upper layer. Note that the loading function $\bar{P}\left(\xi\right)$ is defined in Eq. (4.6) whereas $\bar{Q}\left(\xi\right)$ is given by

$$\bar{Q}\left(\xi\right) = \bar{r}' J_1\left(\xi \bar{r}'\right) \tag{4.20}$$

For the analysis of the adhesive contact problem, the normal traction, $p(r)$, and the shear traction, $q(r)$, can be represented as discrete regions of uniform traction acting over annular areas. The contact surface under the indenter is discretized into a number of *Ne* annular ring elements. It is assumed that $p(r)$ and $q(r)$ are constant within each ring element. The vertical and radial surface displacements at the contact surface, Eqs. (4.16) and (4.17), can then be expressed as,

$$\begin{bmatrix} \mathbf{U_z^N} & \mathbf{U_z^R} \\ \mathbf{U_r^N} & \mathbf{U_r^R} \end{bmatrix} \begin{Bmatrix} \mathbf{p} \\ \mathbf{q} \end{Bmatrix} = \begin{Bmatrix} \mathbf{d} \\ \mathbf{0} \end{Bmatrix} \tag{4.21}$$

where the elements $U_z^k\left(r_i, r_j\right)$ and $U_r^k\left(r_i, r_j\right)$ (i,j = 1, 2,…, *Ne*) of matrices $\mathbf{U_z^k}$ and $\mathbf{U_r^k}$ respectively denote the Green's functions corresponding to the normal and radial surface displacements of a layered elastic half-space at the center of the i^{th} ring element subjected to a uniform annular normal load ($k = N$) or a uniform annular radial load ($k = R$) over the j^{th} ring element. Note that uniform annular normal loading is given by Eq. (4.9) whereas uniform annular radial loading can be obtained from the integration of Eq. (4.20). In addition,

$$\mathbf{p} = \left\langle p(r_1) \quad p(r_2) \ldots p(r_{Ne}) \right\rangle^T \tag{4.22}$$

$$\mathbf{q} = \left\langle q(r_1) \quad q(r_2) \ldots q(r_{Ne}) \right\rangle^T \tag{4.23}$$

$$\mathbf{d} = \left\langle d \quad d \quad \ldots \quad d \right\rangle^T \tag{4.24}$$

If a frictionless contact between a rigid flat-ended cylindrical punch and a layered elastic half-space is considered, the shear traction vanishes and the surface displacement at the top surface in Eq. (4.21) is then reduced to

$$\sum_{j=1}^{Ne} U_z^N\left(r_i, r_j\right) \cdot p\left(r_j\right) = d \tag{4.25}$$

Once the normal traction $p(r)$ and the shear traction $q(r)$ in the contact area are obtained, all elastic fields within the bulk material of the layered half-space under

axisymmetric indentation as shown in Figure 4.9 can be determined from the following equation:

$$R(r,z)=\int_0^\infty R^N(r,z;r')\cdot p(r')dr'+\int_0^\infty R^R(r,z;r')\cdot q(r')dr' \tag{4.26}$$

where $R(r,z)$ denotes displacements and stresses at any point (r, z) of the layered elastic half-space; $R^N(r,z;r')$ and $R^R(r,z;r')$ are the Green's functions corresponding to displacements and stresses at any point (r, z) within the bulk material due to a unit normal load and a unit radial load (ring or annular), respectively, acting on the surface of the upper layer at the radius r'. Note that all elastic fields within the bulk material expressed in the forms of Hankel integral transforms are given in Chapter III.

Numerical solution scheme based on the discretization approach in the previous section is implemented into a computer program to study flat-ended cylindrical punch on a layered elastic half-space under adhesive contact as shown in Figure 4.9. The unknown contact traction (both normal and shear) between the rigid indenter and the layered medium can be represented as discrete regions of uniform tractions acting over annular regions as expressed in Eq (4.21). The required Green's functions, $U_i^j(r,r')$, are determined from a layered elastic half-space subjected to a uniform annular load of unit intensity, and the numerical evaluation of these Green's functions is discussed in Chapter III.

The accuracy of the obtained numerical results are validated with existing solutions. First, the present solution is specialized for the case of adhesive contact between flat-ended cylindrical punch of radius a and an elastic half-space without surface stress effects. Figure 4.10 shows comparisons between the numerical solutions from the present study and existing solution given by Spence (1968). The following material parameters are employed: $\lambda_1 = \lambda_2 = 58.17$ GPa and $\mu_1 = \mu_2 = 26.13$ GPa. In addition, the surface parameters are set to be negligibly small in the present solution (i.e. $\tau_1^s = \tau_2^s = \kappa_1^s = \kappa_2^s \approx 0$). Comparisons of normalized contact pressure and surface displacement profiles at the top surface are shown in Figures 4.10 (a) and 4.10 (b) respectively. Numerical results presented in Figure 4.10 (a) indicate that a very good

agreement between the present and benchmark solutions is obtained when *Ne* = 40 for the normalized contact pressures. Similarly, both normal and radial surface displacements obtained from the current study agree very closely with the benchmark solutions with *Ne* = 40 as shown in Figure 4.10 (b).

Figure 4.11 shows the comparison between the present study and an existing solution proposed by Pinyochotiwong et al. (2013) for an axisymmetric rigid frictionless flat-ended punch acting on a homogeneous elastic half-space with the influence of surface stresses. The corresponding surface material constants employed in the present solution defined as τ_1^s = 1 N/m and κ_1^s = 6.0991 N/m at the top surface whereas $\tau_2^s = \kappa_2^s \approx 0$ at the interface. Comparisons of normalized contact pressure and vertical displacement profiles at the top surface shown in Figures 4.11 (a) and 4.11 (b) respectively indicates a very good agreement between the present solution and the benchmark solution (Pinyochotiwong et al., 2013). The accuracy of the proposed solution scheme is thus confirmed through these comparisons.

Next, the influence of surface energy effects on rigid indentation with adhesive contact on a layered elastic half-space is investigated for a flat-ended cylindrical indenter as shown in Figure 4.9. For convenience, the following non-dimensional quantities are used: $\bar{z} = z/\Lambda_1$; $\bar{h} = h/\Lambda_1$; $\bar{a} = a/\Lambda_1$ and $\bar{d} = d/\Lambda_1$. The discretization technique with *Ne* = 40 is used for the numerical results of the adhesive contact problem presented hereafter. In addition, the material properties employed in the top surface and the bulk in the top layer are identical to those considered by Pinyochotiwong et al. (2013) whereas λ_2 = 78.08 GPa, μ_2 = 40.23 GPa for the bulk of the underlying half-space; and τ_2^s = 0.3944 N/m, κ_2^s = -3.9506 N/m at the interface. Note that the broken lines in all figures presented in this section denote the classical solutions corresponding to the indentation on the layered elastic half-space with no surface energy effects (i.e. $\tau^s = \kappa^s \approx 0$). Figures 4.12 (a) and 4.12 (b), respectively display radial profiles of contact pressure and vertical surface displacement under the indenter for both adhesive and frictionless contacts with $\bar{a}$ = 1 and *h/a* = 1. It is evident from Figure 4.12 that the numerical results from the present study and the classical solution exhibit similar trends for both pressure and displacement profiles, and the surface energy influence renders

the layered medium stiffer. Numerical results presented in Figure 4.12 (a) indicates that both classical and present solutions show singular contact traction close to the indenter edge. In addition, the traction developed under the adhesive contact is comparatively higher than that under the frictionless contact due to the presence of adhesion resulting in higher indentation force is then required to produce the same indentation depth.

Figures 4.13 (a) and 4.13 (b) respectively present radial variations of normalized displacements and stresses of a layered elastic half-space under adhesive indentation at different depths for the contact radius of $\bar{a}$ = 1.0 and the layer thickness of h/a = 1. It is evident from Figure 4.13 that the solutions from the present study and the classical elasticity exhibit similar trends. Figure 4.13 (a) indicates that both vertical and radial displacements from the present study are higher than the classical elastic solutions. Numerical results for the normalized vertical stress and shear stress at various depths shown in Figure 4.13 (b) reveal that the presence of surface stresses causes the reduction in stresses under the contact region, whereas outside the contact region the increase of stresses is observed. In addition, the influence of the surface stress becomes negligible when $r/a > 2.5$.

To demonstrate the effect of contact radius a of flat-ended cylindrical punch on a layered elastic half-space with the influence of surface energy, Figures 4.14 (a) and 4.14 (b) show radial variations of normalized contact pressure and surface displacements of the layered half-space with h/a = 1 for different values of the normalized contact radius, i.e. $\bar{a} = a/\Lambda_1$ = 0.5, 1.0 and 1.5. Note that the solution with $\bar{a}$ = 1.0 corresponds to the case where the thickness of the layer is equal to the characteristic length (Λ_1). It can be obviously seen from Figure 4.14 (a) that the singularity of normal and shear tractions is observed close to the edge of indenter for both classical and present solutions. It should be noted that under the adhesive contact normal and radial ring loads have to be applied at $r = a$ in the present solution to account for both ring loadings induced at the indenter edge due to the presence of the residual surface stress. The applied vertical force P would then be supported by both ring loads together with the contact pressure generated under the indenter. The size-dependency of the present solution is clearly observed in contact pressure and displacement profiles shown in Figure 4.14 whereas the classical elasticity solution is size-independent. It is

also found that the influence of surface stress is reduced when the radius of the indenter becomes larger and the present solution eventually converges to the classical solution.

The influence of the residual surface stress (τ^s) on the normalized contact pressure and surface displacement are investigated respectively in Figures 4.15 (a) and 4.15 (b) with $\bar{a}$ = 1 and *h/a* = 1. The ratios of the residual surface stresses at the top surface and interface are varied, i.e. τ_1^s/τ_2^s = 0.5, 1, 2, 4 whereas other material parameters associated with both upper layer and underlying half-space remain unchanged. It is obvious that the normal traction and vertical surface displacement are larger than the shear traction and radial surface displacement. Numerical results in Figure 4.15 show radial variation of normalized contact pressures and surface displacements in the *z*-direction under indentation with adhesive contact. Figure 4.15 (a) indicates that the normal contact pressure from the present study is lower than the classical solution. The normal pressure significantly decreases by increasing the ratio of residual surface stresses. In addition, the numerical results shown in Figure 4.15 (b) reveal that the normalized vertical surface displacements outside the contact area obtained from the present study are higher than the classical solution due to the presence of the residual surface stress, and the layered half-space becomes stiffer with increasing the ratio τ_1^s/τ_2^s.

To study the influence of shear moduli in the layered medium, radial variations of normalized vertical contact pressure and vertical surface displacement with $\bar{a}$ = 1 and *h/a* = 1 for different values of μ_1/μ_2 are shown in Figure 4.16. It is evident from numerical results on contact pressure and vertical displacement shown in Figure 4.16 that the present and classical solutions display similar behaviors for all values of μ_1/μ_2, and the surface energy influence renders the layered medium stiffer. Numerical results presented in Figure 4.16 (a) reveal that the normal contact traction under the surface energy effects is lower than the classical solution. Figure 4.16 (b) also shows that the vertical surface displacements outside the contact area obtained from the present study are higher than the classical solution since higher indentation force is required to produce the same indentation depth due to the existence of surface effects.

To demonstrate the size-dependent behavior, the final set of numerical solutions is concerned with the indentation force on a layered elastic half-space with surface energy effects. Figure 4.17 presents variations of normalized indentation force, P/P_c, with the normalized contact radius $\bar{a}$ for different values of the layer thickness h/a. The dotted lines in the figure indicate the normalized indentation forces corresponding to the frictionless contact where the surface energy effects are considered while the dash line corresponds to the classical adhesive contact where the surface energy effects are ignored (i.e. $\tau^s = \kappa^s \approx 0$). In addition, P_c indicates the indentation force on an elastic half-space ($h/a \to \infty$) for the classical frictionless case. It is obviously seen from Figure 4.17 that the normalized indentation forces show a significant dependence on the thickness of the upper layer and the contact radius for both adhesive and frictionless contacts due to the influence of surface energy effects. The indentation force increases when the layer thickness decreases. This is physically realistic since the upper layer is softer than the underlying half-space the reduction in the upper layer thickness then renders the layered half-space stiffer. In addition, the indentation force decreases with increasing the contact radius converging to the classical one. Thus, size-dependent behavior is once again observed from the results shown in Figure 4.17 and it is confirmed that a larger indentation force is required for adhesive contact than that under frictionless contact to produce the same contact area.

4.4 Conclusion

The influence of surface energy effects on a layered elastic half-space under rigid indentation with consideration of frictionless and adhesive contacts is investigated in this chapter based on Gurtin-Murdoch theory of surface elasticity. The analytical solution of the mixed-boundary value problem of indentation problem is formulated with the displacement Green's functions constructed from the fundamental solutions of a layered elastic medium with consideration of surface stresses derived in Chapter III. The unknow contact pressure distribution under an indenter of axisymmetric profiles is determined by using a discretization technique. The accuracy of the proposed solution scheme is confirmed by comparing with exiting solutions. Presented numerical results both frictionless and adhesive contacts indicate a significant influence of surface energy

effects on elastic fields in the layered medium, especially in the vicinity of the contact area. The presence of surface stresses renders the layered medium stiffer, and size-dependent behavior is observed. In addition, the indentation force depends significantly on the layer thickness, the shear moduli in the layered medium, and the contact radius under the influence of surface stresses. The present solution can be used as a benchmark solution in the development of numerical techniques such as the finite element and boundary element methods for analysis of more complicated problems related to nano-indentation on a layered elastic medium under the influence of surface energy effects.

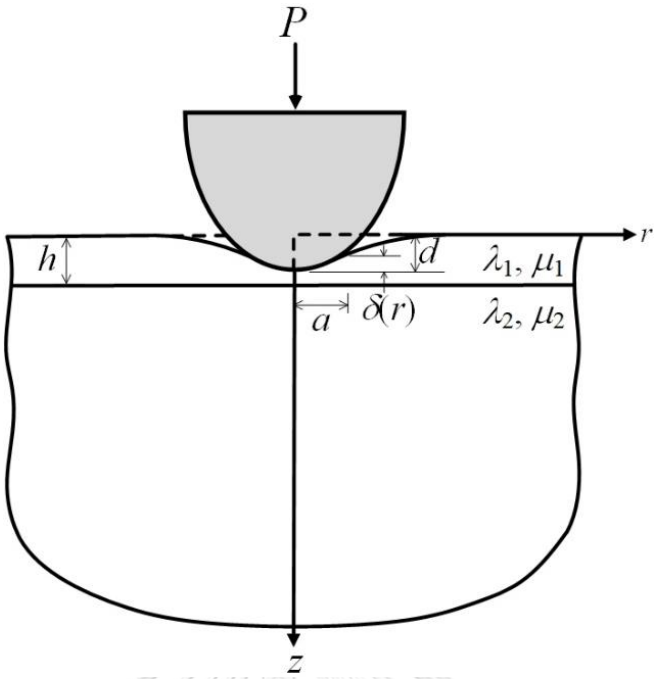

(a)

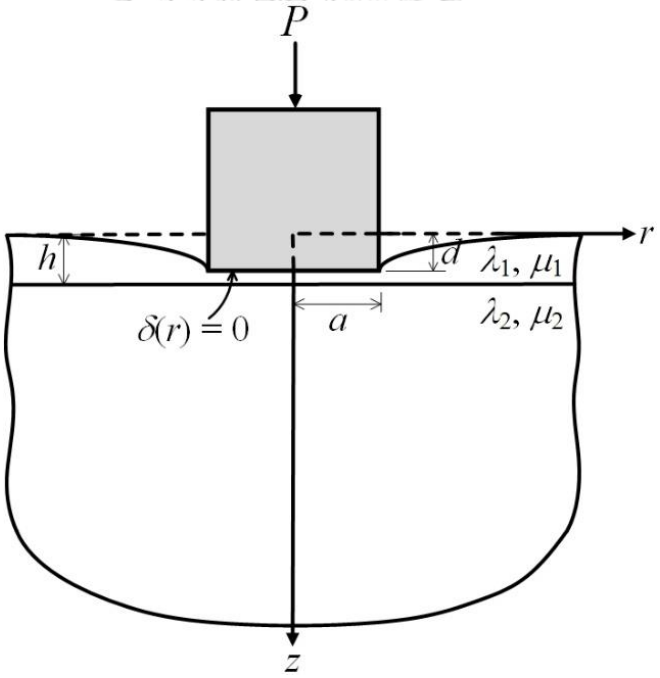

(b)

Figure 4.1 A layered elastic half-space under axisymmetric indentation: (a) paraboloidal indentation and (b) flat-ended cylindrical indentation.

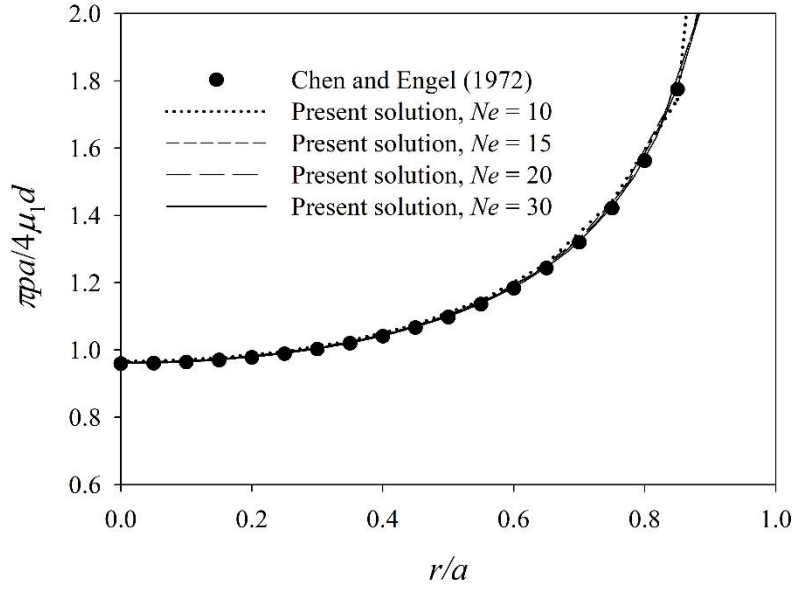

(a)

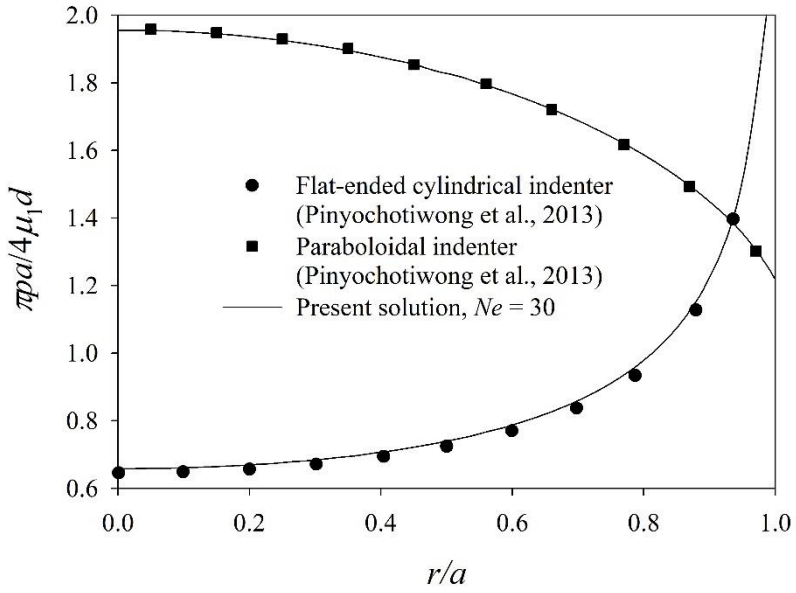

(b)

Figure 4.2 Comparisons of normalized contact pressure: (a) without surface energy effects and (b) with surface energy effects.

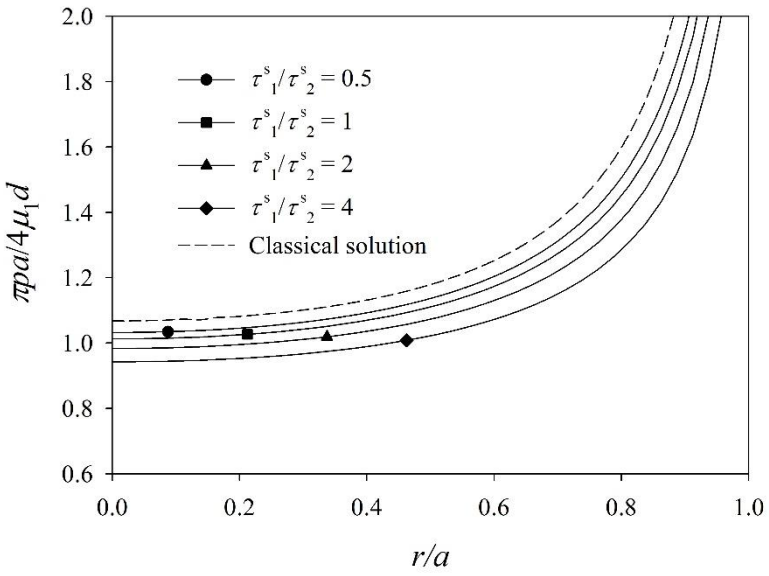

(a)

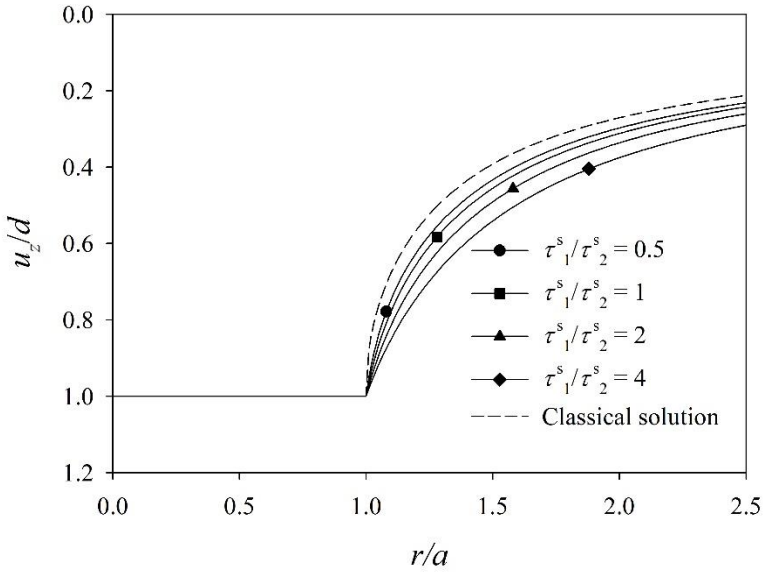

(b)

Figure 4.3 Radial variations of elastic fields under flat-ended cylindrical indenter with $h/a = 1$ and $\bar{a} = 1$ for different values of τ_1^s / τ_2^s: (a) normalized contact pressure and (b) normalized surface displacement.

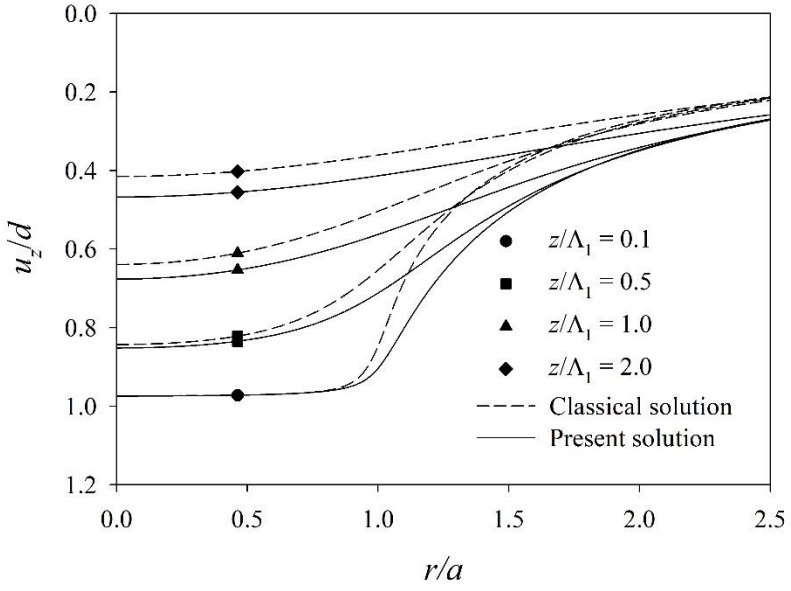

(a)

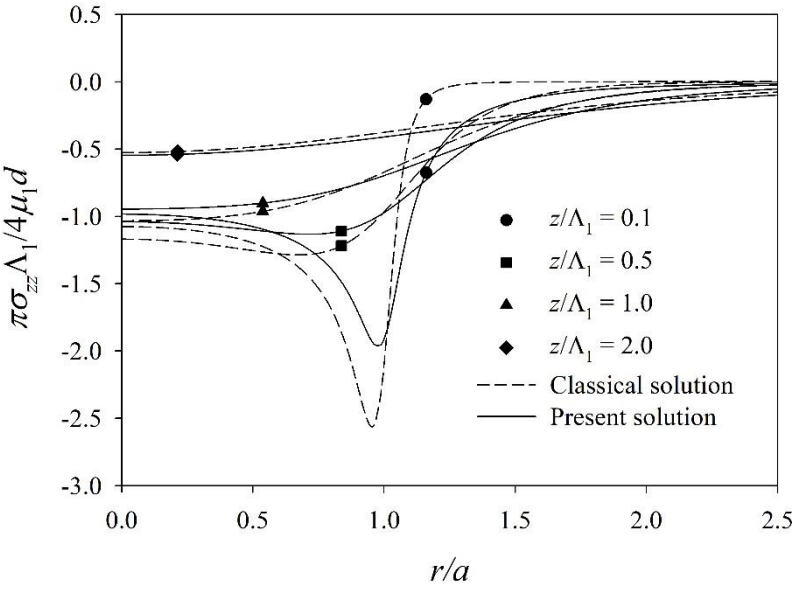

(b)

Figure 4.4 Radial variations of elastic fields at different depths under flat-ended cylindrical indenter with $h/a = 1$ and $\bar{a} = 1$: (a) normalized vertical displacement and (b) normalized vertical stress.

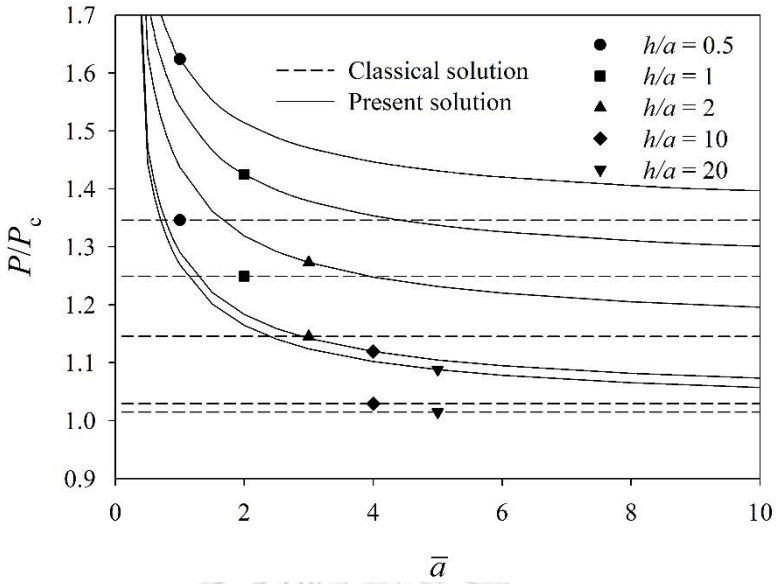

(a)

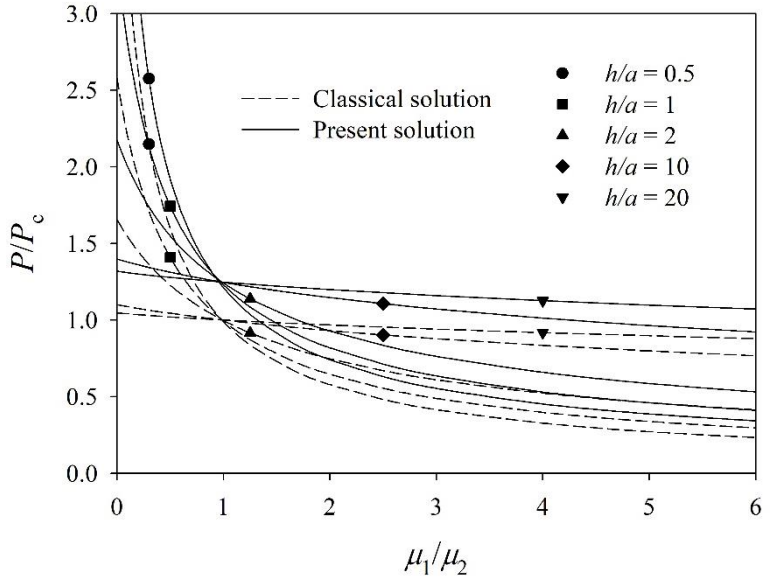

(b)

Figure 4.5 Variations of normalized indentation force under flat-ended cylindrical indenter for various layer thicknesses with (a) contact radius and (b) ratio of shear moduli.

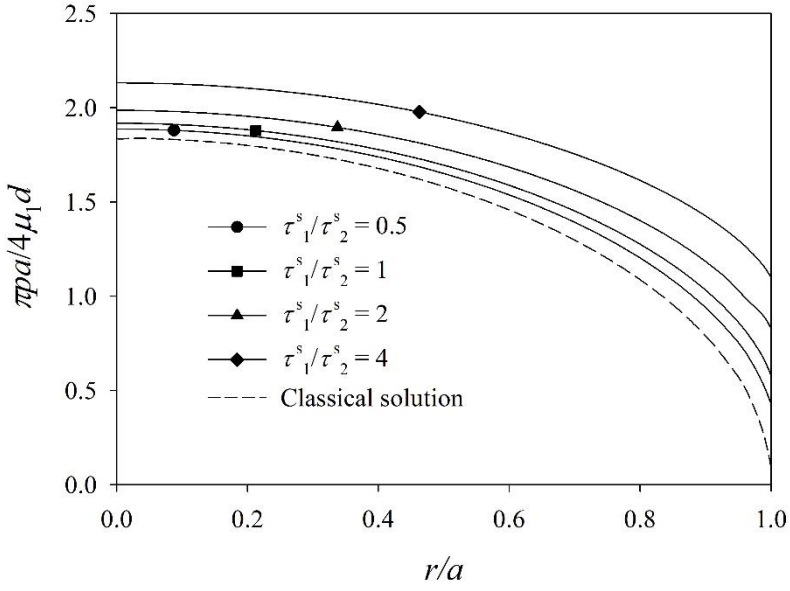

(a)

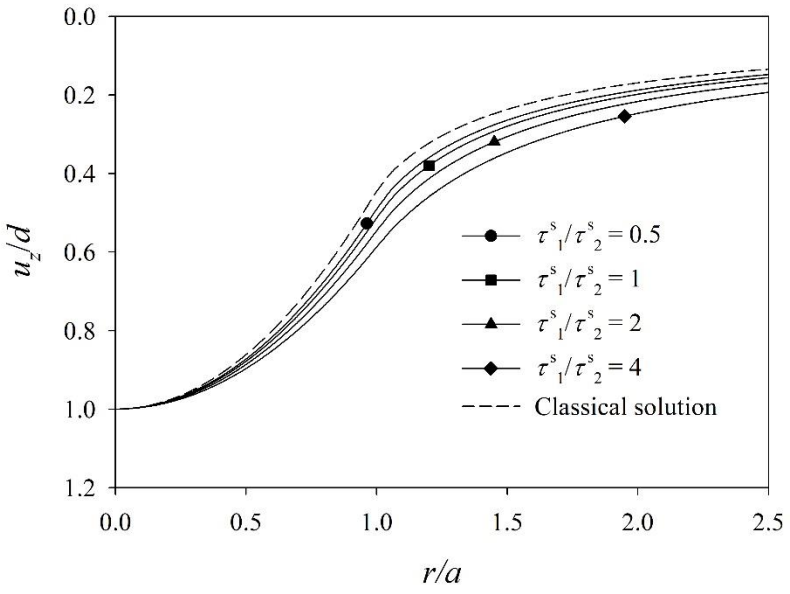

(b)

Figure 4.6 Radial variations of elastic fields under paraboloidal indenter with h/a = 1 and $\bar{a}$ = 1 for different values of τ_1^s / τ_2^s: (a) normalized contact pressure and (b) normalized surface displacement.

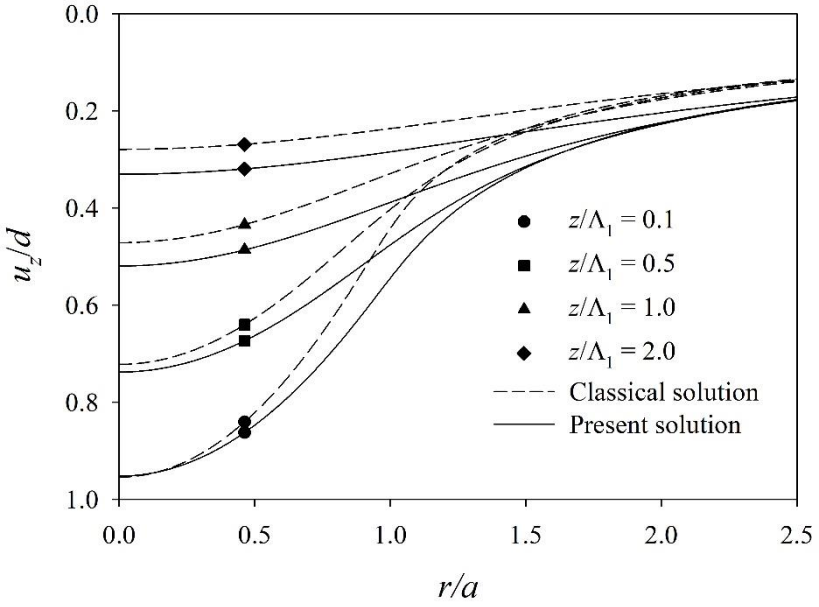

(a)

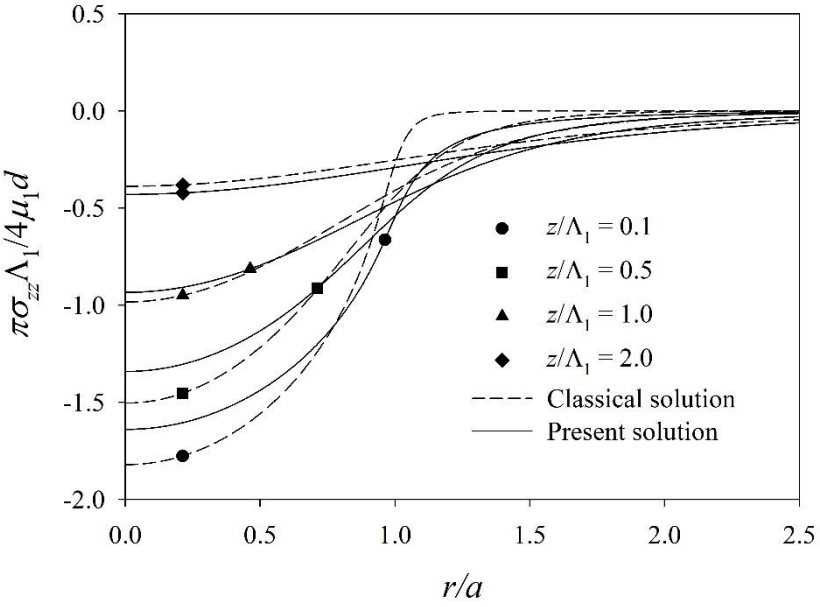

(b)

Figure 4.7 Radial variations of elastic fields at different depths under paraboloidal indenter with h/a = 1 and $\bar{a}$ = 1: (a) normalized vertical displacement and (b) normalized vertical stress.

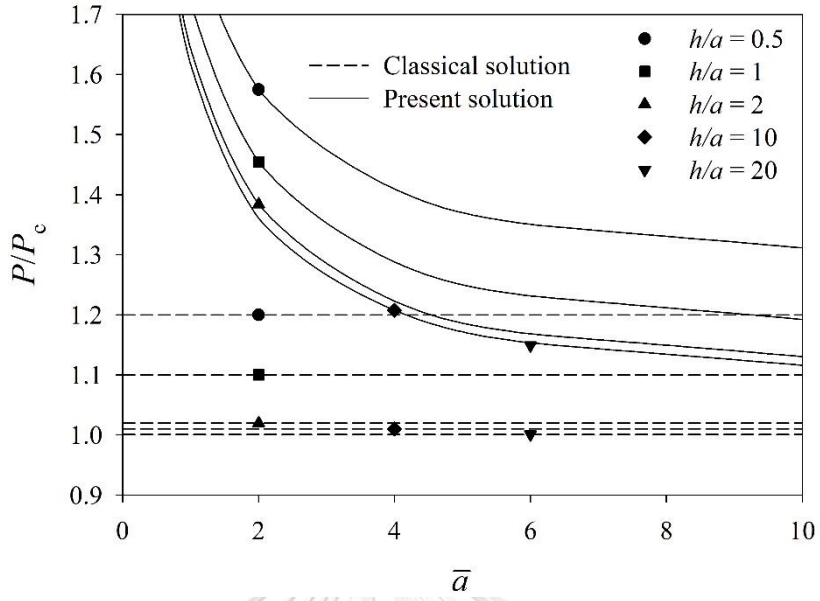

(a)

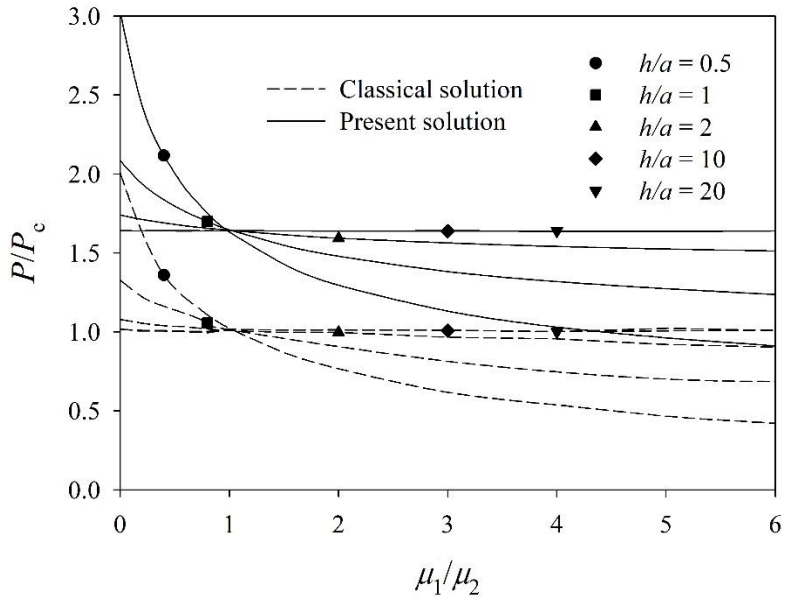

(b)

Figure 4.8 Variations of normalized indentation force under paraboloidal indenter for various layer thicknesses with (a) contact radius and (b) ratio of shear moduli.

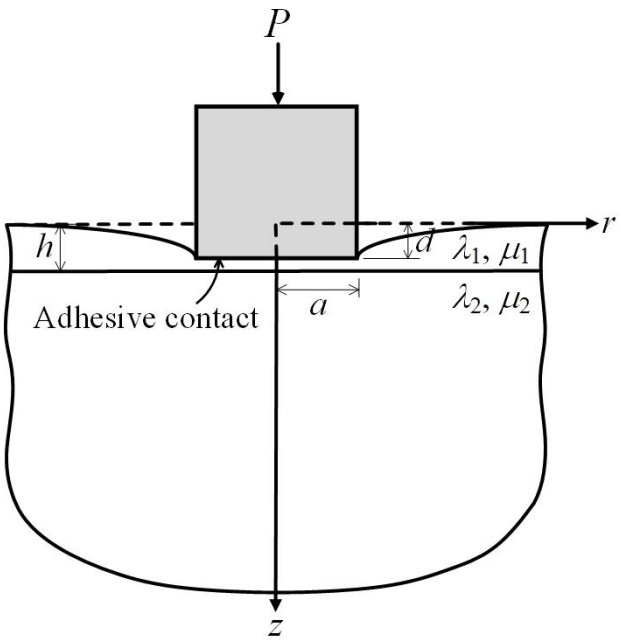

Figure 4.9 An adhesive contact between a rigid flat-ended cylindrical punch of radius a and a layered elastic half-space.

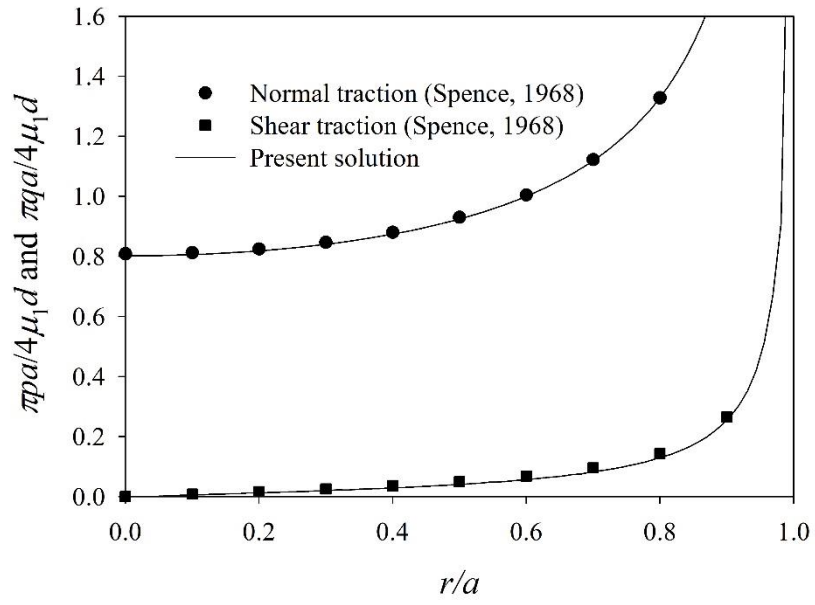

(a)

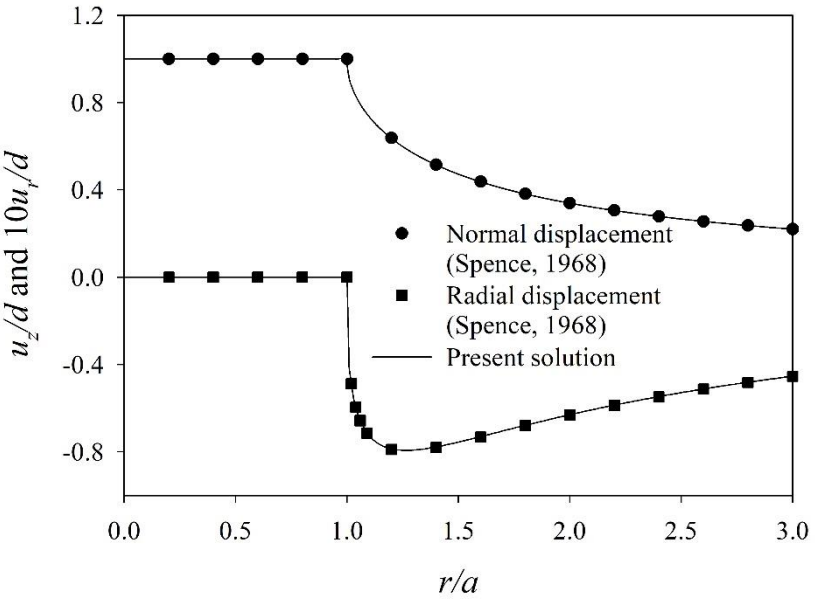

(b)

Figure 4.10 Comparisons of normalized contact pressures and surface displacements for classical numerical solutions with existing solutions under adhesive contact of flat-ended cylindrical indenter: (a) normalized contact pressure and (b) normalized surface displacements.

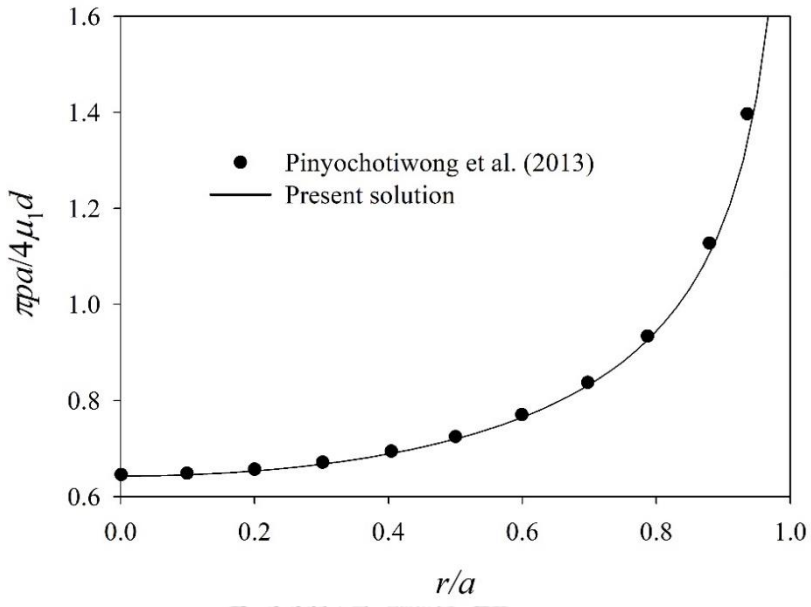

(a)

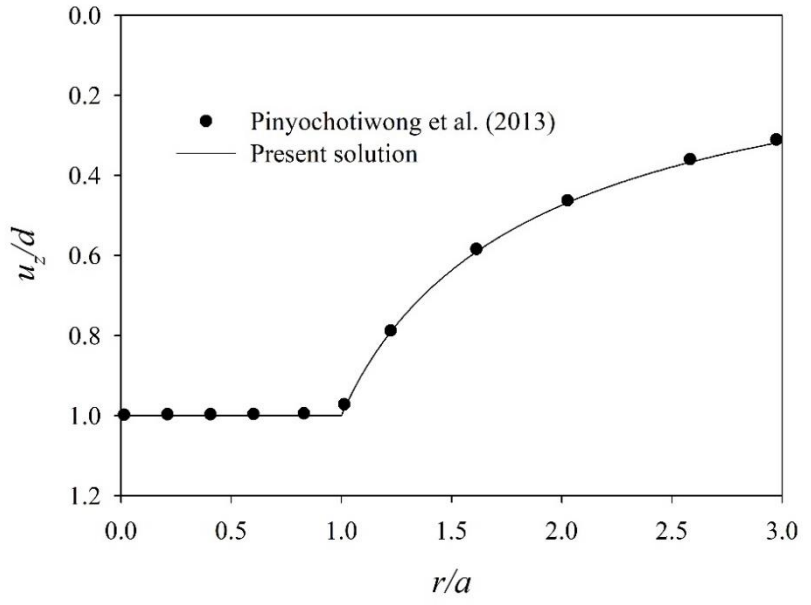

(b)

Figure 4.11 Comparisons of normalized contact pressure and surface displacement for surface effects with existing solutions under frictionless contact of flat-ended cylindrical indenter: (a) normalized contact pressure and (b) normalized surface displacement.

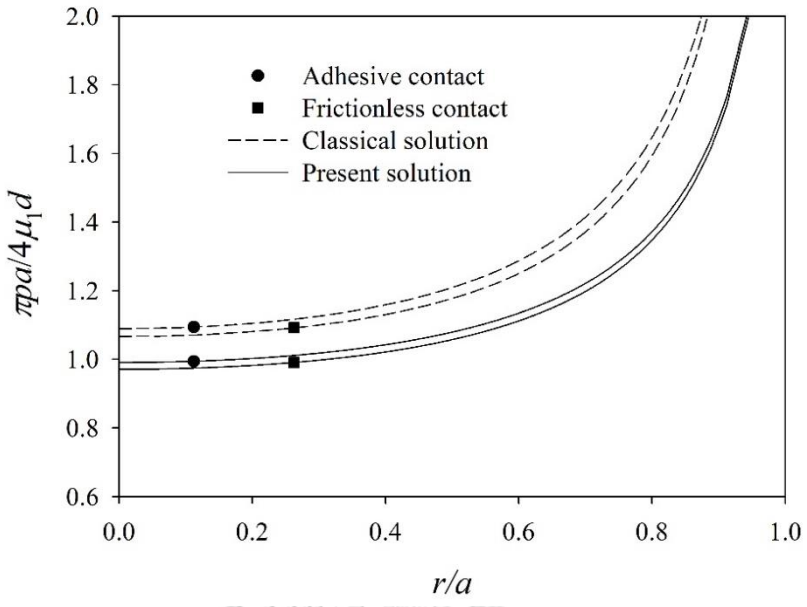

(a)

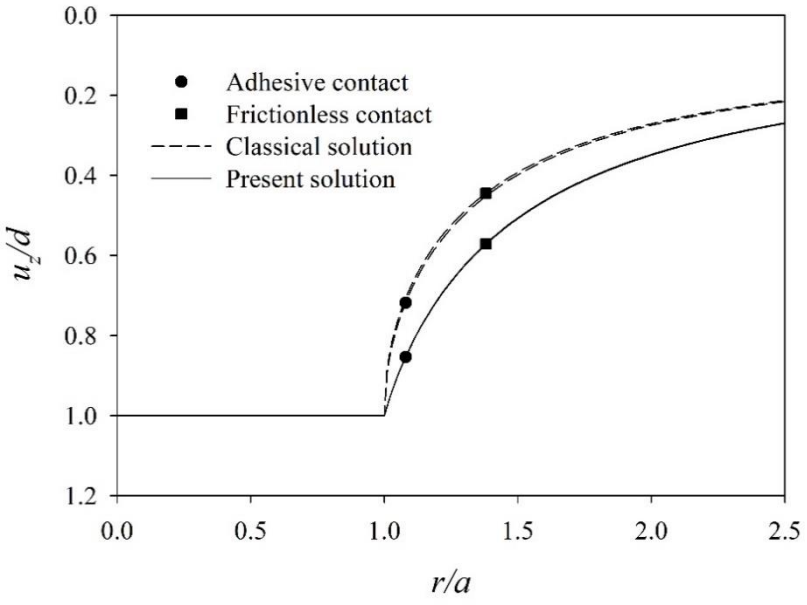

(b)

Figure 4.12 Distribution of normalized contact pressure and vertical surface displacement profiles under flat-ended cylindrical indenter with h/a = 1 and $\bar{a}$ = 1: (a) normalized contact pressure and (b) normalized vertical surface displacement.

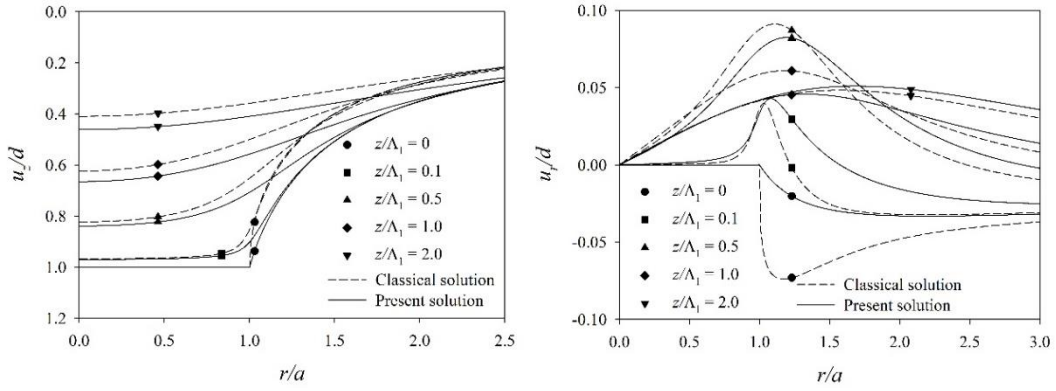

(a)

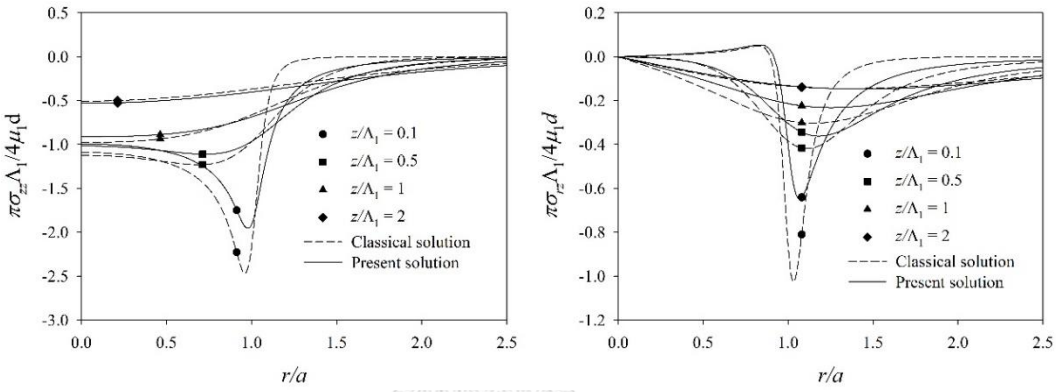

(b)

Figure 4.13 Radial variations of elastic fields at different depths under flat-ended cylindrical indenter with $h/a = 1$ and $\bar{a} = 1$: (a) normalized displacements and (b) normalized stresses.

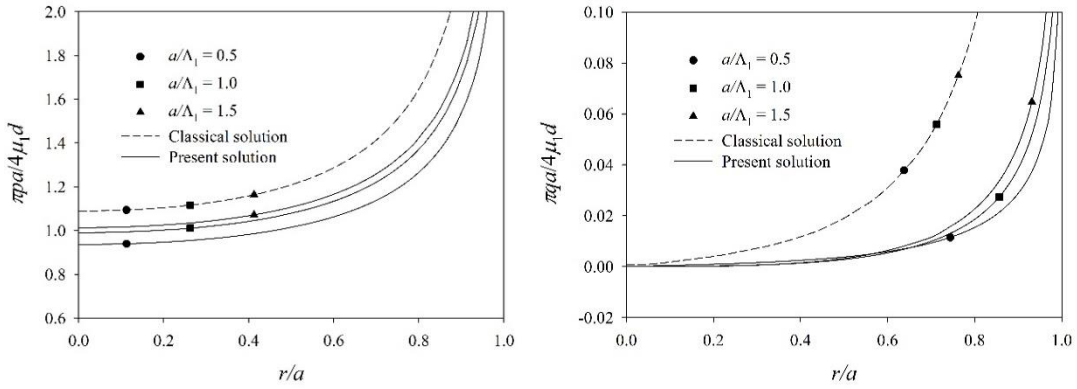

(a)

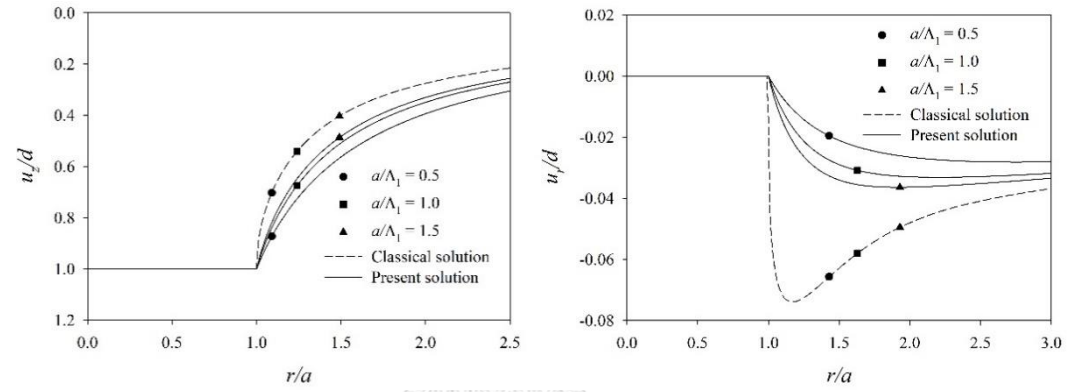

(b)

Figure 4.14 Radial variations of elastic fields under flat-ended cylindrical indenter with $h/a = 1$ for different contact radii $\bar{a}$: (a) normalized contact pressure and (b) normalized surface displacement.

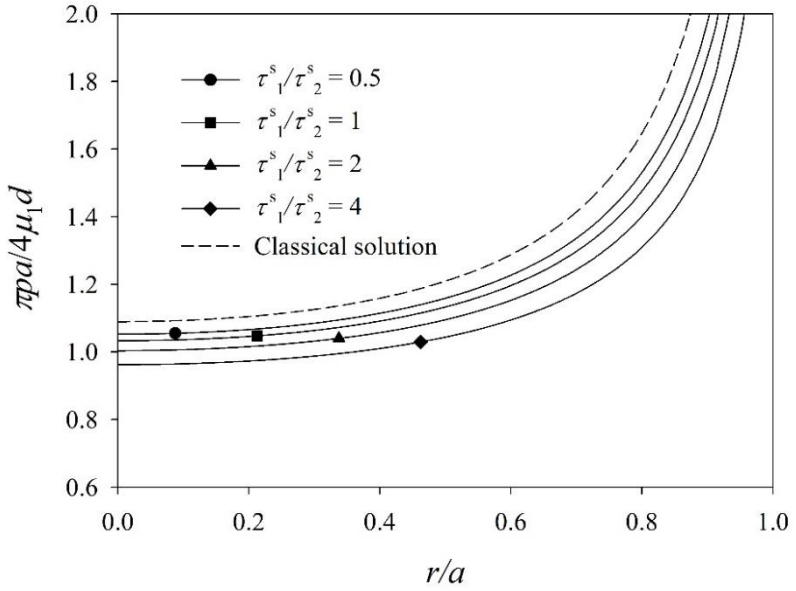

(a)

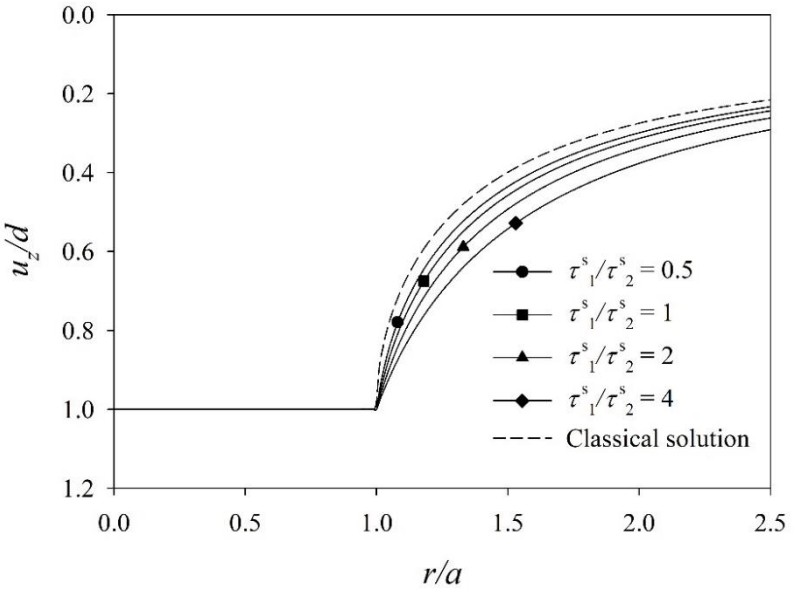

(b)

Figure 4.15 Radial variations of elastic fields under flat-ended cylindrical indenter with h/a = 1 and $\bar{a}$ = 1 for different values of τ_1^s/τ_2^s : (a) normalized contact pressure and (b) normalized surface displacement.

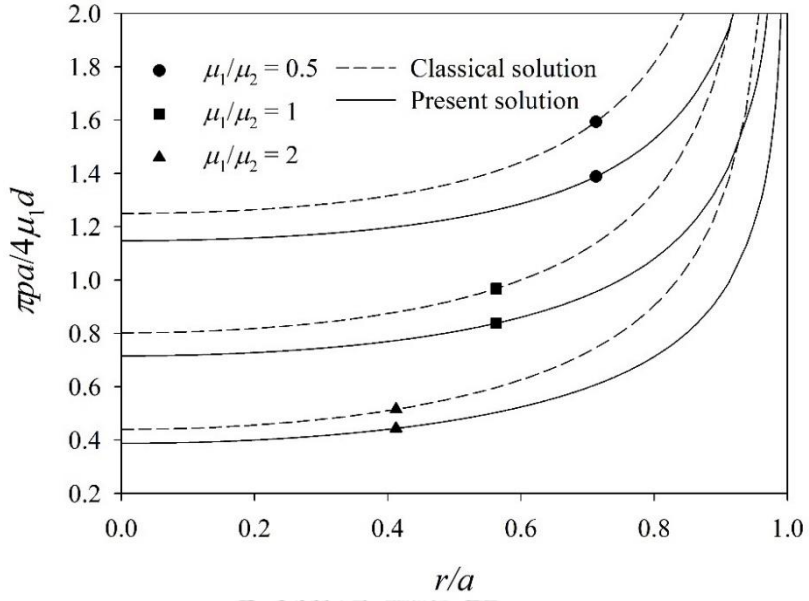

(a)

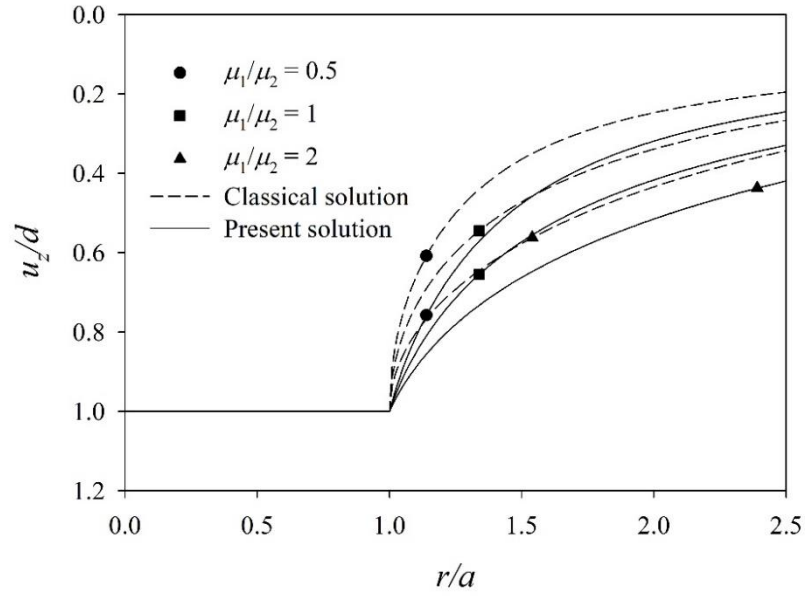

(b)

Figure 4.16 Radial variations of elastic fields under flat-ended cylindrical indenter with h/a = 1 and $\bar{a}$ = 1 for different ratio of shear moduli μ_1/μ_2 : (a) normalized contact pressure and (b) normalized surface displacement.

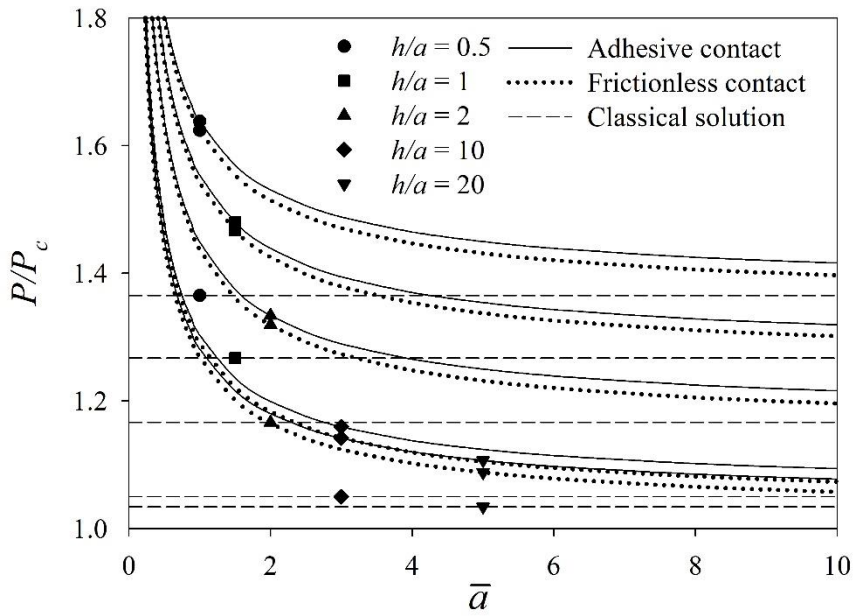

Figure 4.17 Variations of normalized indentation force under flat-ended cylindrical indenter for various layer thicknesses, *h/a* versus contact radius, $\bar{a}$.

CHAPTER V
INTERACTION BETWEEN CIRCULAR NANO-PLATE AND ELASTIC MEDIUM

5.1 General

In this chapter, a variational formulation of interaction problem is presented for the analysis of an elastic circular plate subjected to a concentrated or uniformly distributed loads resting on an isotropic elastic half-space under the influence of surface energy. The Gurtin-Murdoch surface elasticity theory is adopted to take into account the surface energy effects. The contact surface between the plate and the half-space is assumed to be smooth, and the deflected shape of the plate is represented by a power series of the radial coordinate. The undetermined coefficients in the series are determined through the minimization of the total potential energy functional of the plate-half-space system. Selected numerical results are presented to portray the influence of surface energy effects on interaction between an elastic circular plate and an elastic half-space.

5.2 Basic Equations of Circular Nano-Plate

Consider an elastic circular nano-plate of radius *a* subjected to axisymmetric vertical loading as shown in Figure 5.1. A nano-plate based on the Gurtin-Murdoch continuum model has an elastic surface (mathematically zero thickness) perfectly bonded to the bulk material. The displacement fields and the strain-displacement relationship can be expressed as

$$u_r = -z\frac{dw(r)}{dr}; \quad u_z = w(r) \tag{5.1}$$

$$\varepsilon_{rr} = \frac{du_r}{dr} = -z\frac{d^2w(r)}{dr^2}; \quad \varepsilon_{\theta\theta} = \frac{u_r}{r} = -\frac{z}{r}\frac{dw(r)}{dr} \tag{5.2}$$

The stress-strain relationship of the bulk material undergoing axisymmetric deformations can be expressed as

$$\sigma_{rr} = \frac{E_{pl}}{1+\nu_{pl}}\left[\frac{1}{1-\nu_{pl}}\varepsilon_{rr} + \frac{\nu_{pl}}{1-\nu_{pl}}\varepsilon_{\theta\theta}\right] + \frac{\nu_{pl}}{1-\nu_{pl}}\sigma_{zz} \tag{5.3}$$

$$\sigma_{\theta\theta} = \frac{E_{pl}}{1+\nu_{pl}}\left[\frac{1}{1-\nu_{pl}}\varepsilon_{\theta\theta} + \frac{\nu_{pl}}{1-\nu_{pl}}\varepsilon_{rr}\right] + \frac{\nu_{pl}}{1-\nu_{pl}}\sigma_{zz} \tag{5.4}$$

where $\{\sigma_{rr}, \sigma_{\theta\theta}, \sigma_{zz}\}$ denote the stress components; $\{\varepsilon_{rr}, \varepsilon_{\theta\theta}\}$ denote the strain components; $\{u_r, u_z\}$ denote the displacement components of the bulk of the plate respectively.

In the classical thin plate theory, the out of plane stress σ_{zz} is neglected. According to Lim and He (2004); and Lu et al. (2006), the bulk stress σ_{zz} is assumed to vary linearly through the plate thickness to satisfy the equilibrium conditions along the interface, and σ_{zz} can then be expressed as,

$$\sigma_{zz} = \frac{1}{2}\left(\sigma_{zz}^{+} + \sigma_{zz}^{-}\right) + \frac{z}{h_{pl}}\left(\sigma_{zz}^{+} - \sigma_{zz}^{-}\right) \tag{5.5}$$

where σ_{zz}^{+} and σ_{zz}^{-} are the stresses at the top and bottom surfaces respectively of the bulk of the plate. From the Gurtin-Murdoch theory of surface elasticity, the normal stress σ_{zz} can be rewritten in terms of surface stresses in Eqs. (3.5) to (3.8) as

$$\sigma_{zz} = \frac{1}{2}\left(\frac{\partial\sigma_{zr}^{s+}}{\partial r} + \frac{\sigma_{zr}^{s+}}{r} - \frac{\partial\sigma_{zr}^{s-}}{\partial r} - \frac{\sigma_{zr}^{s-}}{r}\right) + \frac{z}{h_{pl}}\left(\frac{\partial\sigma_{zr}^{s+}}{\partial r} + \frac{\sigma_{zr}^{s+}}{r} + \frac{\partial\sigma_{zr}^{s-}}{\partial r} + \frac{\sigma_{zr}^{s-}}{r}\right) \tag{5.6}$$

$$\sigma_{zz} = \frac{z}{h_{pl}}\left(2\tau_{pl}^{s}\frac{d^2w}{dr^2} + \frac{2\tau_{pl}^{s}}{r}\frac{dw}{dr}\right) = \frac{2\tau_{pl}^{s}z}{h_{pl}}\left(\frac{d^2w}{dr^2} + \frac{1}{r}\frac{dw}{dr}\right) \tag{5.7}$$

where the superscript "*s*" is used to denote the quantities corresponding to the surface material; τ_{pl}^{s} is the residual surface stress (or surface tension) under unstrained conditions of the plate. In addition, the other normal stresses in terms of generalized displacement, $w(r)$ can be expressed as

$$\sigma_{rr} = \frac{E_{pl}}{1+\nu_{pl}}\left[\frac{1}{1-\nu_{pl}}\left(-z\frac{d^2w}{dr^2}\right) + \frac{\nu_{pl}}{1-\nu_{pl}}\left(-\frac{z}{r}\frac{dw}{dr}\right)\right] + \frac{\nu_{pl}}{1-\nu_{pl}}\frac{2\tau_{pl}^{s}z}{h_{pl}}\left(\frac{d^2w}{dr^2} + \frac{1}{r}\frac{dw}{dr}\right) \tag{5.8}$$

$$\sigma_{\theta\theta} = \frac{E_{pl}}{1+\nu_{pl}}\left[\frac{1}{1-\nu_{pl}}\left(-\frac{z}{r}\frac{dw}{dr}\right)+\frac{\nu_{pl}}{1-\nu_{pl}}\left(-z\frac{d^2w}{dr^2}\right)\right]+\frac{\nu_{pl}}{1-\nu_{pl}}\frac{2\tau_{pl}^{s}z}{h_{pl}}\left(\frac{d^2w}{dr^2}+\frac{1}{r}\frac{dw}{dr}\right) \quad (5.9)$$

where E_{pl} and ν_{pl} are Young's modulus and Poisson's ratio of the plate material respectively; h_{pl} is the thickness of the plate.

5.3 Total Potential Energy of Circular Nano-Plate

The total potential energy of an elastic circular nano-plate consists of the strain energies of the plate and the surface together with the potential energies of point force *P* and axisymmetric vertical loading *p*(*r*) as shown in Figure 5.1. The deflection of the plate in the *z*-direction denoted by *w*(*r*) can be represented by the following kinematically admissible form as

$$w(r) = a_0 r^2 \ln r + \sum_{n=0}^{N} \alpha_n r^{2n}; \quad 0 \le r \le a \quad (5.10)$$

where

$$a_0 = \frac{P}{8\pi D^*} \text{ and } D^* = \frac{E_{pl} h_{pl}^{\ 3}}{12\left(1-\nu_{pl}^{\ 2}\right)} \quad (5.11)$$

In addition, α_n (n = 0, 1, …, N) denotes a set of generalized coordinates. The term $r^2 \ln r$ is incorporated in the deflection form, Eq. (5.10), to simulate the singular stress resultants at the plate origin due to the presence of concentrated force *P*.

The strain energy U_P of the plate contains two parts, i.e., the elastic strain energy stored in the bulk material (U_B) and the elastic strain energy of the surface (U_S), which are expressed respectively as

$$U_B = \frac{1}{2}\int_V \left(\sigma_{rr}\varepsilon_{rr} + \sigma_{\theta\theta}\varepsilon_{\theta\theta}\right) dV \quad (5.12)$$

$$U_S = \frac{1}{2}\int_\Gamma \left(\sigma_{rr}^{s\pm}\varepsilon_{rr}^{s\pm} + \sigma_{\theta\theta}^{s\pm}\varepsilon_{\theta\theta}^{s\pm} + 2\sigma_{rz}^{s\pm}\varepsilon_{rz}^{s\pm}\right) d\Gamma \quad (5.13)$$

where V and Γ are the bulk volume and the surface area of the plate respectively.

The expression of the strain energy U_P of a thin circular nanoplate in terms of generalized coordinates $\alpha_1, \alpha_2, ..., \alpha_N$ is written in the following matrix form:

$$U_P = \pi a_0^2 a^2 \left(3D + D_1 + \frac{\tau_{pl}^s a^2}{4} \right) + \pi a_0^2 a^2 \ln a \left(4D + 4D_1 + \tau_{pl}^s a^2 \right)$$

$$+2\pi a_0^2 a^2 \left(\ln a \right)^2 \left(2D + 2D_1 + \tau_{pl}^s a^2 \right) + 4\pi a_0 \ln a \left(D \left\langle \mathbf{Q^{p1}} \right\rangle + D_1 \left\langle \mathbf{Q^{p2}} \right\rangle + 2\tau_{pl}^s \left\langle \mathbf{Q^{p3}} \right\rangle \right) \{\boldsymbol{\alpha}\}$$

$$+2\pi a_0 \left(2D \left\langle \mathbf{Q^{p4}} \right\rangle + D_1 \left\langle \mathbf{Q^{p5}} \right\rangle + 4\tau_{pl}^s \left\langle \mathbf{Q^{p6}} \right\rangle \right) \{\boldsymbol{\alpha}\}$$

$$+ \{\boldsymbol{\alpha}\}^T \left(\pi D \left[\mathbf{K^{P1}} \right] + 2\pi D_1 \left[\mathbf{K^{P2}} \right] + 2\pi \tau_{pl}^s \left[\mathbf{K^{P3}} \right] \right) \{\boldsymbol{\alpha}\} \tag{5.14}$$

The elements $\left\langle \mathbf{Q_i^p} \right\rangle$ of order (N+1), and $\left[\mathbf{K^{Pi}} \right]$ of order (N+1)×(N+1), are given by

$$\mathbf{Q_i^{P1}} = 2ia^{2i} \tag{5.15}$$

$$\mathbf{Q_i^{P2}} = 2ia^{2i} \tag{5.16}$$

$$\mathbf{Q_i^{P3}} = \frac{2ia^{2i+2}}{2i+2} \tag{5.17}$$

$$\mathbf{Q_i^{P4}} = (3i-2)a^{2i} \tag{5.18}$$

$$\mathbf{Q_i^{P5}} = 2ia^{2i} \tag{5.19}$$

$$\mathbf{Q_i^{P6}} = \frac{2i^2 a^{2i+2}}{(2i+2)^2} \tag{5.20}$$

$$\mathbf{K_{ij}^{P1}} = \frac{4ij \cdot a^{2i+2j-2}}{2i+2j-2} \left[(2i-1)(2j-1)+1 \right] \tag{5.21}$$

$$\mathbf{K_{ij}^{P2}} = \frac{4ij(2j-1) \cdot a^{2i+2j-2}}{2i+2j-2} \tag{5.22}$$

$$\mathbf{K}_{\mathbf{ij}}^{\mathbf{P3}} = \frac{4ij \cdot a^{2i+2j}}{2i+2j} \tag{5.23}$$

The total potential energy I_P of the plate contains two parts, i.e., the strain energy of the plate (U_P) and the potential energy of external forces (W) as shown in Figure 5.1. In addition, the potential energy due to a vertical load $p(r)$ as shown in Figure 5.1 is written as

$$W = -\int_{\Gamma} p(r)\, w(r)\, d\Gamma \tag{5.24}$$

In view of Eqs. (5.12), (5.13) and (5.24), the total potential energy I_P of nano-plate is given by,

$$I_P = U_P + W \tag{5.25}$$

$$I_P = \pi \int_0^r \left\{ \frac{E_{pl} h_{pl}^3}{12\left(1-\nu_{pl}^2\right)} \left[\left(\frac{d^2 w}{dr^2} + \frac{1}{r}\frac{dw}{dr} \right)^2 - \frac{2\left(1-\nu_{pl}\right)}{r} \frac{dw}{dr} \frac{d^2 w}{dr^2} \right] - \frac{\tau_{pl}^s \nu_{pl} h_{pl}^2}{6\left(1-\nu_{pl}\right)} \left[\frac{d^2 w}{dr^2} + \frac{1}{r}\frac{dw}{dr} \right]^2 \right\} r dr$$

$$+\pi \int_0^r \left\{ \left(\lambda_{pl}^s + 2\mu_{pl}^s\right) \frac{h_{pl}^2}{2} \left[\left(\frac{d^2 w}{dr^2} \right)^2 + \left(\frac{1}{r}\frac{dw}{dr} \right)^2 \right] + 2\tau_{pl}^s \left[\frac{dw}{dr} \right]^2 + \left(\lambda_{pl}^s + \tau_{pl}^s\right) h_{pl}^2 \left[\frac{1}{r}\frac{dw}{dr}\frac{d^2 w}{dr^2} \right] \right\} r dr$$

$$+\pi \int_0^r \left\{ -2\, p(r) \cdot w(r) \right\} r dr \tag{5.26}$$

where λ_{pl}^s and μ_{pl}^s are surface Lamé constants for the elastic plate.

The minimization of I_P in Eq. (5.26) together with the integration by parts leads to the governing equation for a circular nano-plate

$$D\nabla^4 w - 2\tau_{pl}^s \nabla^2 w - p(r) = 0 \tag{5.27}$$

where

$$D = \frac{E_{pl} h_{pl}^3}{12\left(1-\nu_{pl}^2\right)} + \left(\lambda_{pl}^s + 2\mu_{pl}^s\right) \frac{h_{pl}^2}{2} - \frac{\tau_{pl}^s \nu_{pl} h_{pl}^2}{6\left(1-\nu_{pl}\right)} \tag{5.28}$$

and

$$\nabla^2 = \frac{1}{r}\frac{d}{dr}\left(r\frac{d}{dr}\right) \tag{5.29}$$

The bending moment and shear force of circular nano-plate are given respectively by

$$M_r = D\frac{d^2w}{dr^2} + \frac{D_1}{r}\frac{dw}{dr} \tag{5.30}$$

$$Q_r = -D\frac{d}{dr}\nabla^2 w + 2\tau_{pl}^s\frac{dw}{dr} \tag{5.31}$$

where

$$D_1 = \frac{\nu_{pl}E_{pl}h_{pl}^3}{12\left(1-\nu_{pl}^2\right)} + \left(\lambda_{pl}^s + \tau_{pl}^s\right)\frac{h_{pl}^2}{2} - \frac{\tau_{pl}^s\nu_{pl}h_{pl}^2}{6\left(1-\nu_{pl}\right)} \tag{5.32}$$

Equations (5.27) to (5.32) are identical to the governing equation for a nano-plate derived by Liu and Rajapakse (2013) from the equilibrium of an infinitesimal plate element. This equation reduces to the classical Kirchhoff equation when the surface energy effects is completely neglected (i.e., μ_{pl}^s, λ_{pl}^s and τ_{pl}^s are set to zero).

5.4 Variational Formulation of Interaction Problem

Consider an elastic circular nano-plate of radius *a* under axisymmetric vertical loading resting on an elastic half-space as shown in Figure 5.2 with the consideration of surface energy effects. For interaction problem, the circular plate under axisymmetric vertical loading is resisted by the normal contact traction acting on bottom surface of the plate. Let *S* denote the circular contact area between the plate and the supporting medium. The normal traction can be represented by a traction field $T_z(r)$ acting on the circular surface *S*. The strain energy U_h of the elastic half-space can be expressed in the following form:

$$U_h = \frac{1}{2}\int_0^a \left[2\pi r T_z\left(r\right)w\left(r\right)\right]dr \tag{5.33}$$

Note that $T_z\left(r\right)$ can be expressed in terms of generalized coordinates α_n as follows:

$$T_z(r) = \sum_{n=0}^{N} \alpha_n T_{zn}(r) + a_0 T^*(r) \tag{5.34}$$

where $T_{zn}(r)$ and $T^*(r)$ denote the tractions in the vertical direction applied over S such that the vertical displacements within S is equal to r^{2n} and $r^2 \ln r$, respectively.

To determine the traction $T_z(r)$, the circular contact area S is discretized into a number of Ne annular ring elements as shown in Figure 5.3. It is assumed that $T_{zn}(r)$ is constant within each ring element. The unknown contact traction $T_{zn}(r)$ is then evaluated by solving a flexibility equation based on the Green's function of an elastic half-space with consideration of surface energy effects under axisymmetric vertical loading. The Green's function can be expressed in the form of Hankel integral transform as (Intarit, 2012).

$$U_z^N(r_i, r_j) = \int_0^\infty \left\{ \frac{\lambda_h + 2\mu_h}{\mu_h(\lambda_h + \mu_h)} + \left(\frac{\lambda_h + 4\mu_h}{\lambda_h + 2\mu_h} \right) \frac{\Lambda\xi}{\mu_h} \right\} \frac{\left[r_i' J_1(\xi r_i') - r_o' J_1(\xi r_o') \right] J_0(\xi r_i)}{2\eta\xi} d\xi \tag{5.35}$$

$$\eta = (1 + \Lambda\xi) + \frac{\tau_h^s \xi}{2\mu_h} \left(\frac{\lambda_h + 2\mu_h}{\lambda_h + \mu_h} + \frac{\lambda_h + 3\mu_h}{\lambda_h + 2\mu_h} \Lambda\xi \right) \tag{5.36}$$

$$\Lambda = \left(\lambda_h^s + 2\mu_h^s \right) (\lambda_h + 2\mu_h) \Big/ 2\mu_h (\lambda_h + \mu_h) \tag{5.37}$$

where λ_h and μ_h are Lamé constants of the elastic half-space; λ_h^s and μ_h^s are surface Lamé constants at the top surface of the elastic half-space; τ_h^s is the residual surface stress (or surface tension) under unstrained conditions at the top surface of the elastic half-space. In addition, $r_i' = r_j - (\Delta r_j / 2)$ and $r_o' = r_j + (\Delta r_j / 2)$ are inner and outer radii of the annular loading.

The traction $T_{zn}(r_i)$ acting on the i^{th} ring element ($i = 1, \ldots, Ne$) is determined by solving the flexibility equation:

$$\left[\mathbf{U}_\mathbf{z}^\mathbf{N} \right] \{ \mathbf{T_{zn}} \} = \{ \mathbf{w_n} \} \; ; \; n = 0, \ldots, N \tag{5.38}$$

The elements $\mathbf{U}_{\mathbf{zij}}^{\mathbf{N}}$, $\mathbf{T_{zni}}$ and $\mathbf{w_{ni}}$ of $\left[\mathbf{U}_\mathbf{z}^\mathbf{N} \right]$, $\{ \mathbf{T_{zn}} \}$ and $\{ \mathbf{w_n} \}$ respectively are given by

$$\mathbf{U}_{\mathbf{zij}}^{\mathbf{N}} = U_z^N\left(r_i, r_j\right) \tag{5.39}$$

$$\mathbf{T}_{\mathbf{zni}} = T_{zn}\left(r_i\right) \tag{5.40}$$

$$\mathbf{w}_{\mathbf{ni}} = r_i^{2n} \tag{5.41}$$

where $U_z^N\left(r_i, r_j\right)$ (i, j = 1, 2, …, Ne) denotes the Green's function corresponding to vertical surface displacement of an elastic half-space with consideration of surface energy effects at the centre of the i^{th} ring element due to a uniform annular normal load over the j^{th} ring element. In addition, the traction $T^*(r_i)$ acting on the i^{th} ring element (i = 1, …, Ne) is determined by solving Eq. (5.38) with $w_n = r_i^2 \ln r_i$.

From Eqs. (5.10) and (5.34), U_h in Eq. (5.33) can be expressed as

$$U_h = \left\{\boldsymbol{\alpha}\right\}^T \left[\mathbf{K}^{\mathbf{h}}\right]\left\{\boldsymbol{\alpha}\right\} + \left\langle\mathbf{Q}^{\mathbf{h}}\right\rangle\left\{\boldsymbol{\alpha}\right\} + \pi a_0^2 \sum_{j=1}^{Ne} \Delta r_j T_{zj}^* r_j^3 \ln r_j \tag{5.42}$$

The elements $\mathbf{K}_{\mathbf{ij}}^{\mathbf{h}}$ of $\left[\mathbf{K}^{\mathbf{h}}\right]$, of order ($N$+1)×($N$+1) is given by

$$\mathbf{K}_{\mathbf{ij}}^{\mathbf{h}} = \pi \sum_{l=1}^{Ne} \Delta r_l T_{z(i-1)}\left(r_l\right) \cdot r_l^{(2j-1)};\ 1 \le i, j \le (N+1) \tag{5.43}$$

The elements $\mathbf{Q}_{\mathbf{i}}^{\mathbf{h}}$ of $\left\langle\mathbf{Q}^{\mathbf{h}}\right\rangle$ in Eq. (5.42) are given by

$$\mathbf{Q}_{\mathbf{i}}^{\mathbf{h}} = a_0 \sum_{j=1}^{Ne} \left[\pi \Delta r_j T_{zj}^* r_j^{2i-1} + \pi \Delta r_j T_{z(i-1)}\left(r_j\right) \cdot r_j^3 \ln r_j\right];\ 1 \le i \le (N+1) \tag{5.44}$$

The total potential energy I of an elastic circular nano-plate-half-space system under the influence of surface energy consists of the strain energies of the nano-plate (U_P) and the half-space (U_h) given by Eqs. (5.14) and (5.42), respectively, and the potential energies of point force P and uniformly distributed loading p_0 as shown in Figure 5.2 which can be expressed in terms of the generalized coordinates α_i (i = 0, 1, …, N) as

$$I = \pi a_0^2 a^2 \left(3D + D_1 + \frac{\tau_{pl}^s a^2}{4}\right) + \pi a_0^2 a^2 \ln a\left(4D + 4D_1 + \tau_{pl}^s a^2\right) + 2\pi a_0^2 a^2 \left(\ln a\right)^2 \left(2D + 2D_1 + \tau_{pl}^s a^2\right)$$

$$+4\pi a_0 \ln a\left(D\left\langle \mathbf{Q_1^p}\right\rangle + D_1\left\langle \mathbf{Q_2^p}\right\rangle + 2\tau_{pl}^s\left\langle \mathbf{Q_3^p}\right\rangle\right)\{\boldsymbol{\alpha}\} + 2\pi a_0\left(2D\left\langle \mathbf{Q_4^p}\right\rangle + D_1\left\langle \mathbf{Q_5^p}\right\rangle + 4\tau_{pl}^s\left\langle \mathbf{Q_6^p}\right\rangle\right)\{\boldsymbol{\alpha}\}$$

$$+\{\boldsymbol{\alpha}\}^T\left(\pi D\left[\mathbf{K^{P1}}\right] + 2\pi D_1\left[\mathbf{K^{P2}}\right] + 2\pi\tau_{pl}^s\left[\mathbf{K^{P3}}\right] + \left[\mathbf{K^h}\right]\right)\{\boldsymbol{\alpha}\} + \left\langle \mathbf{Q^h}\right\rangle\{\boldsymbol{\alpha}\}$$

$$+\pi a_0^2\sum_{j=1}^{Ne}\Delta r_j T_{zj}^* r_j^3 \ln r_j - P\alpha_0 - 2\pi p_0\sum_{n=0}^{N}\alpha_n \cdot a^{2n+2}/(2n+2) \tag{5.45}$$

For an elastic nano-plate resting on the surface of an elastic medium, as shown in Figure 5.2, the plate deflection is such that it satisfies the following boundary conditions along the edge of the plate at $r = a$:

$$M_r(a) = 0 \text{ and } Q_r(a) = 0 \tag{5.46}$$

By using equations (5.30) and (5.31), the boundary conditions can be expressed as two linear equations in the generalized coordinates α_n (n = 0, 1, 2, …, N):

$$[\mathbf{B}]\{\boldsymbol{\alpha}\} = \{\mathbf{R}\} \tag{5.47}$$

where

$$\{\boldsymbol{\alpha}\} = \langle \alpha_0\ \alpha_1 \ldots \alpha_N \rangle^T \tag{5.48}$$

The elements $\mathbf{B_{ij}}$ and $\mathbf{R_i}$ of $[\mathbf{B}]$ and $\{\mathbf{R}\}$, of order 2×(N+1) and 2 respectively, are given by

$$\mathbf{B_{1j}} = 2(j-1)(2j-3)Da^{2j-4} + 2(j-1)D_1 a^{2j-4};\quad 1 \le j \le N+1 \tag{5.49}$$

$$\mathbf{B_{2j}} = -4(j-1)^2(2j-4)Da^{2j-5} + 4\tau_{pl}^s(j-1)a^{2j-3};\quad 1 \le j \le N+1 \tag{5.50}$$

$$\mathbf{R_1} = -D(3a_0 + 2a_0 \ln a) - D_1(a_0 + 2a_0 \ln a) \tag{5.51}$$

$$\mathbf{R_2} = \frac{4Da_0}{a} - 2\tau_{pl}^s(a_0 a + 2a_0 a \ln a) \tag{5.52}$$

In order to satisfy the boundary condition along the edge of the plate given by Eq. (5.47), the total potential energy defined by Eq. (5.45) can be rewritten as

$$\bar{I} = I + \frac{1}{2}\lambda\left[\left[\mathbf{B}\right]\{\boldsymbol{\alpha}\} - \{\mathbf{R}\}\right]^T \left[\left[\mathbf{B}\right]\{\boldsymbol{\alpha}\} - \{\mathbf{R}\}\right] \tag{5.53}$$

where λ is a penalty number associated with the constraint term.

Finally, the generalized coordinates α_i (i = 0, 1, …, N) are determined by using the principle of minimum potential energy, which required that

$$\frac{\partial \bar{I}}{\partial \alpha_i} = 0 \,;\, i = 0, 1, \ldots, N \tag{5.54}$$

The substitution of Eq. (5.53) in Eq. (5.54) yields the following system of linear simultaneous equation:

$$\left[\mathbf{K}\right]\{\boldsymbol{\alpha}\} = \{\mathbf{F}\} \tag{5.55}$$

where

$$\begin{aligned}\left[\mathbf{K}\right] = {} & \pi D\left(\left[\mathbf{K}^{\mathbf{P1}}\right] + \left[\mathbf{K}^{\mathbf{P1}}\right]^T\right) + 2\pi D_1\left(\left[\mathbf{K}^{\mathbf{P2}}\right] + \left[\mathbf{K}^{\mathbf{P2}}\right]^T\right) \\ & + 2\pi\tau_{pl}^s\left(\left[\mathbf{K}^{\mathbf{P3}}\right] + \left[\mathbf{K}^{\mathbf{P3}}\right]^T\right) + \left(\left[\mathbf{K}^{\mathbf{h}}\right] + \left[\mathbf{K}^{\mathbf{h}}\right]^T\right) + \lambda\left[\mathbf{B}\right]^T\left[\mathbf{B}\right]\end{aligned} \tag{5.56}$$

$$\begin{aligned}\{\mathbf{F}\} = {} & \left\langle P\delta_{0i}\right\rangle^T + \left\langle \pi p_0 \cdot a^{2i+2} \middle/ (i+1)\right\rangle^T - 4\pi a_0 \ln a\left(D\left\langle \mathbf{Q}_1^{\mathbf{p}}\right\rangle + D_1\left\langle \mathbf{Q}_2^{\mathbf{p}}\right\rangle + 2\tau_{pl}^s\left\langle \mathbf{Q}_3^{\mathbf{p}}\right\rangle\right) \\ & - 2\pi a_0\left(2D\left\langle \mathbf{Q}_4^{\mathbf{p}}\right\rangle + D_1\left\langle \mathbf{Q}_5^{\mathbf{p}}\right\rangle + 4\tau_{pl}^s\left\langle \mathbf{Q}_6^{\mathbf{p}}\right\rangle\right) + \lambda\left[\mathbf{B}\right]^T\{\mathbf{R}\} - \left\langle \mathbf{Q}^{\mathbf{h}}\right\rangle\end{aligned} \tag{5.57}$$

in which δ_{ij} denotes a Kronecker delta. Note that the influence of penalty number λ on numerical solution is within the range $1 \le \lambda \le 10^5$ presented by Rajapakse (1988) to control the degree of accuracy.

The solution of a linear simultaneous equation system given by Eq. (5.55) yields the solution of the generalized coordinates α_i (i = 0, 1, …, N) for a given the nano-plate-half-space system as shown in Figure 5.2. Thereafter, the nano-plate deflection, bending moment, and shear force can be obtained by back substituting the generalized coordinates into Eqs. (5.10), (5.30) and (5.31), respectively.

5.5 Numerical Results and Discussion

A computer program based on a variational approach presented in this chapter has been developed to investigate the interaction problem between an elastic circular nano-plate and an isotropic elastic half-space as shown in Figure 5.2. The contact surface between the plate and half-space is assumed to be smooth, and the vertical displacement of the plate is represented by a power series of radial coordinate. The normal contact traction is expressed in terms of generalized coordinates through the solutions of the flexibility equations based on the Green's functions for an elastic half-space under uniform annular vertical loading and surface energy influence presented by Intarit (2012). The total potential energy of the nano-plate-half-space system consists of the strain energies of the plate, the surface, and the half-space, together with the potential due to the applied loading, given by Eq. (5.45). To obtain the solution of generalized coordinates, the principle of minimum potential energy is applied to the total potential energy of the nano-plate-half-space system with a constraint condition given by Eq. (5.54).

The accuracy of the present solution scheme is confirmed by comparing with existing solutions. Figure 5.4 (a) shows the comparison of normalized deflection profiles of a circular nano-plate with a simply-supported edge under a uniform loading, p_0, between the present solution and the solution proposed by Liu and Rajapakse (2013) for different number of generalized coordinates, N. The material parameters employed in the comparison are E_{pl} = 90 GPa and ν_{pl} = 0.23; and the surface material properties are τ_{pl}^{s} = 0.5689 N/m, λ_{pl}^{s} = 3. 4939 N/m, and μ_{pl}^{s} = -5.4251 N/m. In addition, the comparison of normalized deflection profiles of a circular nano-plate with a clamped edge under both a uniform load, p_0, and a point load, P, between the present and existing solutions as shown in Figure 5.4 (b). It is clearly seen that very good agreement between the two solutions is obtained with N = 5. Figure 5.5 (a) and 5.5 (b) respectively show radial profiles of normalized contact traction and bending moment of a circular plate on an isotropic elastic half-space without surface stress effects, between the present solution with N = 8 and Ne = 40 and the solution proposed by Brown (1969) for different values of relative plate stiffness, K_r, with ν_{pl} = 0.3. It is evident from Figure

5.5 that the present solution agrees very closely with Brown (1969) for all values of K_r. Note that the relative plate stiffness, K_r, is given as follows:

$$K_r = \left(1-\nu_h^2\right)\frac{E_{pl}}{E_h}\left(\frac{h_{pl}}{a}\right) \tag{5.58}$$

where E_h and ν_h are Young's modulus and Poisson's ratio of the half-space, respectively.

The influence of surface energy effects on interaction between an elastic circular plate under axisymmetric vertical loading and an elastic half-space is investigated in Figures 5.6 to 5.9. The following material parameters are employed in the numerical study: E_{pl} = 107 GPa and ν_{pl} = 0.33 for the plate; and λ_h = 58.17 GPa and μ_h = 26.13 GPa for the half-space. In addition, τ_{pl}^s = 0.6056 N/m, λ_{pl}^s = 4.4939 N/m, and μ_{pl}^s = 2.7779 N/m for the surface of the plate; and τ_h^s = 1 N/m, λ_h^s = 6.8511 N/m, and μ_h^s = -0.376 N/m for the top surface of the half-space. Note that the broken lines in all figures presented in this section denote the classical solutions where surface stress effects are ignored (i.e. $\tau^s = \lambda^s = \mu^s \approx 0$). Figure 5.6 and 5.7 respectively display radial profiles of normalized vertical displacements and bending moments of a circular nano-plate resting on an elastic half-space under a uniformly distributed vertical load of magnitude p_0 with $\bar{a}$ = a/Λ = 10 for different values of relative plate stiffness, i.e., K_r = 0.1, 1 and 10. Numerical results in Figure 5.6 and 5.7 indicate a significant influence of surface energy effects on both deflection and bending moment. It can be seen from Figure 5.6 that the normalized deflection from the present study is lower than its classical counterpart for all values of relative stiffness K_r whereas the normalized bending moment under the influence of surface stresses shown in Figure 5.7 is always larger than the corresponding classical solution. Therefore, the presence of surface stresses renders the plate stiffer.

Figure 5.8 shows variations of normalized central deflection of a circular nano-plate under the uniform vertical loading with normalized radius $\bar{a}$ for different values of relative stiffness K_r. It is evident from Figure 5.8 that under the influence of surface energy the normalized central deflection depends significantly on both normalized

radius and relative stiffness of the plate. Size-dependent behaviour due to the presence of surface stresses is thus clearly observed in the present solution whereas the classical elasticity solution is size-independent. Similarly, variations of normalized maximum bending moment of a circular nano-plate under the uniform vertical loading with normalized layer thickness, $\bar{h}_{pl}$ where $\bar{h}_{pl} = h_{pl}/\Lambda$, is presented for different values of relative stiffness K_r as shown in Figure 5.9. It is clearly demonstrated that the presence of surface stresses render the plate stiffer, and the material behaviour becomes size-dependent when the surface stresses are considered. In addition, the influence of surface energy effects is reduced with increasing value of $\bar{a}$ and $\bar{h}_{pl}$, and the present solution eventually converges to the classical solution.

5.6 Conclusion

A variational solution scheme is presented in this chapter to study the interaction problem between an elastic circular nano-plate and an isotropic elastic half-space under the influence of surface energy by adopting Gurtin-Murdoch surface elasticity theory. The contact surface between the nano-plate and the half-space is assumed to be smooth, and the deflection shape of the nano-plate is represented by a power series of the radial coordinate. The generalized coordinates in the series are obtained from the minimization of the total potential energy functional of an elastic circular nanoplate-half-space system, which consists of the strain energies of the plate, the surface, and the half-space, together with the potential due to the applied loading. The accuracy of the proposed solution scheme is confirmed by comparing with exiting solutions. Numerical results presented in this chapter indicate a significant influence of surface energy effects on the interaction problem, and the consideration of surface stresses renders the plate stiffer. In addition, the material behaviour becomes size-dependent when the surface stresses are taken into account. The proposed variational solution scheme can be used to study various interaction problems involving an elastic circular plate and an elastic medium with the presence of surface stresses for the applications related to nano-scale systems and soft elastic solids.

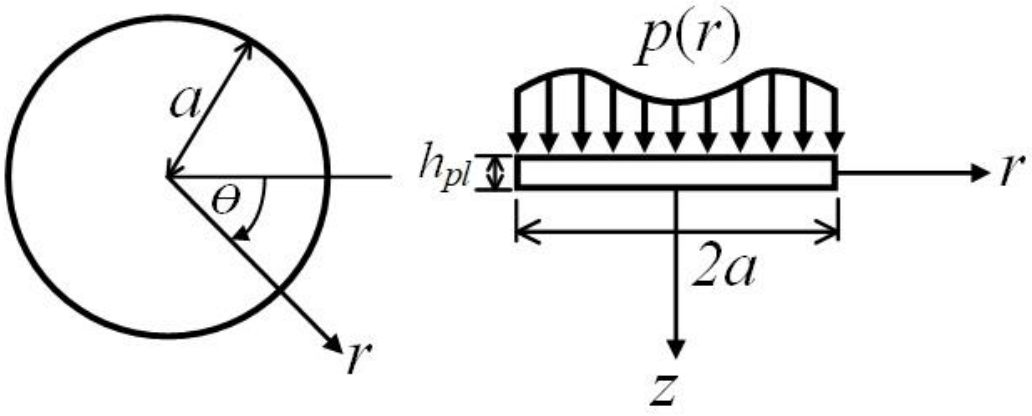

Figure 5.1 A circular nano-plate under axisymmetric vertical loading.

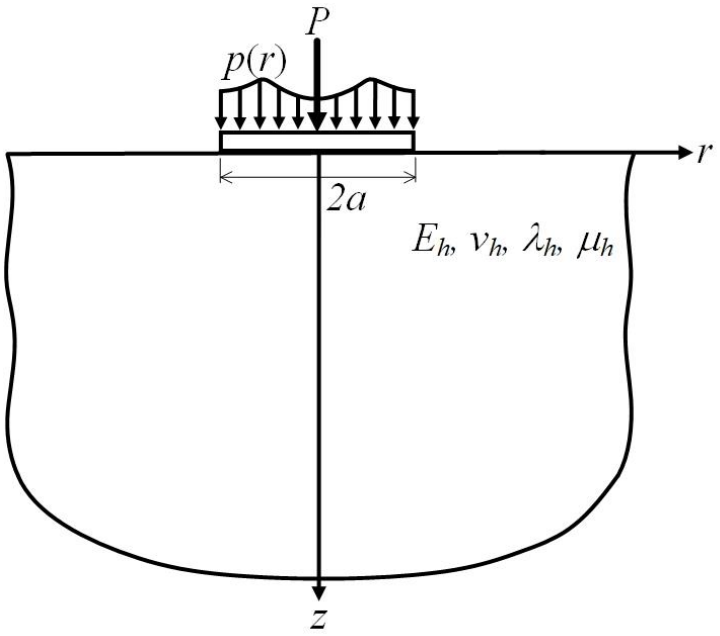

Figure 5.2 A circular nano-plate on an elastic half-space under axisymmetric vertical loading.

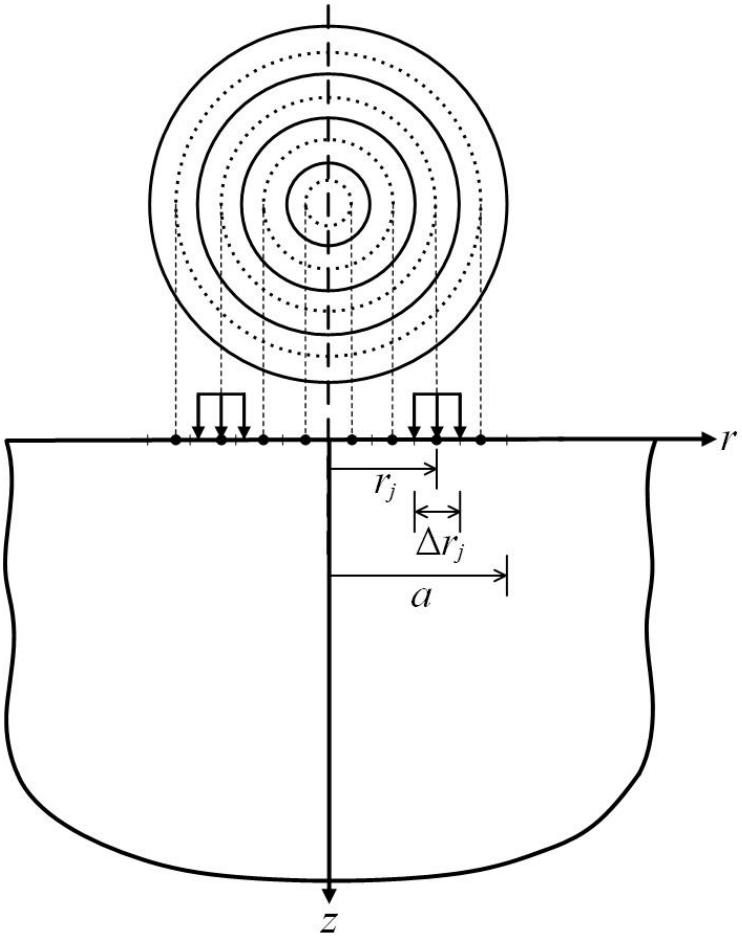

Figure 5.3 Unit vertical load applied over an annular region on an elastic half-space.

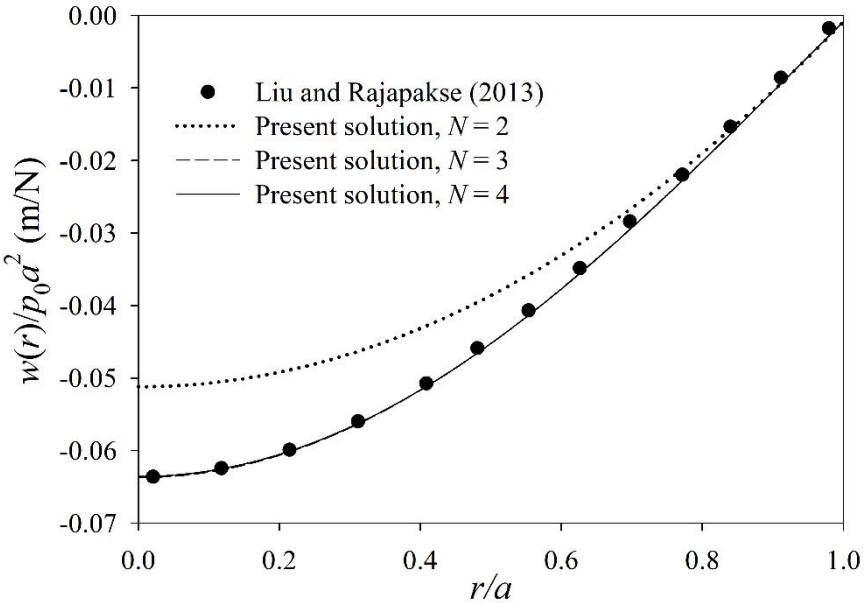

(a)

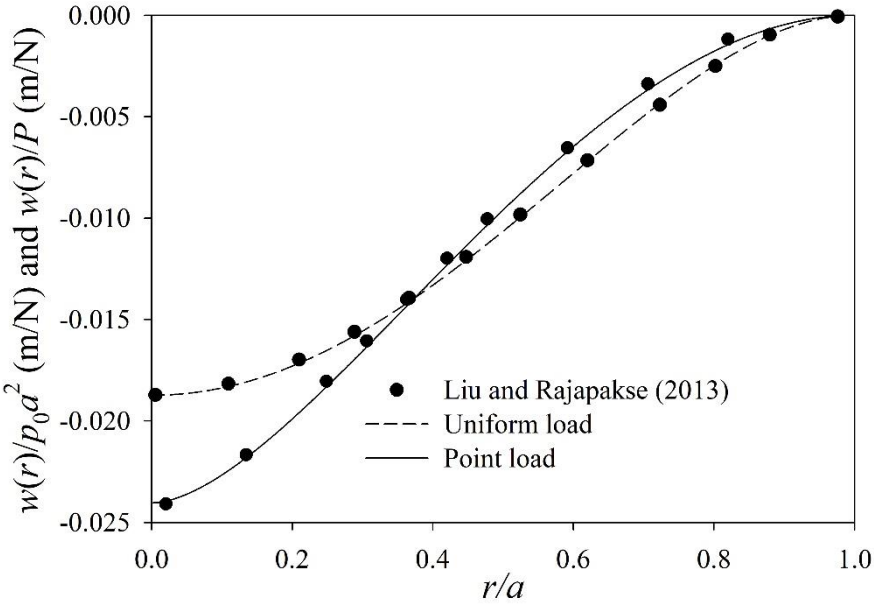

(b)

Figure 5.4 Comparisons for deflection of a circular nano-plate: (a) simply supported edge and (b) clamped edge.

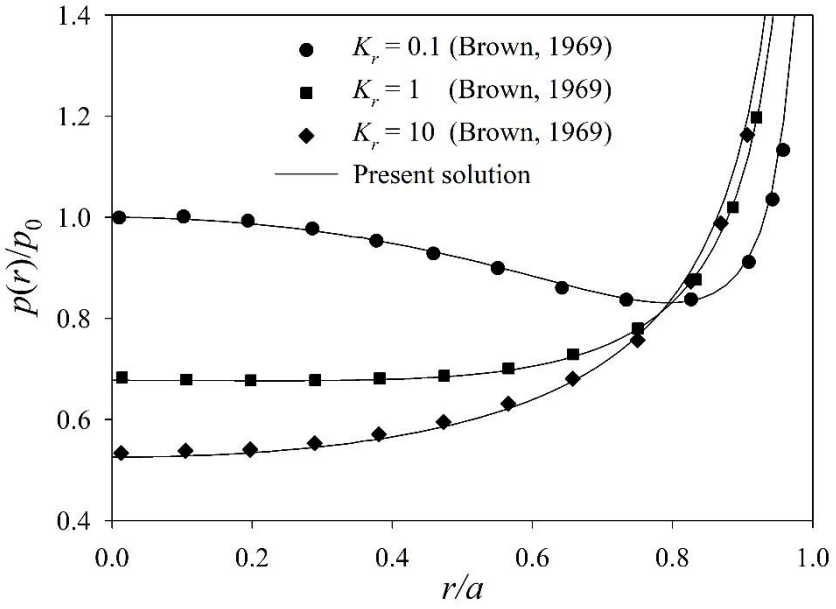

(a)

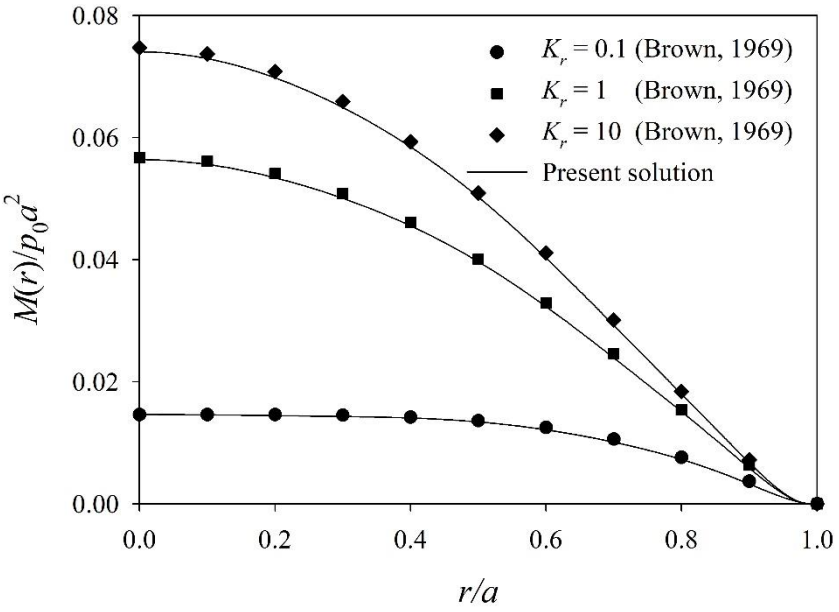

(b)

Figure 5.5 Comparisons for: (a) contact pressure and (b) bending moment of a circular plate on an elastic half-space without surface energy effects.

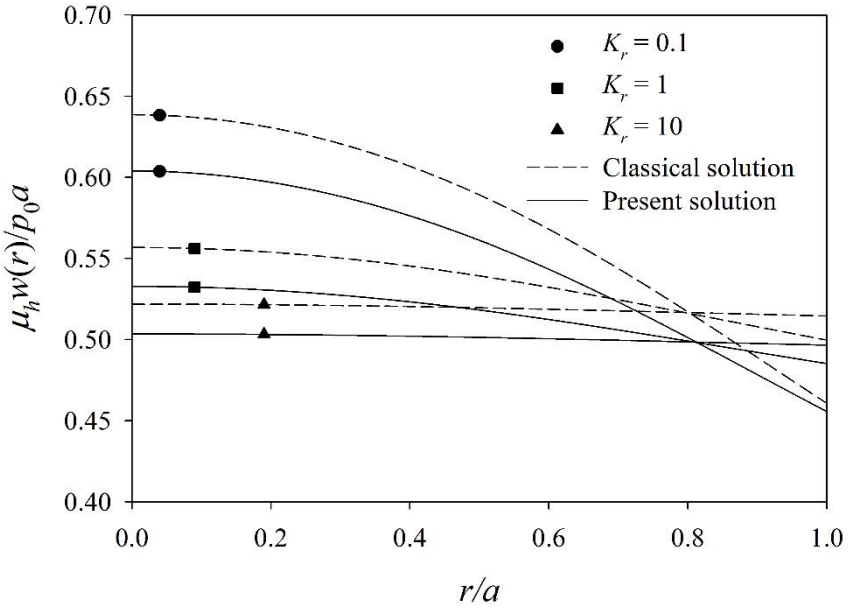

Figure 5.6 Radial profiles of normalized vertical deflection of a circular nano-plate resting on an elastic half-space under uniform vertical loading for different values of K_r with $\bar{a}$ =10.

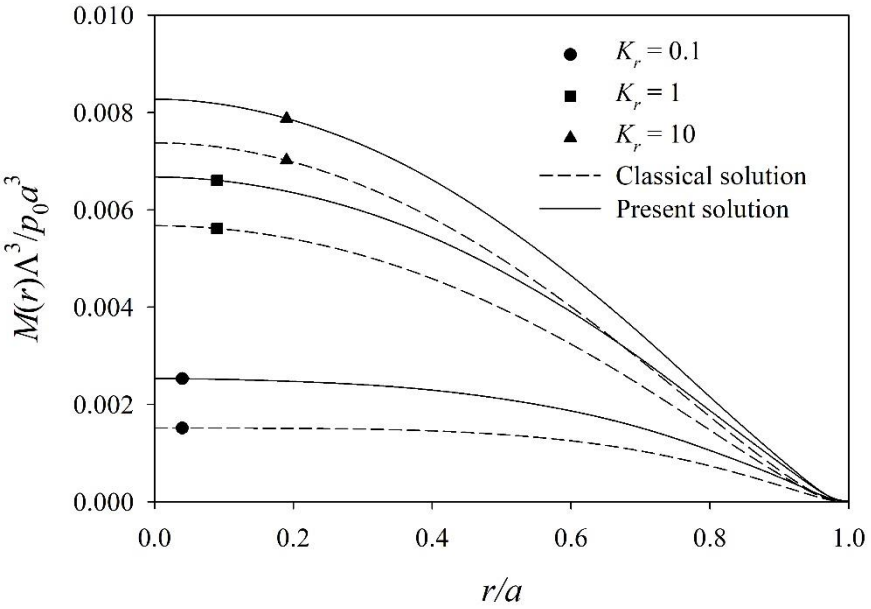

Figure 5.7 Radial profiles of normalized bending moment of a circular nano-plate resting on an elastic half-space under uniform vertical loading for different values of K_r with $\bar{a}$ =10.

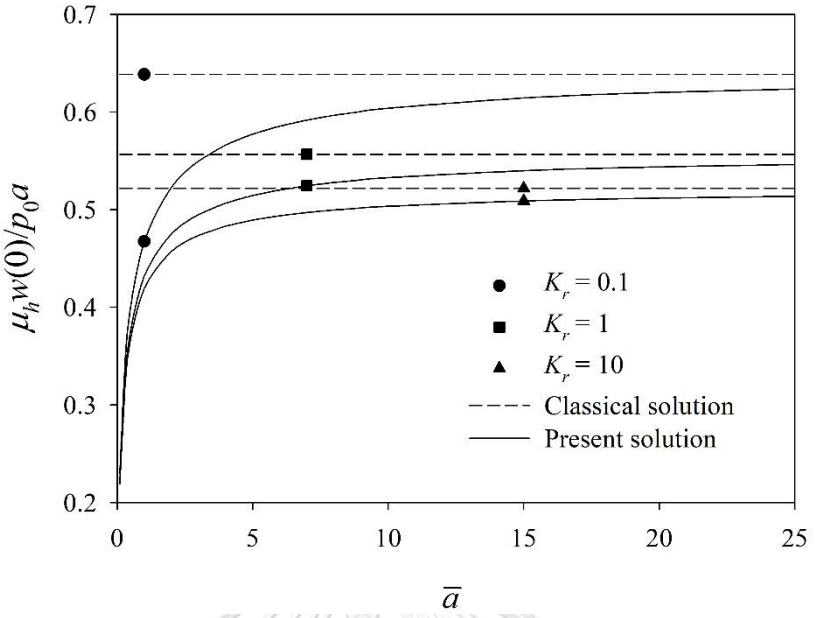

Figure 5.8 Variations of normalized central deflection with $\bar{a}$ of a circular nano-plate resting on an elastic half-space under uniform vertical loading for different values of K_r.

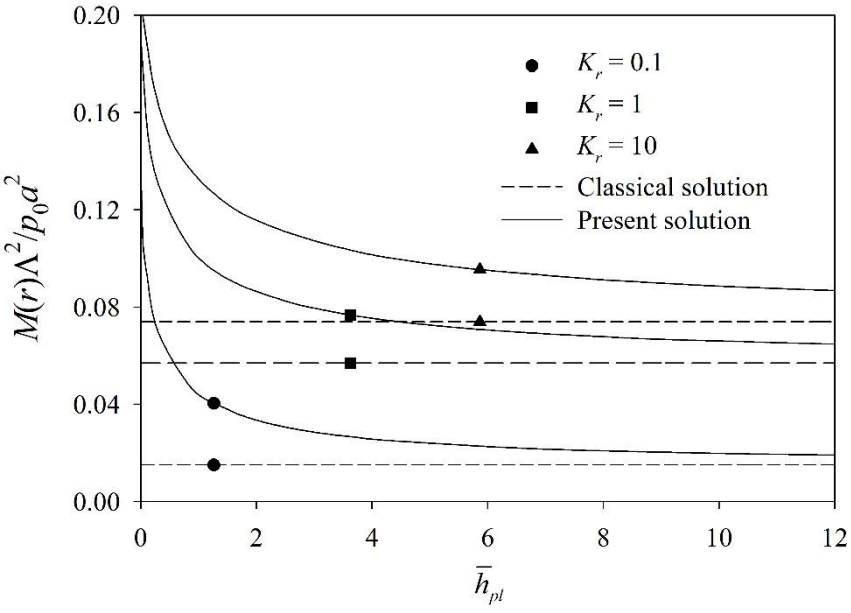

Figure 5.9 Variations of normalized maximum bending moment with $\bar{h}_{pl}$ of a circular nano-plate resting on an elastic half-space under uniform vertical loading for different values of K_r.

CHAPTER VI
CONCLUSIONS

This dissertation presents a theoretical study of contact problems of an elastic medium with consideration of surface energy effects by adopting a complete Gurtin-Murdoch theory of surface elasticity. A set of general solution for the displacement and stress within the bulk material is obtained by employing Love's strain potential and the Hankel integral transform and the final explicit solution of arbitrary functions is derived in Chapter III for the solution of a layered elastic half-space subjected to axisymmetric normal and tangential surface loadings. The obtained solutions are employed as the required influence functions for axisymmetric indentation on a layered elastic medium with frictionless and adhesive contacts presented in Chapter IV. In addition, they are also employed in the analysis of interaction between an elastic circular nanoplate and an elastic half-space based on a variation formulation outlined in Chapter V.

A computer program based on the above solutions has been developed to investigate the above contact problems with the influence of surface stress effects. The accuracy of the present solution scheme is confirmed by comparison with relevant existing solutions. An extensive parametric study is carried out in this dissertation and it indicates that the surface stresses have a significant influence on both displacement and stress fields of an elastic medium especially in the vicinity of the surface. Numerical results also confirms that unlike the classical elasticity solution the elastic medium becomes stiffer with size-dependent being observed under the presence of surface stresses. In addition, it is found that the influence of surface stresses on elastic fields becomes more significant when the radius of the indenter or the nanoplate is smaller. The present solution eventually converges to the classical solution when the radius becomes larger.

The solution presented in this dissertation can be used as a benchmark solution in the development of numerical techniques such as the finite element and boundary element methods for analysis of more complex contact problems under the influence of surface energy effects. In addition, the present solution scheme can be extended to investigate contact problems involving multi-layered systems with appreciate influence

functions such as nano-coatings and nanoscale surface layers in electronic devices; biomaterial applications; advanced industrial materials; and communication devices for nano-scale systems.

REFERENCES

Abdel Rahman, A. A. and Mahmoud, F. F. 2016. Analysis of nanocontact problems of layered viscoelastic solids with surface energy effects under different loading patterns. Acta Mechanica 227(2): 527-548.

Armstrong, R. W., Shin, H. and Ruff, A. W. 1995. Elastic/plastic effects during very low-load hardness testing of copper. Acta Metallurgica et Materialia 43(3): 1037-1043.

Attia, M. A. and Mahmoud, F. F. 2015. Analysis of nanoindentation of functionally graded layered bodies with surface elasticity. International Journal of Mechanical Sciences 94: 36-48.

Barber, J. and Ciavarella, M. 2000. Contact mechanics. International Journal of solids and structures 37(1): 29-43.

Borodich, F. M. 2014. Chapter Three - The Hertz-Type and Adhesive Contact Problems for Depth-Sensing Indentation. Advances in Applied Mechanics. S. P. A. Bordas, Elsevier. 47**:** 225-366.

Borodich, F. M. and Keer, L. M. 2004. Contact problems and depth-sensing nanoindentation for frictionless and frictional boundary conditions. International Journal of Solids and Structures 41(9): 2479-2499.

Borowicka, H. 1939. Druckverteilung unter elastischen Platten. Ingenieur Archive of Applied Mechanics 10(2): 113-125.

Boussinesq, J. 1885. Application des potentiels à l'étude de l'équilibre et du mouvement des solides élastiques: principalement au calcul des déformations et des pressions que produisent, dans ces solides, des efforts quelconques exercés sur une petite partie de leur surface ou de leur intérieur: mémoire suivi de notes étendues sur divers points de physique, mathematique et d'analyse, Gauthier-Villars.

Brown, P. T. 1969. Numerical Analyses of Uniformly Loaded Circular Rafts on Deep Elastic Foundations. Géotechnique 19(3): 399-404.

Burmister, D. M. 1945. The General Theory of Stresses and Displacements in Layered Systems. I. Journal of Applied Physics 16(2): 89-94.

Cammarata, R. C. 1994. Surface and interface stress effects in thin films. Progress in Surface Science 46(1): 1-38.

Cao, Y. P., Dao, M. and Lu, J. 2007. A precise correcting method for the study of the superhard material using nanoindentation tests. Journal of Materials Research 22(5): 1255-1264.

Chang, L. and Zhang, L. 2009. Mechanical behaviour characterisation of silicon and effect of loading rate on pop-in: A nanoindentation study under ultra-low loads. Materials Science and Engineering: A 506(1): 125-129.

Chen, W. and Engel, P. 1972. Impact and contact stress analysis in multilayer media. International Journal of Solids and Structures 8(11): 1257-1281.

Clements, D. L. 1971. The Indentation of an Anisotropic Half Space by a Rigid Punch. Journal of the Australian Mathematical Society 12(1): 75-82.

Craighead, H. G. 2000. Nanoelectromechanical Systems. Science 290(5496): 1532-1535.

Dhaliwal, R. S. 1970. Punch problem for an elastic layer overlying an elastic foundation. International Journal of Engineering Science 8(4): 273-288.

Dhaliwal, R. S. and Rau, I. S. 1970. The axisymmetric Boussinesq problem for a thick elastic layer under a punch of arbitrary profile. International Journal of Engineering Science 8(10): 843-856.

Dingreville, R., Qu, J. and Cherkaoui, M. 2005. Surface free energy and its effect on the elastic behavior of nano-sized particles, wires and films. Journal of the Mechanics and Physics of Solids 53(8): 1827-1854.

Doerner, M. F. and Nix, W. D. 1986. A method for interpreting the data from depth-sensing indentation instruments. Journal of Materials research 1(4): 601-609.

Duan, H. L., Wang, J., Huang, Z. P. and Karihaloo, B. L. 2005. Eshelby formalism for nano-inhomogeneities. Proceedings of the Royal Society A: Mathematical, Physical and Engineering Science 461(2062): 3335.

Eshelby, J. D., Read, W. T. and Shockley, W. 1953. Anisotropic elasticity with applications to dislocation theory. Acta Metallurgica 1(3): 251-259.

Fischer, F. D., Waitz, T., Vollath, D. and Simha, N. K. 2008. On the role of surface energy and surface stress in phase-transforming nanoparticles. Progress in Materials Science 53(3): 481-527.

Fox, L. 1948. Computation of Traffic Stresses in a Simple Road Structure, H.M. Stationery Office.

Galin, L. A. and Gladwell, G. M. L. 2008. Contact Problems: The legacy of L.A. Galin, Springer Netherlands.

Gao, X.-L. and Zhang, G. Y. 2016. A non-classical Kirchhoff plate model incorporating microstructure, surface energy and foundation effects. Continuum Mechanics and Thermodynamics 28(1): 195-213.

Gao, X.-L. and Zhou, S.-S. 2013. Strain gradient solutions of half-space and half-plane contact problems. Zeitschrift für Angewandte Mathematik und Physik (ZAMP): 1-24.

Gao, X., Hao, F., Fang, D. and Huang, Z. 2013. Boussinesq problem with the surface effect and its application to contact mechanics at the nanoscale. International Journal of Solids and Structures 50(16): 2620-2630.

Gerrard, G. M. 1969. Tables of stresses, strains and displacement in two-layer elastic systems under various traffic loads. Vic, Australian Road Research Board.

Gibbs, J. W., Bumstead, H. A. and Van Name, R. G. 1906. Scientific Papers of J. Willard Gibbs ...: Thermodynamics, Longmans, Green and Company.

Goodman, L. E. 1962. Contact Stress Analysis of Normally Loaded Rough Spheres. Journal of Applied Mechanics 29(3): 515-522.

Greenwood, J. and Barber, J. 2012. Indentation of an elastic layer by a rigid cylinder. International Journal of Solids and Structures 49(21): 2962-2977.

Gupta, P. K. and Walowit, J. 1974. Contact stresses between an elastic cylinder and a layered elastic solid. Journal of lubrication technology 96(2): 250-257.

Gurtin, M. E. and Murdoch, A. I. 1975. A continuum theory of elastic material surfaces. Archive for rational mechanics and analysis 57(4): 291-323.

Gurtin, M. E. and Murdoch, A. I. 1978. Surface stress in solids. International Journal of Solids and Structures 14(6): 431-440.

Gurtin, M. E., Weissmüller, J. and Larché, F. 1998. A general theory of curved deformable interfaces in solids at equilibrium. Philosophical Magazine A 78(5): 1093-1109.

Hainsworth, S. V. and Page, T. F. 1994. Nanoindentation studies of the chemomechanical effect in sapphire. Journal of Materials Science 29(21): 5529-5540.

Harding, J. and Sneddon, I. 1945. The elastic stresses produced by the indentation of the plane surface of a semi-infinite elastic solid by a rigid punch. Mathematical Proceedings of the Cambridge Philosophical Society, Cambridge University Press.

He, L. H. and Lim, C. W. 2006. Surface Green function for a soft elastic half-space: Influence of surface stress. International Journal of Solids and Structures 43(1): 132-143.

He, L. H., Lim, C. W. and Wu, B. S. 2004. A continuum model for size-dependent deformation of elastic films of nano-scale thickness. International Journal of Solids and Structures 41(3): 847-857.

Hertz, H. 1882. Ueber die Beruhrung fester elastischer Korper. J Reine Angew Math 92: 156-171.

Huajian, G., Cheng-Hsin, C. and Jin, L. 1992. Elastic contact versus indentation modeling of multi-layered materials. International Journal of Solids and Structures 29(20): 2471-2492.

Huang, D. W. 2008. Size-dependent response of ultra-thin films with surface effects. International Journal of Solids and Structures 45(2): 568-579.

Huang, G.-Y. and Yu, S.-W. 2006. Effect of Surface Elasticity on the Interaction Between Steps. Journal of Applied Mechanics 74(4): 821-823.

Intarit, P.-i., Senjuntichai, T. and Rungamornrat, J. 2018. Elastic layer under axisymmetric indentation and surface energy effects. Zeitschrift für angewandte Mathematik und Physik 69(2): 29.

Intarit, P. 2012. Solutions of Elastic Medium with Surface Stress Effects, Chulalongkorn University.

Intarit, P., Senjuntichai, T. and Rajapakse, R. 2010. Dislocations and internal loading in a semi-infinite elastic medium with surface stresses. Engineering Fracture Mechanics 77(18): 3592-3603.

Intarit, P., Senjuntichai, T., Rungamornrat, J. and Rajapakse, R. 2017. Penny-shaped crack in elastic medium with surface energy effects. Acta Mechanica 228(2): 617-630.

Intarit, P., Senjuntichai, T., Rungamornrat, J. and Rajapakse, R. K. N. D. 2011. Surface elasticity and residual stress effect on the elastic field of a nanoscale elastic layer. Interaction and multiscale mechanics 4(2): 85-105.

Jindal, P., Goyal, M. and Kumar, N. 2014. Mechanical characterization of multiwalled carbon nanotubes-polycarbonate composites. Materials & Design (1980-2015) 54: 864-868.

Jing, G. Y., Duan, H. L., Sun, X. M., Zhang, Z. S., Xu, J., Li, Y. D., Wang, J. X. and Yu, D. P. 2006. Surface effects on elastic properties of silver nanowires: Contact atomic-force microscopy. Physical Review B 73(23): 235409.

Katebi, A. and Selvadurai, A. P. S. 2015. A frictionless contact problem for a flexible circular plate and an incompressible non-homogeneous elastic halfspace. International Journal of Mechanical Sciences 90: 239-245.

Lei, D. X., Wang, L. Y. and Ou, Z. Y. 2012. Elastic Analysis for Nanocontact Problem with Surface Stress Effects under Shear Load. Journal of Nanomaterials 2012: 7.

Lim, C. W. and He, L. H. 2004. Size-dependent nonlinear response of thin elastic films with nano-scale thickness. International Journal of Mechanical Sciences 46(11): 1715-1726.

Liu, C. and Rajapakse, R. K. N. D. 2013. A Size-Dependent Continuum Model for Nanoscale Circular Plates. IEEE Transactions on Nanotechnology 12(1): 13-20.

Long, J. M. and Wang, G. F. 2013. Effects of surface tension on axisymmetric Hertzian contact problem. Mechanics of Materials 56: 65-70.

Long, J. M., Wang, G. F., Feng, X. Q. and Yu, S. W. 2012. Two-dimensional Hertzian contact problem with surface tension. International Journal of Solids and Structures 49(13): 1588-1594.

Lu, P., He, L. H., Lee, H. P. and Lu, C. 2006. Thin plate theory including surface effects. International Journal of Solids and Structures 43(16): 4631-4647.

Mao, S. X., Zhao, M. and Wang, Z. L. 2003. Nanoscale mechanical behavior of individual semiconducting nanobelts. Applied Physics Letters 83(5): 993-995.

Miller, R. E. and Shenoy, V. B. 2000. Size-dependent elastic properties of nanosized structural elements. Nanotechnology 11(3): 139.

Mindlin, R. and Tiersten, H. 1962. Effects of couple-stresses in linear elasticity. Archive for Rational Mechanics and analysis 11(1): 415-448.

Mindlin, R. D. 1964. Micro-structure in linear elasticity. Archive for Rational Mechanics and Analysis 16(1): 51-78.

Mossakovskii, V. I. 1954. The fundamental mixed problem of the theory of elasticity for a halfspace with a circular line separating the boundary conditions. Journal of Applied Mathematics and Mechanics 18: 187-196 (in Russian).

Mossakovskii, V. I. 1963. Compression of elastic bodies under conditions of adhesion (Axisymmetric case). Journal of Applied Mathematics and Mechanics 27(3): 630-643.

Oliver, W. C. and Pharr, G. M. 1992. An improved technique for determining hardness and elastic modulus using load and displacement sensing indentation experiments. Journal of materials research 7(6): 1564-1583.

Oliver, W. C. and Pharr, G. M. 2004. Measurement of hardness and elastic modulus by instrumented indentation: Advances in understanding and refinements to methodology. Journal of Materials Research 19(1): 3-20.

Ou, Z. Y. and Pang, S. D. 2013. Fundamental solutions to Hertzian contact problems at nanoscale. Acta Mechanica 224(1): 109-121.

Pak, R. Y. S., Simmons, B. M. and Ashlock, J. C. 2008. Tensionless contact of a flexible plate and annulus with a smooth half-space under axisymmetric loads by integral equations. International Journal of Mechanical Sciences 50(6): 1004-1011.

Perriot, A. and Barthel, E. 2004. Elastic contact to a coated half-space: Effective elastic modulus and real penetration. Journal of Materials Research 19(2): 600-608.

Piessens, R., de Doncker-Kapenga, E. and Ueberhuber, C. 1983. Quadpack. A subroutine package for automatic integration. Springer Series in Computational Mathematics, Berlin: Springer, 1983.

Pinyochotiwong, Y., Rungamornrat, J. and Senjuntichai, T. 2013. Rigid frictionless indentation on elastic half space with influence of surface stresses. International Journal of Engineering Science 71: 15-35.

Povstenko, Y. Z. 1993. Theoretical investigation of phenomena caused by heterogeneous surface tension in solids. Journal of the Mechanics and Physics of Solids 41(9): 1499-1514.

Rajapakse, R. K. N. D. 1988. The interaction between a circular elastic plate and a transversely isotropic elastic half-space. International Journal for Numerical and Analytical Methods in Geomechanics 12(4): 419-436.

Rau, I. S. and Dhaliwal, R. S. 1972. Further considerations on the axisymmetric Boussinesq problem. International Journal of Engineering Science 10(8): 659-663.

Rungamornrat, J., Tuttipongsawat, P. and Senjuntichai, T. 2016. Elastic layer under axisymmetric surface loads and influence of surface stresses. Applied Mathematical Modelling 40(2): 1532-1553.

Sapsathiarn, Y. and Rajapakse, R. 2013. Finite-element modeling of circular nanoplates. Journal of Nanomechanics and Micromechanics 3(3): 59-66.

Selvadurai, A. P. S. 1979. An energy estimate of the flexural behaviour of a circular foundation embedded in an isotropic elastic medium. International Journal for Numerical and Analytical Methods in Geomechanics 3(3): 285-292.

Selvadurai, A. P. S. 1979. The Interaction between a Uniformly Loaded Circular Plate and an Isotropic Elastic Halfspace: A Variational Approach. Journal of Structural Mechanics 7(3): 231-246.

Selvadurai, A. P. S. 2000. Partial differential equations in mechanics, Berlin New York : Springer.

Selvadurai, A. P. S. and Dumont, N. A. 2011. Mindlin's Problem for a Halfspace Indented by a Flexible Plate. Journal of Elasticity 105(1): 253-269.

Selvadurai, A. P. S. and Katebi, A. 2015. An adhesive contact problem for an incompressible non-homogeneous elastic halfspace. Acta Mechanica 226(2): 249-265.

Selvadurai, A. P. S., Labanieh, S. and Boulon, M. J. 2007. On the mechanics of contact between a flexible transducer diaphragm located at a rigid boundary and an elastic material. International Journal for Numerical and Analytical Methods in Geomechanics 31(7): 933-952.

Sharma, P., Ganti, S. and Bhate, N. 2003. Effect of surfaces on the size-dependent elastic state of nano-inhomogeneities. Applied Physics Letters 82(4): 535-537.

Sharma, P. and Wheeler, L. T. 2006. Size-Dependent Elastic State of Ellipsoidal Nano-Inclusions Incorporating Surface/Interface Tension. Journal of Applied Mechanics 74(3): 447-454.

Shenoy, V. B. 2002. Size-dependent rigidities of nanosized torsional elements. International Journal of Solids and Structures 39(15): 4039-4052.

Shenoy, V. B. 2005. Atomistic calculations of elastic properties of metallic fcc crystal surfaces. Physical Review B 71(9): 094104.

Shokrieh, M. M., Hosseinkhani, M. R., Naimi-Jamal, M. R. and Tourani, H. 2013. Nanoindentation and nanoscratch investigations on graphene-based nanocomposites. Polymer Testing 32(1): 45-51.

Sneddon, I. N. 1951. Fourier transforms. New York, McGraw-Hill.

Sneddon, I. N. 1965. The relation between load and penetration in the axisymmetric Boussinesq problem for a punch of arbitrary profile. International journal of engineering science 3(1): 47-57.

Spence, D. A. 1968. Self Similar Solutions to Adhesive Contact Problems with Incremental Loading. Proceedings of the Royal Society of London. Series A, Mathematical and Physical Sciences 305(1480): 55-80.

Stroh, A. N. 1958. Dislocations and Cracks in Anisotropic Elasticity. The Philosophical Magazine: A Journal of Theoretical Experimental and Applied Physics 3(30): 625-646.

Tian, L. and Rajapakse, R. K. N. D. 2006. Analytical Solution for Size-Dependent Elastic Field of a Nanoscale Circular Inhomogeneity. Journal of Applied Mechanics 74(3): 568-574.

Tian, L. and Rajapakse, R. K. N. D. 2007. Elastic field of an isotropic matrix with a nanoscale elliptical inhomogeneity. International Journal of Solids and Structures 44(24): 7988-8005.

Toupin, R. A. 1964. Theories of elasticity with couple-stress. Archive for Rational Mechanics and Analysis 17(2): 85-112.

Wang, Z.-Q., Zhao, Y.-P. and Huang, Z.-P. 2010. The effects of surface tension on the elastic properties of nano structures. International Journal of Engineering Science 48(2): 140-150.

Wong, E. W., Sheehan, P. E. and Lieber, C. M. 1997. Nanobeam mechanics: elasticity, strength, and toughness of nanorods and nanotubes. science 277(5334): 1971-1975.

Xu, H. and Pharr, G. M. 2006. An improved relation for the effective elastic compliance of a film/substrate system during indentation by a flat cylindrical punch. Scripta Materialia 55(4): 315-318.

Yakobson, B. I. 2003. Nanomechanics. Handbook of nanoscience, engineering, and technology. I. W. A. G. D. W. B. S. E. L. a. G. J. I. (ends.). Florida, CRC Press.

Yang, F. 1998. Indentation of an incompressible elastic film1This work was finished when the author was at the University of Rochester, Rochester, NY, USA.1. Mechanics of Materials 30(4): 275-286.

Yu, H. Y., Sanday, S. C. and Rath, B. B. 1990. The effect of substrate on the elastic properties of films determined by the indentation test — axisymmetric boussinesq problem. Journal of the Mechanics and Physics of Solids 38(6): 745-764.

Zaman, M. M., Kukreti, A. R. and Issa, A. 1988. Analysis of circular plate-elastic half-space interaction using an energy approach. Applied Mathematical Modelling 12(3): 285-292.

Zhao, X. 2009. Surface loading and rigid indentation of an elastic layer with surface energy effects, University of British Columbia.

Zhao, X. J. and Rajapakse, R. K. N. D. 2009. Analytical solutions for a surface-loaded isotropic elastic layer with surface energy effects. International Journal of Engineering Science 47(11): 1433-1444.

Zhou, S. and Gao, X.-L. 2013. Solutions of half-space and half-plane contact problems based on surface elasticity. Zeitschrift für angewandte Mathematik und Physik 64(1): 145-166.

APPENDIX

VITA

Mr. Supakorn Tirapat was born in Ubon Ratchathani, Thailand, on March 22, 1990. He obtained his Bachelor of Engineering degree in Civil Engineering from Khon Kean University on March 22, 2012. He then pursued Doctor of Philosophy degree in Civil Engineering at Chulalongkorn University in the same year under the supervision of Professor Dr. Teerapong Senjuntichai and Associate Professor Dr. Jaroon Rungamornrat with the support from Thailand Research Fund under the Royal Golden Jubilee Ph.D. (RGJ-Ph.D.) Scholarship. During his study, he was a visiting international research student at the Simon Fraser University, Burnaby, Canada, to conduct a research work with Professor Dr. Nimal Rajapakse from August, 2017 to December, 2017.